Fundamental Research On Direct Fabrication Of Low Dimensional Nanomaterials On Si Substrates

BY

JIAN-YIH CHENG
B.S., University of Illinois at Chicago, 2009
M.S., University of Illinois at Chicago, 2011

THESIS

Submitted in partial fulfillment of the requirements for the degree of Doctor of Philosophy in Mechanical Engineering in the Graduate College of the University of Illinois at Chicago, 2017

Chicago, Illinois

Defense Committee:

Dr. Carmen Lilley, Mechanical and Industrial Engineering, Chair and Advisor

Dr. Amin Salehi, Mechanical and Industrial Engineering

Dr. Constantine Megaridis, Mechanical and Industrial Engineering

Dr. Nathan Guisinger, Argonne National Laboratories

Dr. Maria Chan, Argonne National Laboratories

ACKNOWLEDGEMENTS

I would like to express my sincere gratitude towards my advisor, Dr. Carmen Lilley for supporting me throughout my graduate journey. Her guidance, technical knowledge, and patience were essential to help me move forward through my graduate career and it has been a pleasure working under her. I would also like to formally thank Dr. Nathan Guisinger, Dr. Maria Chan, Dr. Amin Salehi, and Dr. Constantine Megaridis for taking the time and effort to participate on my committee and to review the manuscript of this thesis. In particular, I am especially grateful for the time and efforts Brandon Fisher, Dr. Nathan Guisinger, and Dr. Maria Chan spent navigating me through the nuances of experimental and theoretical nanotechnology research.

I would also like to thank my lab mates Qilu He, Poh-Keong Ng, Tanim Humayun, and Genesis Ortega. It was an absolute pleasure befriending them over the course of my studies through office conversations, car pools, lunches, and random science excursions. Their insight and friendship helped break up the monotony of daily research. Finally, I would like to thank my parents and sister whose endless support gave me the drive to push through my studies.

CONTRIBUTION OF AUTHORS

Chapters 1-3 contain literature reviews on the materials and methods used during my dissertation research. Chapter 1 gives an introduction to my dissertation research as well as the overall research goal and its possible applications and importance to the field of nanoelectronics and nanomaterials. Chapter 2 represents a literature review and explanation of the theoretical methods used in my research. Chapter 3 represents a literature review and explanation of the experimental methods and techniques used in my research. Section 2 of Chapter 4 was published as a manuscript titled "Enabling direct silicene integration in electronics: First principles study of silicene on $NiSi_2$(111)" in *Applied Physics Letters* 2016 for which I was the primary author. I performed all the simulations and calculations, generated all the figures, and wrote the manuscript with supporting help and editing from my advisors Dr. Carmen Lilley and Dr. Maria Chan. Section 3 of Chapter 4 represents a set of unpublished theoretical calculations looking at the electronic contribution of Cu_3Si and $NiSi_2$ to a graphene due to their interface. I anticipate that the work in Chapter 4 Section 3 will be published as a part of a co-authored manuscript. All work in Chapter 5 represents a series of my own unpublished experiments looking at using chemical vapor deposition to directly grow graphene atop silicide layers fabricated on Si(111) substrates. I anticipate that the research contained in Chapter 5 will be continued after I leave and that the work will be used to publish a co-authored manuscript in the future. Chapter 6 was published as a manuscript titled "Atomically manufactured nickel-silicon quantum dots displaying robust resonant tunneling and negative differential resistance" in *Nature Quantum Materials* 2017 of which I was the primary author. I performed a large portion of the experiment alongside co-authors Brandon Fisher, Dr. Carmen Lilley, and Dr. Nathan Guisinger and generated Figure 1 and Figure 3 of the manuscript. I also provided the data and images for the

remaining manuscript figures compiled by my co-authors and contributed a large amount to the data analysis. Dr. Carmen Lilley, Dr. Nathan Guisinger, and I all contributed equally to manuscript writing and editing. Chapter 7 includes unpublished research regarding the atomic structure and electronic properties of single layer Sn on Si(111). I performed all experiments in Chapter 7 and generated all the figures. I anticipate that this research will be published in a co-authored manuscript soon after I leave the university. I anticipate the co-authors to include Dr. Carmen Lilley, Dr. Nathan Guisinger, Genesis Ortega, and myself. Chapter 8 is a summary of my research and how it ties back to my overall research goal and importance to this field of research. Chapter 8 also includes possible future experiments and research goals stemming from the research presented in my thesis.

TABLE OF CONTENTS

CHAPTER PAGE

Chapter 1 INTRODUCTION 1
1.1 Background and motivation 1
1.2 Research goals and objectives 4
Chapter 2 THEORETICAL METHODS 7
2.1 Overview of Density Functional Theory 7
2.2 DFT Parameters Used 9
Chapter 3 EXPERIMENTAL METHODS 12
3.1 Si Substrate Preparation 12
3.1.1 Si substrate Sample Preparation for STM Experiments 12
3.1.2 Si Sample Preparation for CVD Experiments 13
3.2 Fabrication Methods 13
3.2.1 Silicide Preparations 13
3.2.2 E-Beam Evaporation 14
3.2.3 Chemical Vapor Deposition 16
3.3 Characterization Methods 18
3.3.1 Scanning Tunneling Microscopy 18
3.3.2 Raman Spectroscopy 21
3.3.3 X-ray Diffraction 23
Chapter 4 DENSITY FUNCTIONAL THEORY SIMULATIONS OF SILICENE AND GRAPHENE ON SILICIDES 26
4.1 Introduction 26
4.2 Simulations of Silicene on $NiSi_2$ 26
4.3 Simulations of Graphene on $NiSi_2$ and Cu_3Si 40
4.4 Concluding Remarks 48
Chapter 5 GRAPHENE GROWTH ON SILICIDES 50
5.1 Introduction 50
5.2 CVD Graphene Growth on Cu_3Si Fabricated on Si Substrates 51

5.3 Attempted CVD of Graphene on $NiSi_2$ 59
5.4 Ethylene Decomposition on Sub-Monolayer Surface Reconstructions of Ni $\sqrt{19}$x$\sqrt{19}$ 60
5.5 Concluding Remarks 62
Chapter 6 CHARACTERIZATION OF SUB-MONOLAYER Ni DEPOSITION ON Si(111) .. 63
6.1 Introduction 63
6.2 Ni Surface Reconstruction atop Si(111) 64
6.3 Concluding Remarks 77
Chapter 7 SN SURFACE RECONSTRUCTION ATOP Si(111) 79
7.1 Introduction 79
7.2 Electronic Characterization of Sn Surface Reconstructions 79
7.3 Concluding Remarks 89
Chapter 8 CONCLUSIONS AND RECOMMENDATIONS FOR FUTURE WORK 91
8.1 Conclusions 91
8.2 Future Work 94
APPENDIX A 98
Background Correction 98
APPENDIX B 99
Journal Policies Regarding the Reprint of Published Work 99
REFERENCES 100
VITA 113

LIST OF TABLES

TABLE PAGE

Table 1 Summary of structural parameters of silicene and H:silicene, freestanding and atop $NiSi_2$ and H:$NiSi_2$. 30

Table 2 Band gaps of the Sn √3 and 2√3 reconstructions on Si(111) 88

LIST OF FIGURES

FIGURE PAGE

Figure 1 Simplified diagram of electron-beam evaporation onto a sample. The filament is heated by applying current $I_{Filament}$. Due to the HV potential applied between the filament and crucible the electron beam generated is directed towards the crucible heating the metal source, Ni until it evaporates creating a plume which deposits onto a sample aligned with the evaporator's opening. 15

Figure 2 Simplified schematic of CVD setup using the two gas mixtures for graphene growth. 18

Figure 3 Simplified schematic of STM operation. A bias voltage (V_{Bias}) is applied between the tungsten tip (W) and the sample. In this diagram, a positive V is applied to the sample as the tunneling occurs from the tip to the sample. As the tip approaches the sample, when the distance is close enough, electrons will tunnel across the energy barrier due to the vacuum between the two (vacuum barrier). 19

Figure 4 Simplified schematic of Raman spectroscopy system. An incident laser is used to excite a sample. The reflected beam is detected by a spectrometer and the Raman shift is measured. 22

Figure 5 XRD diagram showing the relation between the 2θ angle and sample surface..... 24

Figure 6 (a-c) Top and side view models of silicene on $NiSi_2$, silicene on H:$NiSi_2$ and H:silicene on $NiSi_2$ respectively (d) Side view of the bulk Si(111)-$NiSi_2$(111) interface. Red, green, blue, and silver atoms represent H, Si in the 2D layer, Si in $NiSi_2$ slab, and Ni, respectively. In (d), blue and silver atoms represent Si and Ni respectively. 30

Figure 7. Side view of the charge difference density plots. (a) Silicene on a $NiSi_2$ slab, (b) silicene on a H:$NiSi_2$ slab, (c) H:silicene on a $NiSi_2$ slab. Red, green, blue, and silver atoms represent H, Si in 2D layer, Si in $NiSi_2$, and Ni, respectively. Isosurface value was set at 0.015 e/$Å^3$ where yellow and light blue isosurfaces represent negative and positive charge density difference respectively. 33

Figure 8 Simulated STM images for (a) freestanding silicene, (b) silicene on a $NiSi_2$ slab, (c) silicene on a H:$NiSi_2$ slab, (d) freestanding H:silicene, (e) H:silicene on a $NiSi_2$ slab. All images were simulated using a bias voltage of -2.0 V relative to the Fermi energy. A simulated bias voltage of -2.0 V was chosen due to the high DOS close to -2 eV for the simulated systems. 34

Figure 9 Band structures of (a) freestanding silicene, (b) silicene on H:$NiSi_2$, (c) silicene on a $NiSi_2$ slab, (d) freestanding H:silicene, (e) H:silicene on $NiSi_2$. Solid grey lines in (b), (c), and (e) represent the band structure of the supercell including the 2D layer and substrate. Red markings in those subplots represents the band structure contribution of the silicene or H:silicene layer. (f) Zoomed view of freestanding silicene (red) and silicene on H:$NiSi_2$ (blue) band structure around the K point in the Brillouin zone. The Fermi energy was set at 0 eV for all plots. 36

Figure 10 Density of States (DOS) of (a) freestanding silicene, (b) freestanding H:silicene, (c) silicene on $NiSi_2$, (d) silicene on a H:$NiSi_2$, (e) H:silicene on $NiSi_2$. Red and blue lines represent the 2D layer total DOS and total DOS of the supercell system (2D layer and substrate) respectively (DOS of silicene only). 38

Figure 11 Charge difference density plot of graphene on $NiSi_2$. (a) Top view and (b) side view of graphene on $NiSi_2$(111). Brown, blue, and grey atoms represent C, Si, and Ni atoms respectively. 44

Figure 12 Charge difference density plot of graphene on Cu_3Si. (a) Top view and (b) side view of graphene on Cu_3Si(111). Brown, blue, and orange atoms represent C, Si, and Cu atoms respectively. 44

Figure 13 Band structure and DOS plot of the supercell (black) and decomposed graphene contribution (red) on $NiSi_2$. The Fermi energy of both plots was set to 0 eV. 46

Figure 14 Band structure and DOS plot of the supercell (black) and decomposed graphene contribution (red) on Cu_3Si. The Fermi energy of both plots was set to 0 eV..... 46

Figure 15 Representation of the standard CVD graphene growth on Cu foil process times, temperatures, and gas flows. Temperature and time axes are not to scale and are exaggerated for visual purposes.. 52

Figure 16 Raman maps of the optical microscope image shown in (a). (b-d) show Raman maps of intensities centered around wavenumbers 2750 cm^{-1} (2D), 1581 cm^{-1} (G) and 1351 cm^{-1} (D) respectively. Color bars show the relative signal intensity in arbitrary units. Derived Raman map (e) indicates the approximate number of graphene layers based upon the G:2D Raman peak intensity ratio..... 54

Figure 17 Normalized Raman (a) and XRD (b) spectra corrected for background slope. Spectra in (a) were taken over annealed Cu_3Si island without graphene (blue), over an annealed Cu_3Si island covered graphene (red), over a bare Si area between graphene covered Cu_3Si islands 56

Figure 18 Normalized Raman spectra over (a) 250 to 3200 cm^{-1} Raman shift and (b) a zoomed Raman shift plot around 1200 to 3200 cm^{-1} denoted by the dashed inset in (a). Spectra were corrected for background slope. Spectra were taken over an annealed Cu_3Si island without graphene (blue), over an annealed Cu_3Si island covered graphene (red), over a bare Si area between graphene covered Cu_3Si islands (green), and over a graphene covered Cu3Si island left in ambient conditions for three months (purple). 57

Figure 19. Raman spectroscopy (514 nm laser, 13.71 mW power, 20 sec dwell time, 5 acquisitions) of sample after CVD processing of Ni deposition on a Si(111) substrate. Peaks centered around 229, 294, and 320 cm^{-1} and a double peak centered around 376 cm^{-1} confirm the presence of $NiSi_2$ formed during the heating process. No graphene peaks were observed over the sample.. 60

Figure 20. Raman spectroscopy of sample after ethylene decomposition showing the presence of graphite (514 nm, 13.71 mw, 10 sec dwell). Red arrow markers are placed at the peaks centered over Raman shifts of 1363, 1594, 2714, and 2972 cm^{-1} which represent the D, G, 2D, and D+G peaks respectively. 62

Figure 21 Atomic-scale imaging of Ni-Si clusters. (a) Topographic STM image showing submonolayer Ni coverage, where regions of pristine Si(111)-7×7 surface reconstruction are visible (Sample Bias +2.0V, Setpoint Current 100 pA). Within the Ni restructured area there are predominately "ring-cluster" structures with the underlying reconstruction going 1x1. At the right corner boundary near clean Si(111), there are four unique dark ring structures. (b) Zoom in STM image of the ring-like structures reveals our two cluster formations (1×1 and √19). The ball and stick schematics show the atomic arrangement of the Si atoms relative to the central Ni atoms. The 1×1 clusters (circled in yellow) and the √19 clusters (circled in blue) consist of self-assembled atomic clusters of Si and Ni. 67

Figure 22 Resonance reveals quantum dot behavior in the atomic clusters. (a) Schematic diagram illustrating that the lowered dimensionality results in electron confinement within the clusters resulting in discrete quantized energy levels. As the size of the quantum dot decreases, the peak spacing should increase and is consistent with what we observe. (b) I-V measurements made over the Ni-Si atomic cluster quantum dots, where the turn-on energies are greater for the smaller 1×1 cluster. NDR is observed in both cluster structures at negative sample bias. (c) Averaged STS dI/dV spectra measured over the 1x1 clusters illustrated in the STM image inset. Clear resonance is observed with discrete energy levels in the cluster at positive and negative bias. Negative conductance is observed and correlated with NDR observed in I-V. (d) Averaged STS spectra of the larger √19 clusters show similar resonance but with a smaller gap between energy levels as illustrated. (e) Schematic band diagrams showing (I) Equilibrium where the Fermi level aligns and is within the conduction band due to degenerate doping of the Si, (II) Resonance where the chemical potential shifts the band of electrons in the conduction band into alignment with discrete energy level, and (III) NDR where the chemical potentials shift until the discrete level falls within the forbidden gap and cannot contribute to tunneling..... 69

Figure 23 Spatial tip dependence on resonance through quantum dots. (a) STM image showing a line of spectra measured over a √19 cluster. (b) As the position of the STM tip moves, it shifts out of resonance and the negative conductance is lost illustrating a dependence on tip-cluster spacing. (c) The resonant energy for the clusters is extremely reproducible. This histogram shows some statistical analysis of resonant peak energies and minima for the √19 cluster. Although we could benefit from more statistical data to reveal the exact distribution, the peak values lie within 100 meV and there is thermal broadening due to a room temperature tip. 74

Figure 24 Saturated surface coverage of √19 cluster self-assembly. (a) STM image showing domains of saturated Ni-Si √19 cluster formation, where they hexagonally arrange with domain boundaries visible within the image (Sample Bias -2 V, Setpoint Current 200 pA). (b) A zoomed in STM image shows a uniform array of √19 clusters with some defects and vacancies. (c) A spatial dI/dV map for the same area in (b) showing a rich electronic ordering within the tightly packed atomic quantum dot array (Sample Bias -2 V, Setpoint Current 200 pA). (d) STS dI/dV spectra measured at different points over the tightly packed √19 clusters. The peak at negative bias has broadened and we do not observe the presence of NDR. (e) I-V measurements also confirm the loss of NDR and only a slight shoulder is observed. As the clusters pack together tightly, we believe that the levels of the QD structures overlap and broaden the measured spectra. 76

Figure 25 Top and side view of the 13 atom model proposed by Toernvik et al. (a) before DFT relaxation and (b) after DFT relaxation. Blue Atoms represent Si, whilst grey, red, and green atoms represent the 2√3x2√3 Sn layer. Red and Green atoms in (a) represent the higher height dimers in the unrelaxed model. Their positions after relaxation are shown in (b). 81

Figure 26 (a) Room temperature (295K) STM topography (orange color scale) and conductance image (purple color scale) of a 2√3 island surrounded by √3 reconstruction. (I=100pA, V_b=-1V) (b) Topography and conductance image of the 4√3 reconstruction alongside the 2√3 and √3 reconstructions at LT. White dashed lines are guidelines for the eye highlighting the 4√3 areas. (I=250pA, V_b=1V)..... 82

Figure 27 Zoomed in view of the 2√3 and 4√3 phases at RT and LT. (a) Topography and conductance image of RT 2√3 reconstruction. (I=600pA, V_b=0.5V). (b) Topography and conductance image of 4√3 reconstruction alongside areas of 2√3. (I=1nA, V_b=1V) (c) Zoomed areas of the RT 2√3 phase from (a). (d) Zoomed areas of the LT 4√3 phase from (b). (e) FFT patterns of the topography and conductance image from (c) showing the spacings of the RT 2√3, which roughly correlate to the lattice parameters of the 2√3 unit cell. (f) FFT patterns of the topography and conductance images from (d) showing the spacings of the LT 4√3. 83

Figure 28 (a) Possible example of the dimer pair transition of Sn atoms from RT to LT. The rhombus represents a proposed unit cell of the 2√3consisting of 13 atoms at room temperature. Filled circles represent the atom in the pair with the higher height value. Dashed lines are guidelines to separate the paired 4√3dimers. (b) Line profiles over the 2√3 and 4√3 phases. 85

Figure 29 (a) Histogram of the average width of the 4√3 pattern and (b) the average spacing between each stripe or areas of 4√3. 86

Figure 30 STM topography image, dI/dV point spectroscopy plot, and logarithmic scale I-V point spectroscopy plot of (a) room temperature √3 phase (I=300 pA, V_b=-1.5 V) (b) low temperature √3 phase (I=500 pA, V_b=1 V) (c) room temperature 2√3 phase (I=600 pA, V_b=0.5 V) (d) low temperature 2√3 and 4√3 phases (I=100 pA, V_b=1 V). 87

Figure 31 Example of raw Raman spectra before (a) and after (b) background correction and normalization. 98

LIST OF ABBREVIATIONS

2D	Two Dimensional
DFT	Density Functional Theory
VASP	Vienna Ab Initio Simulation Package©
ATK	Atomistix Toolkit©
DOS	Density of States
LDOS	Local Density of States
FFT	Fast Fourier Transform
E-Beam	Electron Beam
CVD	Chemical Vapor Deposition
STM	Scanning Tunneling Microscope
STS	Scanning Tunneling Spectroscopy
UHV	Ultra High Vacuum
XRD	X-ray Diffraction
TMD	Transition Metal Dichalcogenide
DC	Direct Current
AC	Alternating Current
CDD	Charge Difference Density
NDR	Negative Differential Resistance
PVR	Peak Voltage Ratio

SUMMARY

This thesis aims to study the fabrication and characterization of low dimensional nanomaterials directly on Si. In this thesis, theoretical DFT simulations and experimental work were combined to study if a graphene layer would be stable atop a silicide and how the 2D layer properties may be affected. Further experimental studies looked at characterizing self-assembled Ni-Si quantum dots and Sn 2D layers on Si(111) substrates. Studying these low dimensional nanomaterials provides further insight into their fabrication and electrical properties for future applications.

The growth of 2D layers, such as graphene and silicene, have commonly been performed on metal foils or crystals such as Cu, Au, and Ag. However, these 2D layers must be transferred to a semiconducting substrate in order to fabricate a functioning device. This transfer process can be detrimental to the as-grown properties and may be a reason why the predicted properties of nanomaterials, such as graphene, have not been fully realized. Direct fabrication of a 2D layer on Si would eliminate this transfer process preserving the as-grown properties. Metal silicides may aid in this integration, by acting as a growth layer for 2D layers on top of Si substrates.

The silicene/$NiSi_2$(111) interface was studied using DFT simulations to see if a silicene layer would be stable and how the silicide layer would affect the 2D layer band structure and density of states (DOS). The second set of DFT simulations analyzed if graphene on $NiSi_2$(111) and Cu_3Si(111) would also be stable as well as the silicides' effects on the 2D layer band structure and DOS. These simulations showed that a silicene layer would be too strongly coupled to a $NiSi_2$ layer thus necessitating the need to hydrogenate the silicide or silicene to decouple the layers electronically. In contrast, graphene is not strongly coupled to $NiSi_2$ or Cu_3Si resulting in the preservation of its freestanding properties.

Subsequent experiments were performed to attempt the CVD growth of graphene with Cu and Ni silicides fabricated on Si(111) substrates. The silicides were formed after heating metal films on Si(111) during the CVD process before introducing a Ar/CH_4 mixture alongside Ar/H_2 to grow graphene. No CVD graphene growth atop $NiSi_2$ was observed. However, CVD grown graphene was successfully verified atop Cu_3Si structures on Si(111). X-ray diffraction(XRD) was used to verify the composition of the Cu silicide to be η`-Cu3Si formed during the heating steps of the CVD process. Raman spectroscopy was used to verify the presence of 1-3 layers of graphene atop the Cu_3Si structures of varying crystal quality along the surface of the sample.

The direct Si integration of even lower dimensional silicides nanostructures was explored through the self-assembly of Ni-Si ring structures. The $\sqrt{19}\times\sqrt{19}$ and 1x1 Ni surface reconstructions atop Si(111) are made of these Ni-Si ring structures. The ring like structures behaved similar to quantum dots as studied through scanning tunneling spectroscopy (STS). Additionally, these Ni-Si ring QDs displayed NDR with a negative bias on the degenerately P doped which is a characteristic advantageous to QD transistor design.

Unlike most metals, Sn does not form a silicide due to its low solubility with Si. 2D layers of Sn are of interest due to its theorized topological insulator properties. Sub-monolayer deposition of Sn on Si(111) results in the formation of $\sqrt{3}\times\sqrt{3}$ and $2\sqrt{3}\times2\sqrt{3}$ surface reconstruction phases. These 2D layers of Sn were studied using STM and STS at room temperature (295K) and low temperature (55K). At low temperature the $2\sqrt{3}$ phase underwent a transition to a newly observed $4\sqrt{3}\times2\sqrt{3}$ phase which displayed a unique checkerboard conductance image pattern indicating charge ordering, and thus may display a full charge density wave (CDW), observed in topological insulators, at even lower temperatures.

CHAPTER 1 INTRODUCTION

1.1 Background and motivation

Continuous demand for improvements to reduced electronic sizes, increased processor density, and faster performance of electronics have led researchers to study low dimensional nanomaterials for their electrical properties and sizes to achieve these criteria. Low dimensional nanomaterials are materials that have at least one critical dimension that is less than 1nm, for example one atomic layer in a two-dimensional (2D) film. Low dimensional nanomaterials include 2D atomic layers such as graphene, one-dimensional (1D) nanowire structures such as CNTs with diameters less than 1nm, and zero-dimensional (0D) structures such as Quantum Dots (QD) of a few atoms [1-4]. These specific examples of low dimensional structures are of particular interest in electronics applications due to their size and electrical properties as they display unique electrical characteristics suitable for electronics applications [1-4].

For example, graphene has been considered a revolutionary material due to its ballistic electron transport, low electrical resistivity, high chemical stability, and potential for tuning the band gap [2, 5-19]. Desirable electrical properties of graphene include its high electron mobility ranging from 200,000-1,000,000 $cm^2/V{\cdot}s$ [5-9] and large Fermi velocity of up to $2.6x10^6$ m/s in suspended form [6, 8-14]. Researchers have also attempted to tailor the band gap of graphene by surface modification, substrate engineering, or by applying an external electrical field [12, 15-19]. However, to utilize many of graphene's unique properties, there still remain technical challenges to its integration in electronics. Current challenges include creating wafer scale graphene films of high quality and integration onto semiconductor substrates, such as Si, for device fabrication [20]. Integration onto Si substrates, in particular, is of interest since graphene

is commonly grown on metal foils and then physically transferred to a semiconducting substrate after etching away the metal using chemicals [21-24]. This transfer process can induce defects affecting graphene's as-grown properties and may be a reason that it is difficult to achieve graphene's predicted properties [24]. Silicides may provide a method for integrating graphene directly on Si without this transfer process. Silicides themselves are alloys of metal and Si and can be fabricated directly on Si substrates [25]. They are also compatible with Si based processing techniques and can be patterned in devices [26].

In particular, Ni and Cu silicides have a long history in Si based electronics as contact materials and interconnects in CMOS technology [25, 27]. More recently Pt_3Si has been used to grow large scale, high quality graphene flakes [28]. The stability of graphene and its ability to protect a silicide layer from oxidation has also been shown when used as capping layers for Ni-Si, Fe-Si, and Co-Si silicides [29]. However, previous research of graphene growth atop silicides has only occurred using metal substrates in the graphene growth, followed by silicidation after the graphene has been grown [28, 29]. There remains a need to explore whether silicides fabricated directly atop Si substrates can also support direct graphene growth.

More recently, research on silicon based quantum computing [30], have further increased the demand for 0D and 1D nanomaterial research investigations for qubit design [31-33]. Thus, research on silicides that are 1D structures or quantum dots are of high interest due to their compatibility with current CMOS manufacturing [34-36]. Reducing the size of these self-assembled QD structures to the atomic limit (a few atoms in a QD) results in structures that resemble those of molecular electronics [37]. However, QD research of silicides is still in relative infancy and there remain many challenges to their fabrication as well as identifying their properties.

One particular challenge is controlled fabrication [38, 39]. Since the electronic properties of QDs are highly dependent on its size, controlling the size of the structure is important. At these small scales, self-assembly of QDs on Si substrates provides a method producing QD arrays [4, 39, 40]. However, there can be variances in the sizes of the self-assembled QD array. In addition, controlling the size and positioning of QDs within these arrays, and their resulting electrical properties still remains a challenge. Although some of these small structures at the atomic limit have been studied for QD applications, many other low dimensional structures metal silicides, such as Ni silicide atop Si have yet to be characterized for this application.

Finally, the low dimensional properties of 2D Sn on Si are also of high interest because of its predicted behavior as a topological insulator [41, 42]. As mentioned, Sn does not form a silicide with Si [43]. In the past, surface reconstruction with Sn on Si(111) and Ge(111) were studied by researchers [44, 45]. Reconstructed $\sqrt{3}\times\sqrt{3}$ Sn monolayers on semiconducting substrates Si(111) and Ge(111) have been researched and appear to exhibit superconducting characteristics at temperatures less than 4K [44, 45]. However, there are two possible reconstructions of Sn on Si(111), the $\sqrt{3}\times\sqrt{3}$ and $2\sqrt{3}\times2\sqrt{3}$. While the $\sqrt{3}\times\sqrt{3}$, has been explored in the past, the $2\sqrt{3}\times2\sqrt{3}$ reconstruction has not been extensively studied and it is unknown if it also displays charge ordering characteristics or other unique behaviors [46-48]. There remains a need to characterize other self-assembled silicide and metal structures at the bottom of the atomic limit, which may present unique electronic characteristics advantageous to those presented in current research.

As discussed, low dimensional nanomaterials have unique electrical characteristics due to their size and have potential to be used as structures in new technologies such as quantum

electronics. However, many challenges still remain on what their fundamental properties are at low dimensions and how to directly fabricate them on Si platforms.

1.2 Research goals and objectives

The research goal is to fabricate low dimensional nanomaterials with tunable electronic properties directly on Si. To achieve this goal, the research objectives are to:

i.) Use density functional theory (DFT) to study the properties of 2D films on silicides, where silicides would be epitaxial to a Si substrate.

ii.) Demonstrate the fabrication of graphene on Si(111) using a silicide layer.

iii.) Use self-assembly to directly fabricate metal silicide quantum structures on Si to study their electronic properties.

iv.) Fabricate low dimensional Sn on Si using self-assembly methods and study their electronic properties.

To address objective, (i.) DFT calculations were performed to study whether 2D layers such as graphene and silicene are stable atop silicides. The binding energy, band structure, and density of states (DOS) where calculated and these calculations were used to study how the silicide interface may affect the electrical properties of the 2D layer atop. Chapter 3 presents DFT simulations looking at the interface of silicene on $NiSi_2$, and the interface of graphene with $NiSi_2$ and Cu_3Si. In addition, bulk Si(111) and $NiSi_2$(111) have an extremely low lattice mismatch and are known to create a distinctly epitaxial interface [49-52]. Thus, a Si 2D film in the form of silicene on $NiSi_2$(111) will be explored to study whether $NiSi_2$(111) can be used in 2D Si growth. Chapter 4.2 explores the stability of a silicene layer on $NiSi_2$(111) and how the

interface affects the band structure, DOS, and Fermi velocity. Chapters 4.3 present similar interface effects of graphene on $NiSi_2$ and graphene on Cu_3Si.

Exploratory research on the direct fabrication of graphene on Si using silicides is presented in Chapter 5. This proof of concept experiment was performed to address objective (ii.) to use silicides to directly integrate graphene on Si substrates without the transfer method. $NiSi_2$ and Cu_3Si layers were formed on Si(111) through the surface phase reaction (SPR) method. Methane was used as the carbon source to react during the silicide layer during chemical vapor deposition (CVD) to form graphene. This method did not result in graphene growth on $NiSi_2$. However, using a Cu_3Si layer did result in 1-3 layers of graphene successfully grown and integrated on a Si(111) substrate. Silicide formation was verified using XRD, while graphene layer numbers, and crystal quality were verified using Raman spectroscopy.

Objective (iii.) was addressed by studying the quantum dot behavior self-assembled Ni-Si QDs on Si(111). The research was performed by reducing the dimensions of silicide systems to the atomic limit results and is presented in Chapter 6. Ni-Si QD structures on Si(111) form ring like structures similar to the $\sqrt{19}\times\sqrt{19}$ reconstruction [53]. Using scanning tunneling microscopy (STM), the electronic properties of these Ni-Si rings were studied and found to display negative differential resistance (NDR) and quantum resonance not previously observed. The presence of NDR in these silicide structures indicates that they behave like individual quantum dots isolated from the Si substrate.

Objective (iv) is addressed by performing STM analysis of low dimensional Sn layers on Si(111). Sn does not form a silicide due to the low solubility between Sn and Si [43, 54] and is of particular interest due to its superconducting properties at temperatures below 4K [55-57]. Low dimensional Sn layers on Si(111) form $\sqrt{3}\times\sqrt{3}$ [44, 58-60] and $2\sqrt{3}\times2\sqrt{3}$ [61-63] reconstructions

on Si(111). For simplicity, the √3×√3 and 2√3×√3 reconstructions will be referred to as √3 and 2√3 respectively. Previous literature has conflicting viewpoints on whether the √3 reconstruction displays CDW characteristics at low temperature indicating superconductivity within a 2D layer on semiconducting substrates [64-66]. However, no published works are available on the 2√3 reconstruction and whether it displays similar CDW behavior. Research presented in Chapter 7 focuses on the 2√3 reconstruction and a new 4√3×2√3 reconstruction of the 2√3 phase at low temperature (55K) on Si(111). This new phase is of interest due to conductance and topology images indicating charge ordering. The presence of charge ordering within the 4√3 phase may indicate the possibility of a CDW at lower temperatures providing further evidence towards Sn monolayers of Si acting as a topological insulator.

CHAPTER 2 THEORETICAL METHODS

2.1 Overview of Density Functional Theory

Density Functional Theory (DFT) is a theoretical method to calculate the ground state energy of a many-body atomic system using a series of approximations [67]. The first approximation used is the Born-Oppenheimer approximation which takes advantage of the large difference in mass between electrons and nuclei to allow the electrons to be treated separately from the ions [67]. This reduces the Hamiltonian operator to terms operating on electronic wave functions, namely kinetic, plus electron-nuclei and electron-electron interactions. The Schrödinger equation can then be rewritten as equation 2.1. The Hamiltonian is represented by H, the energy by E, and the many-body electron wave function as Ψ.

$$H\boldsymbol{\Psi} = E\boldsymbol{\Psi} \quad \text{ref.[68]} \tag{2.1}$$

Explicitly, the many-electron Schrödinger equation is written as

$$H\Psi = \sum_{i=1}^{N}\left(-\frac{\hbar^2}{2m}\nabla_i^2\Psi - Ze^2\sum_R \frac{1}{|\boldsymbol{r_i}-\boldsymbol{R}|}\Psi\right) + \frac{1}{2}\sum_{i\neq j}\frac{e^2}{|\boldsymbol{r_i}-\boldsymbol{r_j}|}\Psi = E\Psi \quad \text{ref.[68]} \tag{2.2}$$

where ħ, m, and Z represent Planck's constant, the mass of an electron, and atomic number of the element respectively. The symbols r and R represent the electron and atom nuclei positions respectively.

Since solving (2.2) with explicit many-body wavefunctions is monumentally challenging, the Density Functional Theory [69] approach is a mean-field solution that treats single-particle wavefunctions ψ instead. The resulting Kohn-Sham equation [70] is shown in equations 2.3 and

2.4. The first potential (V(r)) defines the potential energy due to electron interaction with atomic nuclei of the system. The second potential is a function the energy of a system due to Coulomb interactions with the mean field due to all other electrons, often referred to at the Hartree potential [67]. The third potential is referred to as the exchange-correlation potential which represents all remaining electron-electron interactions [69]. Instead of E in (2.2) which is the total energy of the system, ε is used to represent the single-particle energy eigenvalues. The V symbols in equations 2.3 and 2.4 represent potentials as a function of electron position r.

$$\left[-\frac{\hbar^2}{2m}\nabla^2 + V(\boldsymbol{r}) + V_H(\boldsymbol{r}) + V_{XC}(\boldsymbol{r})\right]\psi_i(\boldsymbol{r}) = \varepsilon_i\psi_i(\boldsymbol{r}) \text{ ref.[67, 69, 70]} \quad (2.3)$$

$$\left[-\frac{\hbar^2}{2m}\nabla^2 + V_{Known} + V_{Hartree} + V_{Exchange-Correlation}\right]\psi_i(\boldsymbol{r}) = \varepsilon_i\psi_i(\boldsymbol{r}) \text{ ref.[67, 69, 70]} \quad (2.4)$$

In most practical DFT calculations, the Kohn-Sham equation is solved self-consistently to yield the total energy, electronic charge density, and single-particle energy eigenvalues of a many-body system, and other electronic and magnetic properties [69, 70]. Kohn-Sham theorems defined how these potentials and electron density of a system may be used to define the energy and electrical properties of a multibody system [69, 70]. DFT simulations define an estimated electron density of a multibody system and then calculate the electron density using the Kohn-Sham equations. If the defined and calculated electron density match, then it is assumed that this is the ground state electron density and the total energy and other electrical and magnetic properties of a multibody system may be calculated [70].

Defining the exchange-correlation (XC) functional of the Kohn-Sham equation is the most complex and time-consuming portion of DFT. The two most basic XC approximations are the Local Density Approximation (LDA) which depends only on electronic charge density at a point [71],straightforward electron density around an atom [71] and the Generalized Gradient

Approximation (GGA), which depends also on the local charge density gradient [72, 73]. Many alternative XC approximations and branches of existing XC approximations have and are currently being developed to better replicate the natural behavior of electrons.

To simplify DFT calculations, core electrons are grouped together with atomic nuclei and treated with a pseudopotential [74]. Many kinds of pseudopotentials exist and alter the valence potentials used in DFT calculations in order to better replicate conditions in nature. The Projector Augmented Wave (PAW) approach is a generalization of the pseudopotential approach. PAW is commonly used and considered relatively accurate [75-77].

From a surface science standpoint, DFT calculations themselves may be used to find the relaxed atomic positions in bulk crystals and surface slabs as well as the relaxed structure of nanomaterials [70, 78-80]. DFT has proven to be a valuable tool in predicting the electronic properties, such as band structure and Density of States (DOS), of low dimensional 2D layers, such as graphene, TMDs, and silicene [1, 17, 79, 81-84]. However, due to the use of approximations in DFT calculations, the results are just that, approximations. The accuracy of DFT results are highly dependent on the parameters used and has been used to accurately measure the binding energy between molecules and surfaces. Constant development and refinement of XC functions and pseudopotentials continues to improve the realistic accuracy of DFT results.

2.2 DFT Parameters Used

To address objective (i.), DFT simulations were performed with the Vienna Ab Initio Simulation Package (VASP) © [76, 85, 86]. The resulting output files from VASP© calculations were analyzed using Quantum Wise Atomistic Tool Kit (ATK)© [87, 88], Vesta© [89] and

p4vasp© [90]. These programs were used to visualize, analyze, and output data. DFT calculations were used to determine the surface energy, binding energy of a 2D layer, stability and structure of a 2D layer on a silicide, the band structure, the DOS, and predicted STM images of a 2D layer on a silicide. Specifically, DFT calculations were used to determine the relaxed structure of silicene and graphene on a $NiSi_2$(111) surface slab, and graphene on Cu_3Si(111) as well as electronic properties of the 2D layer. The specific DFT calculations performed are detailed in Chapter 3.

In this work, the Perdew-Burke-Ernzerhof (PBE) GGA exchange-correlation functional was used [73]. The GGA-PBE exchange correlation was used instead of LDA since it is the commonly used exchange correlation in metal silicides [91-93] and graphene [94, 95] DFT calculations. The Projected Augmented Wave (PAW) pseudopotentials were used, with PAW atom pseudo potentials supplied by VASP© [77]. Relaxations were performed with Gaussian smearing, DOS calculations were performed using tetrahedron method smearing with Blöchl corrections, and band structure calculations were performed with Methfessel-Paxton smearing. Smearing was used to smooth out the electron occupancy within partially filled energy bands of the system to improve the convergence of the calculations. The Gaussian, Methfessel-Paxton, and tetrahedron smearing methods use a Guassian, step, and linear functions respectively to fill those partially filled bands [67, 68].

Atomic models were created using ATK© [87, 88] using the most common methods for simulating surface slabs with DFT [67]. Interface models between a 2D layer and silicide surface slab were created by straining the 2D layer over silicide surface so that the lattices aligned while maintaining a 2D layer lattice strain of less than 2%. Ionic relaxations were performed on bulk crystals, silicide surface slabs, and 2D layer and silicide surface slab interfaces with k-point

meshes varying from 4×4×1 to 14×14×1 depending on the cell size. Through these ionic relaxations, the total energy of the systems were determined and used to calculate surface energy, and binding energy of a relaxed 2D layer structure on a silicide. Relaxations of the surface slabs and interfaces were performed while keeping the cell size fixed. Surface slabs themselves were created with at least 8-9 layers with a minimum of 15 Å vacuum above the surface to prevent periodic interaction along the z-direction boundaries. The three topmost layers of the surface slabs were allowed to relax, while the remaining layers were kept fixed.

Band structure and DOS calculations were performed with a higher k-point mesh density than ionic relaxations to maintain accuracy. Band structure calculations were performed over the common G-M-K-G path for hexagonal unit cells within the Brillouin zone and decomposed valence and atom contributions to the band structure and DOS was determined from the resulting simulations. The decomposed data was plotted to find the contributions of the 2D layer or silicide layer to the overall band structure and DOS. Simulated STM images were calculated to predict the charge density of 2D layer on silicide at different applied bias voltages to simulate the local density of states (LDOS) plots seen in topographical STM images. Simulated STM images were calculated using bias voltages from -2 to +2 consistent with normal experimental STM images taken within that range.

CHAPTER 3 EXPERIMENTAL METHODS

3.1 Si Substrate Preparation

3.1.1 Si substrate Sample Preparation for STM Experiments

The sample preparation for Si substrates prepared for experiments performed in the Omicron™ Variable Temperature (VT) Ultra-high vacuum (UHV) STM is outlined first. Si samples were prepared from Si(111) wafers degenerately doped with As or B, with resistivities of 0.001-0.0006 Ω·cm were purchased from Virginia Semiconductor. These wafers were diced into sample strips of 10x3 mm. Samples doped by As or B were used for Chemical Vapor Deposition (CVD) or Electron beam (e-beam) deposition respectively.

Before a Si sample was placed into a UHV chamber it was cleaned with solvents. Strips were cleaned using acetone then isopropyl alcohol before being mounted to a Direct Current (DC) Mo holder. The DC holder was inserted into a load lock chamber of an Omicron™ VT STM and pumped down to a pressure on the order of 10^{-9} mbar before transfer into the UHV preparation chamber. Before a sample is transferred to the analysis chamber it must be degassed and flashed. The Si sample is degassed at 600°C for a minimum of 12 hours to remove any hydrocarbons from the surface. After the degas process, the sample is flash heated to 1200°C for 30 seconds, then cooled slightly to 900°C for 90 seconds before letting it cool to room temperature. The flash heating process is performed 3-5 times to remove the native oxide from the Si surface allowing the sample to cool back to room temperature and the chamber pressure to return to within UHV range. Flash heating of the sample is repeated until there is little to no change in preparation chamber pressure signifying that no native oxide is being degassed from the sample.

3.1.2 Si Sample Preparation for CVD Experiments

For Si samples used in CVD, the same diced 10×3 mm Si strips were first cleaned using acetone and IPA. The native oxide was then removed by using buffered oxide etch (BOE) (1:10, HF:(NH_4F+H_2O)) bath for 60-90 seconds until the Si surface became hydrophilic. After the BOE dip the samples were rinsed using de-ionized (DI) water for 120 seconds before being dried using N_2. Once samples had been through a BOE process they were placed within the Lesker™ e-beam evaporator for metal deposition.

3.2 Fabrication Methods

3.2.1 Silicide Preparations

Electron beam evaporation has been used in both the SPR and reactive deposition epitaxy (RDE) methods to fabricate silicides. Both methods require metal deposition on a Si substrate and heating the sample to induce silicidation. The difference between the two silicide fabrication methods is that RDE method requires that the metal deposition occur while simultaneously annealing the substrate [96-98]. The SPR method uses a sequential approach to deposition of the metal followed by annealing the sample after deposition is completed [99]. In this research, e-beam evaporation was used to deposit Ni and Sn metal layers on the Si substrates in the Omicron™ VT UHV STM system. Within the UHV chamber, the e-beam deposition was coupled with direct current substrate heating to induce RDE silicide growth and self-assembly of the low dimensional Ni structures. The CVD process utilized an SPR method of silicide growth since the e-beam deposition was used to deposit thicker metal layers on Si, which is later heated during the CVD heating process.

3.2.2 E-Beam Evaporation

Electron beam (e-beam) evaporation was used for thin film deposition of metals on Si in UHV systems [100]. E-beam evaporation is a physical vapor deposition method requiring the use of a high vacuum or UHV environment in order to operate [100]. To produce an electron beam, a potential is applied between the electron filament and the crucible holding the deposition source. The bombardment of electrons on the metal source (in this case Ni, Cu, or Sn) causes the source to heat and evaporate. The evaporation of the source material creates a plume of metal evaporant which travels to the sample whose surface is aligned with the opening of the evaporator and the center of the plume. A simplified schematic of electron beam evaporation may be seen in Figure 1. The deposition rate using e-beam evaporation is directly related to the electron beam emission current. The stronger the electron beam emission current, the faster the electron bombardment of the source and faster heating/evaporation of the source. To control the emission current and subsequently the deposition rate two parameters may be directly controlled; the voltage potential between the electron filament and the crucible holding the source, and the electron filament current.

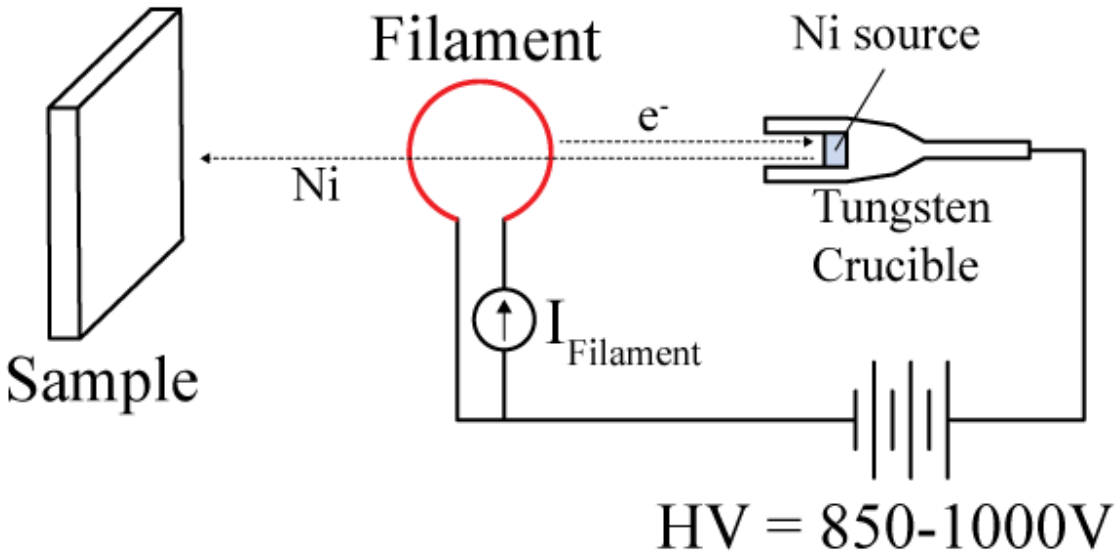

Figure 1 Simplified diagram of electron-beam evaporation onto a sample. The filament is heated by applying current $I_{Filament}$. Due to the HV potential applied between the filament and crucible the electron beam generated is directed towards the crucible heating the metal source, Ni until it evaporates creating a plume which deposits onto a sample aligned with the evaporator's opening.

An Omicron™ EMF3 single source e-beam evaporator was used for metal evaporation on Si in the Omicron™ UHV system. The Omicron™ e-beam evaporator was operated in the preparation chamber of the UHV with chamber pressures kept around 10^{-9} mbar. For these experiments, the Ni and Sn sources were held in a W crucible. Since Sn reacts with W, a C liner was used to prevent Sn and W interaction. The purity of Ni and Sn sources was around 99.9999% and 99.99% respectively. The following parameters were used for the e-beam evaporator: HV = 850-1000 V, $I_{filament}$ = 1.70-2.00 A, $I_{emission}$(flux) = 50-100 nA, $P_{UHV} < 10^{-9}$ mbar. By controlling the HV and $I_{filament}$, the flux of the evaporant can be controlled. The HV is kept static, while the $I_{filament}$ is altered to control the flux value. However, the HV may need to be changed depending on the source material to achieve flux values within the nA even μA range. The flux cannot be used to calculate the deposition thickness. A crystal quartz monitor is not installed within the UHV system where this specific e-beam evaporator was used. Deposition

thickness is estimated based upon the resulting surface reconstructions observed during topological STM images.

A Lesker™ e-beam evaporation system was used for the metal deposition of samples used in the CVD. The Lesker™ e-beam system is a HV system that has a chamber pressure of around 10^{-7} mbar. Ni or Cu layers of 100-300 nm were deposited on Si substrates diced into 10x3 mm samples sizes. Evaporation sources of Ni and Cu pellets of 99.999% purity purchased from Kurt J. Lesker Company™ were used. This system is operated by a single tool owner and uses a crystal quartz monitor to measure the deposition thickness.

3.2.3 Chemical Vapor Deposition

Chemical Vapor Deposition (CVD) has been used for 2D layer growth such as graphene [101] and Transition Metal Dichalcogenides (TMDs) [102] on various substrates. The basic principle of CVD involves the flow of gases into a heated chamber, which react over the substrate surface and/or decompose to form a desired material deposit [103]. Parameters that affect the depositions include the chamber pressure, gases used, substrates used, and temperatures. A conventional method of growing graphene on Cu and Ni foils using Atmospheric Pressure CVD (AP CVD) involves the flow of H_2 and CH_4 at a temperature of around 1000˚C for 30-60 minutes [101, 104]. The CH_4 catalyzes on the metal surfaces leaving behind a carbon deposit, which forms into graphene due to the high temperature. The excess hydrogen from the reaction of the CH_4 on the surface is carried out by the flow of H_2.

The CVD furnace used in this research was an MTI™ AP CVD furnace. A two-inch inner diameter alumina tube was used and an alumina boat was used to hold the sample during the entire process. In this research the tube was heated to temperatures between 800-1100˚C.

During the temperature ramp up, growth, and cool down stages, an Ar/H_2 gas mixture was constantly flowed through the tube at 200 sccm. When the tube reached the desired maximum temperature for the growth stage, an Ar/CH_4 mixture was flowed through the tube at 100 sccm for 60-90 minutes. Flow rate of the CH_4 mixture controls the carbon concentration the sample is exposed to during the growth phase at maximum temperature during the CVD process. Increasing the flow rate and/or time of exposure of the CH_4 mixture can increase the amount of C deposited on the sample. However, increasing the H_2 mixture flow rate can be detrimental since it can act as an etchant to the surface after deposition when the flow of the CH_4 mixture is stopped. After the growth stage, the methane mixture was stopped and only the Ar/H_2 mixture was present during the cool down. Unlike some other graphene growth processes, pure H_2 and CH_4 gases were not used due to the location of the CVD furnace and safety regulations on the maximum mixture percentages that could be used. The mixtures of H_2 and CH_4 with Ar gas did not require the use of higher flowrates since the Ar/H_2 and Ar/CH_4 mixture percentages used maintained a similar H_2:CH_4 ratio during the graphene growth process. A simple schematic of the CVD process using the Ar/H_2 and Ar/CH_4 mixtures may be seen in Figure 2.

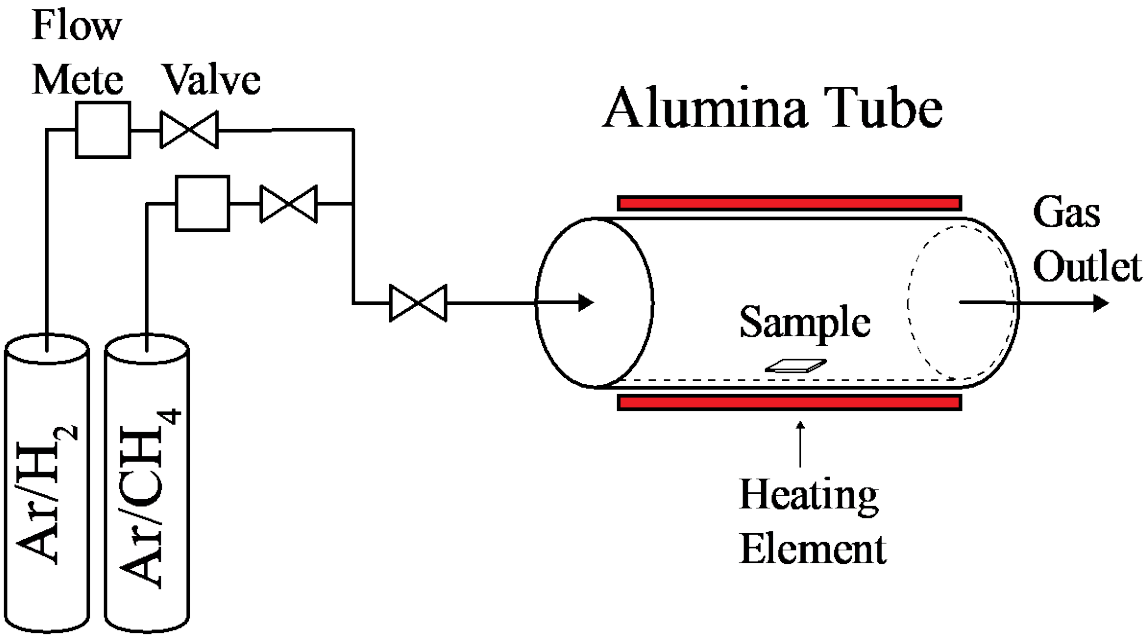

Figure 2 Simplified schematic of CVD setup using the two gas mixtures for graphene growth.

3.3 Characterization Methods

3.3.1 Scanning Tunneling Microscopy

Scanning Tunneling Microscopy (STM) is a technique of using electron tunneling between a tip and sample to create atomic images of the surface and was first demonstrated in 1982 by Binning et al. [105]. Using STM, the approximate atomic structure (not composition) and LDOS of surface structures may be studied. STM relies on the principle of electron tunneling. In an STM system, there is a sharp tip and sample separated by a vacuum. When a bias voltage potential is applied between the tip and the sample, the vacuum between the two acts as an energy barrier [106]. The direction of the applied voltage potential can be changed depending on the desired direction of electron tunneling. If the tip is approached towards the surface of the sample, eventually there will be close enough distance for electrons to tunnel from

the tip to the sample. This flow of electrons is referred to as the tunneling current. The two primary parameters of STM operation are the bias voltage (V_{Bias}) and tunneling current (I). The range of scans for V_{Bias} is typically within the range of -2 to +2 V [105]. If V_{Bias} is positive, electrons are tunneling from the tip to empty states sample. A simplified schematic of STM operation with V_{Bias} as positive is shown in Figure 3. If V_{Bias} is negative, electrons are tunneling from the filled states of the sample to the tip. Scanning at varying V_{Bias} produces a series of images at different energy levels. These images give a better understanding of the surface structure and surface states at specific energy levels.

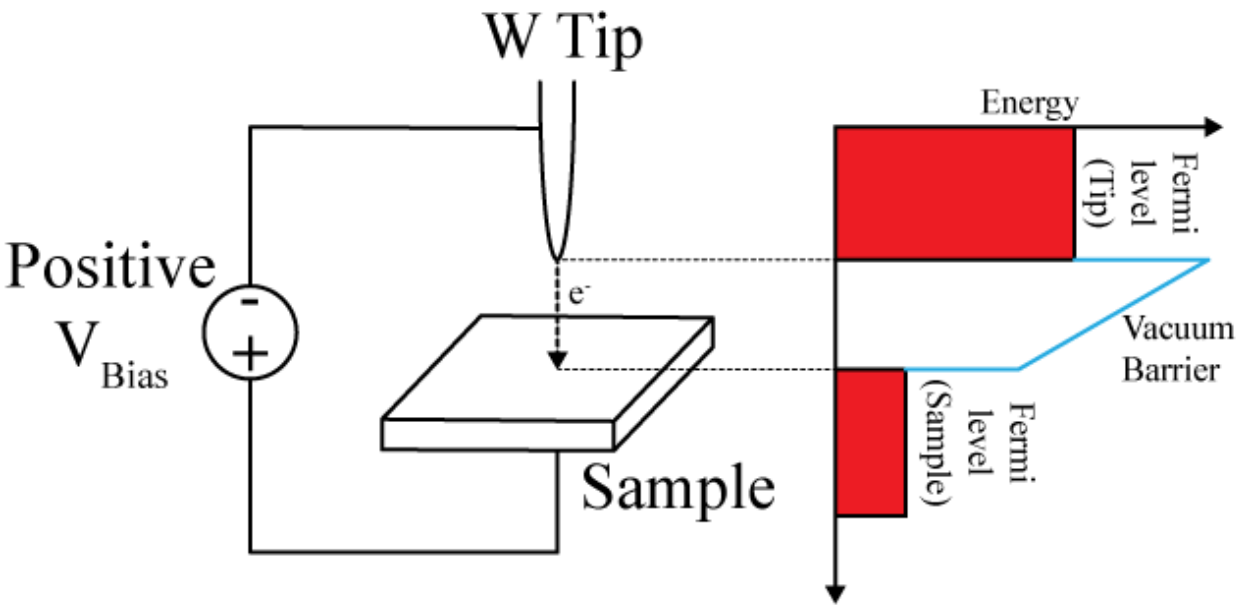

Figure 3 Simplified schematic of STM operation. A bias voltage (V_{Bias}) is applied between the tungsten tip (W) and the sample. In this diagram, a positive V is applied to the sample as the tunneling occurs from the tip to the sample. As the tip approaches the sample, when the distance is close enough, electrons will tunnel across the energy barrier due to the vacuum between the two (vacuum barrier).

The STM used was an Omicron™ variable temperature AFM/STM system. A Stanford Instruments™ SR830 lock-in amplifier was used to amplify the current signals for measurements. The UHV analysis chamber housing the STM was held at 10^{-11} mbar. Tips were

electrochemically etched W and were flashed at high temperature once inserted into the UHV chamber housing the STM. Low temperature was achieved using a liquid He cryostat and the minimum temperature was 55K. Bias voltages between -2 to +2 V were applied during scanning. I-V and dI/dV spectra were usually taken over a similar bias range of -2 to +2 V. The current set point was varied between samples and scans in order to accentuate topological and conductance image data. However, in certain cases the tip current could affect the scan quality and cause a tip crash necessitating scans to be taken at low current setpoints (~100 mA). A starting setpoint during tip approach to the sample surface was 100 mA. Stable scans over atomic structures were normally performed using 200-500 mA current setpoints. Higher current setpoints decrease the tip to sample distance but also increase the measured signal intensity. If the sample surface was stable, the current setpoint was increased to 1 nA. However, it is noted that at this high current setpoint, there was a tendency for the tip to crash after only completing a partial scan. The rastered measurement of tip height while maintaining a constant current setpoint was used to generate a topographical image of the atomic surface. Simultaneous measurements of I-V and dI/dV over the same area were used to generate a complementary conductance image using the lock-in technique. The lock-in technique uses a lock-in amplifier to measure the signal strength under noise taking the AC portion of the tunneling current whose in-phase signal modulation that matches the V_{Bias} modulation directly equals dI/dV. The dI/dV data is known as the differential conductance and is proportional to the local density of states (LDOS). Plotting dI/dV data versus voltage may be used determine if low dimensional materials behave like quantum dots by plotting dI/dV vs. the V_{Bias}. In this experiment, STM was used to look at the atomic structure and LDOS associated with metal surface reconstructions over Si substrates. Specifically, STM was used to study at the structure and NDR behavior of Ni-Si ring structures self-assembled on

Si(111). It was also used to study the surface reconstruction, possible charge ordering, and band gap change of Sn monolayers at low temperature on Si(111). Gwyddion©, open source software was used to process STM topographic and conductance images. The details on how Gwiddion© is used to plane level, remove scarring, adjust for drift, and other image processing corrections may be found in the software manual and its cited literature [107, 108].

3.3.2 Raman Spectroscopy

The Raman effect was first observed in 1928 by C.V. Raman [109]. When light illuminates a sample surface some of the light is absorbed, scattered, and reflected. The photon excitation of a sample can result in phonon scattering due to the elasticity or inelasticity of bonds between atoms [109]. This phonon scattering can be detected by slight variations to the intensity and wavelength of scattered and reflected light known as the Raman shift. The signal of these wavelength shifts results in high intensity peaks at certain Raman shifts that can be associated with specific elements and compositions. A schematic of how Raman spectra are taken is shown Figure 4. In this research, objective (ii) was to perform a proof of concept graphene growth on silicides fabricated directly on Si substrates. Raman spectroscopy was used to verify and characterize graphene films and the underlying substrate. To verify the presence of graphene, Raman shift peaks in the 1200-3000 cm^{-1} range were analyzed, where peaks at around 1350, 1580, 2750 cm^{-1} correspond to the D, G, and 2D carbon peaks [110, 111]. The presence of graphene is confirmed when there are G and 2D Raman peaks. A further analysis and explanation of the significance of these peaks is presented in Chapter 4. Raman spectroscopy was used in this experiment to verify the presence of graphene on silicides and to determine graphene crystal quality. It was also used to determine the composition of Ni-silicide on Ni

samples. It was not used to determine the composition Cu-silicide as it is considered Raman invisible, similar to pure Cu [101].

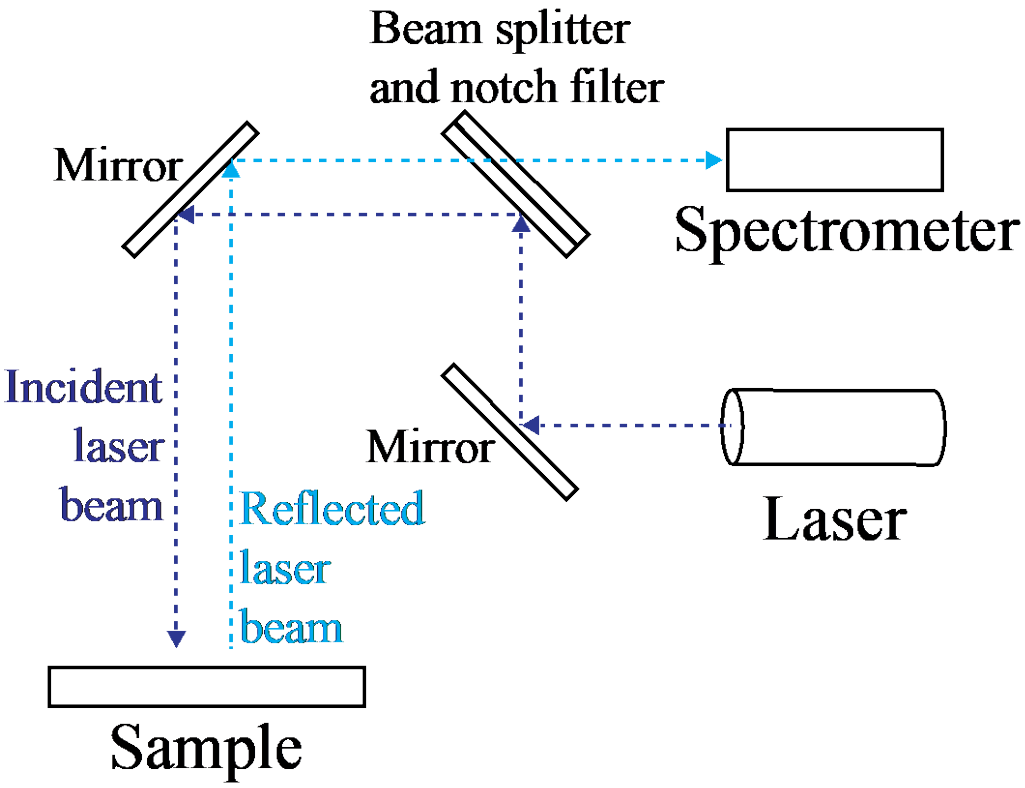

Figure 4 Simplified schematic of Raman spectroscopy system. An incident laser is used to excite a sample. The reflected beam is detected by a spectrometer and the Raman shift is measured.

Raman spectroscopy was performed using a Renishaw® inVia Raman microscope. This microscope has available laser wavelengths that span from the infrared (IR) to ultraviolet (UV). In this particular system, a 442 nm laser was the primary excitation source. A 442 nm laser was usually preferred over the 514 nm and 632 nm laser wavelengths due to the smaller background noise at higher Raman shifts. Graphene and other C based spectra peaks occur within higher Raman shifts thus the need for lower background noise over that range. An 1800 L/mm diffraction grating was used and at 100x magnification the laser spot size was approximately 0.2

μm. The maximum power of the 442 nm and 514 nm lasers are 23.7 mW and 13.71 mW respectively. To minimize sample heating the laser power was usually reduced to 5-10% of the maximum power. Dwell times were set at ten seconds to optimize the signal, yet not oversaturate the detector over strong peaks. Increasing the laser power too high can oversaturate the detector and the signal making the spectra taken too noisy. Similarly increasing the dwell time of the detector over certain Raman shifts can also oversaturate the detector, but can be used to increase the signal accentuating weak Raman peaks. Raman data was plotted using the Matlab® software. There is usually some curvature associated with the measured spectra due to optical effects. This background curvature was subtracted from the raw spectra to flatten the data for plotting. The method used for background correction is described in the Appendix.

3.3.3 X-ray Diffraction

It was discovered in 1912 that crystalline surfaces may act as diffraction grating for X-rays [112, 113]. When an X-ray interacts with a crystalline surface at specific incident angles the sample can act like a diffraction grating to reflect X-rays and cause constructive interference with the incident X-ray intensity. A schematic of XRD operation is shown in Figure 5. The θ angle is the angle between the sample surface plane and the X-ray. A detector is stationed opposite of the X-ray source at the exact same θ angle to detect constructive diffracted X-rays. The diffracted X-rays are measured by the 2θ angle shown in the schematic. By sampling X-rays across a range of 2θ angles a spectra of diffracted X-ray intensities can be measured. The peaks and intensities of this spectra represent crystallographic planes present in the sample. In XRD systems, X-rays are generated and these incident X-rays are measured for intensity across a 2θ angle range. The parameters controlled are X-ray power, sample rotation (optional), and 2θ angle range. By controlling the X-ray power one can control the depth penetration of the X-rays at the

sample surface. Sample rotation can be used to increase the number of crystallographic planes the incident X-rays encounter, which may increase the signal strength in low dimensional structures of powders or islands. The 2θ range can be varied to target the specific peaks of known crystallographic planes for a sample. In this experiment, XRD was used to detect the crystallographic planes associated with $NiSi_2$ and Cu_3Si silicides fabricated on Si(111). X-ray power was not altered for these experiments since the sample substrate is Si(111) which has known XRD peaks which do not interfere with the expected silicide peaks.

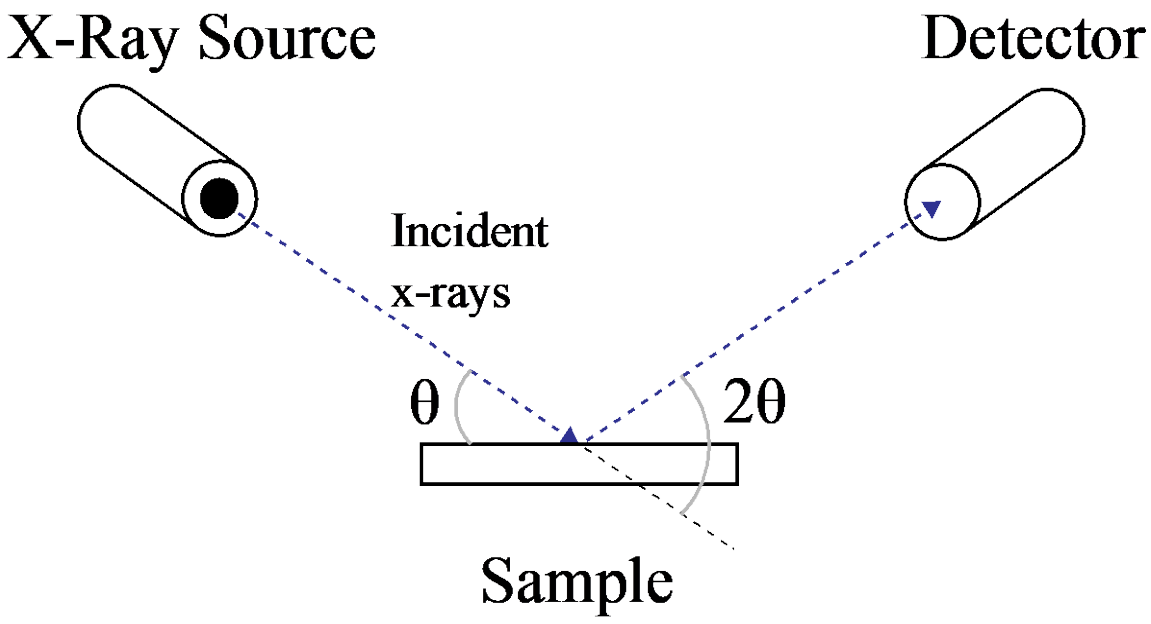

Figure 5 XRD diagram showing the relation between the 2θ angle and sample surface.

The XRD measurements in this experiment were performed using the Bruker™ D2 Phaser XRD machine. The X-ray power was set using a voltage of 30 kV and current of 100 mA. A 1 mm X-ray collimation slit was used and the 2θ range was varied to between 20-90˚ to capture the silicide XRD peaks. In the case of this experiment, the resulting silicide layer formed islands of varying sizes over the sample surface. The size and distribution of the islands made it

hard to achieve a static sample XRD spectrum so the silicides were treated as a “powder” by spinning the sample at 60 rpm. By spinning the sample the X-rays have a chance to reflect off a larger number of silicide islands’ crystallographic surfaces giving a stronger signal. Similar to Raman signals, there is normally some curvature to the measured XRD spectra due to optical effects. Background curvature was subtracted from the XRD spectra in the same manner as Raman spectra described in the Appendix.

CHAPTER 4 DENSITY FUNCTIONAL THEORY SIMULATIONS OF SILICENE AND GRAPHENE ON SILICIDES

4.1 Introduction

Metal silicides are technologically important for nanoelectronics fabrication due to possible direct growth and integration of low-dimensional materials on silicides and silicon. One example is the CVD growth of CNTs on Ni silicide for integration into MOSFET devices or Pt silicide for CVD grown graphene[28]. Here, we explore Ni silicides as a substrate for 2D Si films, commonly referred to as silicene, and $NiSi_2$ and Cu_3Si as a substrate for graphene. Silicides, such as Pt_3Si [28] as well as Ni, Fe, and Co silicides [29], have been experimentally proven to support a graphene layer. However, these studies have not looked at how the interface may affect a 2D layer's electrical properties through theoretical methods. Through these DFT simulations, the effects of the interface between the silicide and 2D layer on the 2D layer's band structure and DOS were analyzed. Through this analysis one may understand how a silicide would affect electrical properties of low dimensional 2D layer integrated on a Si platform using silicides as a growth layer.

4.2 Simulations of Silicene on $NiSi_2$

(This section was previously published as J.-Y. Cheng, M. K. Y. Chan, and C. M. Lilley, "Enabling direct silicene integration in electronics: First principles study of silicene on $NiSi_2$(111)," *Applied Physics Letters,* vol. 109, p. 133111, 2016. Linked here.)

Silicene is known to have a strong interaction with the metallic substrates used in fabrication methods [114-118]. One of the most common substrates for silicene growth is Ag(111) [114]. On Ag(111), the observed silicene layer is an adlayer of Si atoms precipitated

from the bulk Ag substrate due to the low solubility of Si in Ag [119]. Bonding between the silicene and Ag results in strong coupling of the electronic band structure and density of states with the 2D layer. Thus, it is necessary to explore alternative substrates for silicene fabrication where silicene may be more easily uncoupled by doping methods or removed from the substrate.

$NiSi_2$ may be a viable substrate for silicene growth, having been used extensively for the crystallization of amorphous and hydrogenated Si [120-122]. As a substrate, $NiSi_2$(111) is of particular interest due to its hexagonal-like structure similar to that of silicene. $NiSi_2$(111) and Si(111) have a low lattice mismatch of less than 0.4% at room temperature [49] and form an epitaxial interface [123]. Thus, $NiSi_2$(111) may be able to support a silicene layer. However, strong interactions may occur between silicene and $NiSi_2$, altering the 2D layer's electronic properties. To date, silicene has not been studied on $NiSi_2$. Since the electronic properties of silicene are dependent on the interaction with the underlying substrate, it is important to computationally model the silicene/substrate interaction. Herein, a detailed study on the stability and electronic properties of silicene atop a $NiSi_2$(111) substrate will be presented. Density Functional Theory (DFT) calculations were performed to determine whether silicene is stable atop $NiSi_2$. The binding energies between silicene and the substrate were used to identify the type of interaction at the interface. Substrate effects on the electronic Density of States (DOS) and the band gap were then studied. Additionally, hydrogenation effects between the silicide substrate and the silicene layer were studied. The effects of hydrogenation on the binding energies of the system and electronic properties of the silicene were also explored.

DFT calculations were performed using the Vienna Ab Initio Simulation Package (VASP©) [76, 85, 86]. The DFT methods were outlined in Chapter 2, and are detailed here for clarity. The PBE GGA exchange-correlation functional and the Projected Augmented Wave

(PAW) method was used, with PAW atom potentials supplied by VASP© [77]. The DFT-D2 Grimme correction for van der Waals interactions was included in all calculations [124]. All DFT calculations were performed using a 1×1 supercell (1-2 atoms per layer). Larger 3×3 supercell (9-16 atoms per layer) calculations were performed to check for long-range order. Energy cutoffs of 400 eV were used for all calculations. Reciprocal space was sampled using 14×14×1 and 4×4×1 k-point grids for relaxation and 24×24×1 and 8×8×1 for density of states, for the 1×1 and 3×3 supercell respectively. Ionic relaxations were halted when forces are below 0.05 eV/Å. Energy cutoffs and k-point mesh sizes were determined such that the total energy is converged to 0.02 eV/atom. Images of atomistic structures were produced using the VESTA© visualization tool [89]. For surface slab models, vertically symmetric $NiSi_2$(111) surface slabs with Ni or Si surface terminations were created with eight to nine layers. The surface slab models contain at least 15 Å of vacuum between periodic images. A Si(111)-$NiSi_2$(111) interface model was also considered, where periodic alternating slabs of Si(111) and $NiSi_2$(111) were combined with a minimum of eight to nine layers for each material. The four layers on either side of the interface were allowed to relax, while the remaining layers were fixed in position during relaxation.

The surface energy of the Ni- and Si-terminated $NiSi_2$(111) surface models were compared to determine relative stability. Experimentally, Si-terminated $NiSi_2$(111) surfaces are most common, as verified by ion scattering analysis and X-ray photoemission spectroscopy (XPS) experiments by other researchers [125]. Previous DFT calculations have shown that Ni-terminated $NiSi_2$(111) had a surface energy of 3.79 J/m^2, compared to Si-terminated $NiSi_2$(111) which had a surface energy of 1.37 J/m^2. Due to the high surface energy, Ni-terminated $NiSi_2$(111) is expected to be unstable and was not further considered in these simulations.

Henceforth, Si-terminated $NiSi_2$(111) will be referred to as $NiSi_2$. Hydrogen atoms were also added to the surface Si atoms to terminate the dangling bonds and such models will be referred to as H:$NiSi_2$. The theoretical stability of H:silicene and H:$NiSi_2$ was determined by calculating the binding energy ΔE of a hydrogen atom to each structure. DFT calculations of hydrogen on silicene resulted in a ΔE of -1.22 eV/(H atom), referenced to the energy of an isolated H_2 molecule. Due to the high binding energy of a hydrogen atom to silicene, it is assumed that a H:silicene layer would be stable and the hydrogen would not desorb during fabrication. Calculations of hydrogen on $NiSi_2$ resulted in a ΔE of -0.21 eV/(H atom). The binding energy of a hydrogen atom to $NiSi_2$ is low and the possibility of hydrogen desorption from a $NiSi_2$ surface may depend on experimental conditions.

Silicene was relaxed over $NiSi_2$ or H:$NiSi_2$ and hydrogenated silicene (H:silicene) was relaxed on $NiSi_2$. The H:silicene model has hydrogen terminated silicon atoms on both sides of the silicene layer. After ionic relaxation, the resulting buckling heights, interatomic distance, and interfacial distance were measured and their values are shown in Table 1. The structures, bond lengths and distances are shown in Figure 6. Compared to free-standing silicene, silicene on $NiSi_2$ (Fig. 1a) showed an increase in buckling height from 0.50 Å to 0.69 Å, accompanied by a small change in Si-Si interatomic distance from 2.25 Å to 2.31 Å. In comparison, silicene on H:$NiSi_2$ (Figure 6b) had a buckling height of 0.61 Å and Si-Si distance of 2.28 Å. The H:silicene layer atop $NiSi_2$ (Figure 6c) showed almost no change in buckling height and Si-Si distance compared to freestanding H:silicene. These results show that H:silicene retains the freestanding structure of H:silicene atop $NiSi_2$ while silicene does not.

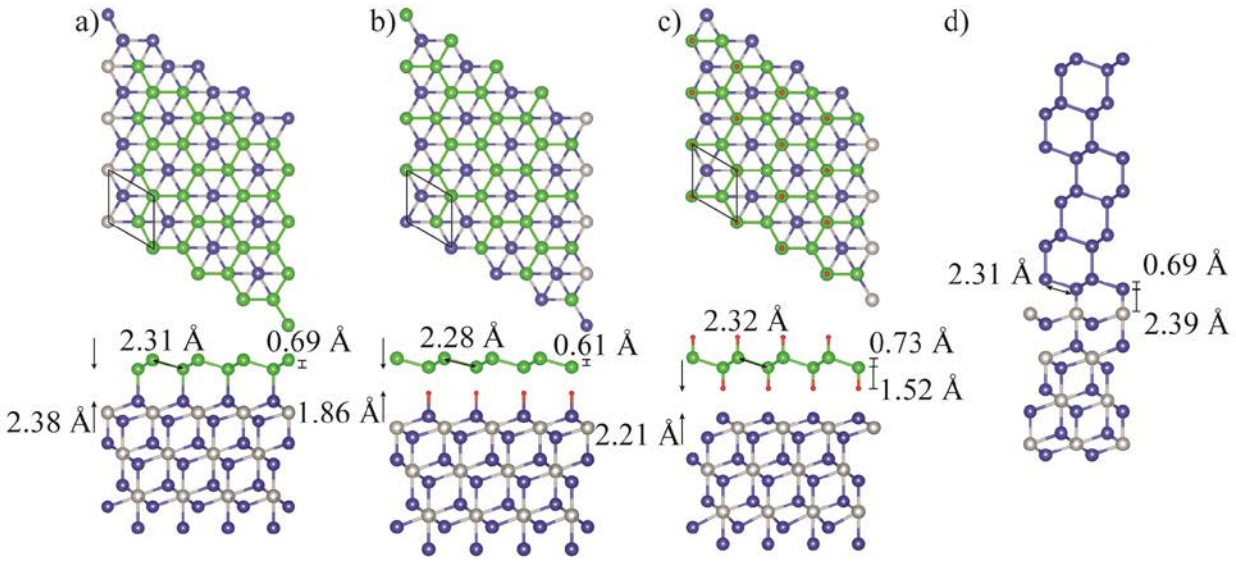

Figure 6 (a-c) Top and side view models of silicene on $NiSi_2$, silicene on H:$NiSi_2$ and H:silicene on $NiSi_2$ respectively (d) Side view of the bulk Si(111)-$NiSi_2$(111) interface. Red, green, blue, and silver atoms represent H, Si in the 2D layer, Si in $NiSi_2$ slab, and Ni, respectively. In (d), blue and silver atoms represent Si and Ni respectively.

Table 1 Summary of structural parameters of silicene and H:silicene, freestanding and atop $NiSi_2$ and H:$NiSi_2$.

System	Buckling Height Δ (Å)	Si-Si Interatomic Distance (Å)	Interfacial Distance (Å)
Freestanding Silicene	0.50	2.25	---
Silicene on $NiSi_2$ slab	0.69	2.31	2.38
Silicene on H:$NiSi_2$ slab	0.61	2.28	1.86
Freestanding H:Silicene	0.74	2.32	---
H:Silicene on $NiSi_2$ slab	0.73	2.32	2.21

We investigated how strongly silicene or H:silicene binds (hence couples) to $NiSi_2$ using DFT. The binding energies of the silicene layer were calculated from $E_{bind} = (E_{sub+2D} - E_{sub} - E_{2D})/n$ where E_{sub+2D} is the total energy of the substrate plus 2D layer (silicene or H:silicene), E_{sub} is the total energy of the substrate, E_{2D} is the total energy of the 2D layer, and *n* is the number of atoms within the 2D layer. E_{bind} for silicene on $NiSi_2$ was -0.33 eV/atom, indicating strong binding. This binding energy is similar to those of silicene atop metals such as Al (E_{bind} = -0.35 eV) and Mg (E_{bind} = -0.39 eV), calculated using DFT [126]. Hydrogenation was explored to decouple the 2D layer from the substrate. Thus, ionic relaxations of silicene atop H:$NiSi_2$ and H:silicene atop $NiSi_2$ were performed to study hydrogenation effects on binding energy and the electronic properties. The calculated binding energies for silicene atop H:$NiSi_2$ and H:silicene atop $NiSi_2$ were -0.074 eV/atom (-0.16 J/m^2) and -0.044 eV/atom (-0.19 J/m^2) respectively, indicating weak binding and decoupling of silicene from the substrate.

The interfacial distance, buckling height, and interface energy of bulk Si(111) and $NiSi_2$(111) was also calculated to compare with silicene on $NiSi_2$ (Figure 6d). The interfacial distance from the simulations was measured from the topmost Ni layer in $NiSi_2$ to the midpoint of the first and second Si layer of bulk Si(111) and measured 2.74 Å. The Si interatomic spacing measured from the simulations in the bulk Si(111) was 2.31 Å. To verify this model, the interfacial distance and Si interatomic spacing in bulk Si(111) was compared to experimentally measured values of 2.73 Å [127] and 2.34 Å [128] respectively and are found to be in close agreement. Also, the interfacial distance was measured between the nearest neighbor atomic layers of $NiSi_2$ and bulk Si. Using this method, the interfacial distance was 2.39 Å and is close to the interfacial distance of 2.38 Å found for silicene and $NiSi_2$ above. The bulk Si interatomic distance from the simulations was 2.31 Å and the buckling height at the interface was 0.69 Å and

also are close to the distance of 2.31 Å and buckling height of 0.69 Å for silicene on $NiSi_2$ found above. The interface energy was calculated to be -2.24 J/m^2 using the equation $E_{interface} = \left(E_{int} - E_{Si\ bulk} - E_{NiSi_2\ bulk}\right)/2A$. E_{int}, $E_{Si\ bulk}$, and $E_{NiSi_2\ bulk}$ represent the total energy of the Si and $NiSi_2$ interface, Si bulk, and $NiSi_2$ bulk respectively, while A is the cross-sectional area. Due to the similarities in interfacial distance, interatomic distance, and buckling height, our results strongly suggest that the silicene layer on $NiSi_2$ is relaxing towards the atomic positions of bulk Si at the Si(111)-$NiSi_2$(111) interface.

Simulated STM images were generated using partial charge density plots calculated in VASP©, generated at specific energy range relative to the Fermi energy. Figure 7 shows a charge density difference around the bonds between the 2D layer and substrate due to charge transfer from the $NiSi_2$ substrate to the silicene layer. The high binding energies of silicene atop $NiSi_2$ result in the significant change between the simulated STM images of freestanding silicene in Figure S2a and silicene atop $NiSi_2$ in Figure S2b. The simulated STM image in Figure 8b no longer matches the hexagonal pattern from the freestanding silicene image in Figure 8a. In the hydrogenated cases for Figure 7b and Figure 7c, the charge difference density shows little charge transfer between the substrate and 2D layer. Figure 7b shows an intermediate amount of charge density difference compared to Figure 7a and c. Figure 7d for H:silicene on $NiSi_2$ shows no charge transfer between the 2D layer and substrate in the charge density difference image and shows that there is less interaction between the 2D layer and the $NiSi_2$ substrate when the substrate is hydrogenated. Also, when comparing the simulated STM images of freestanding silicene and silicene atop H:$NiSi_2$ in Figure 8a and Figure 8c respectively, there are no discernable differences in the images. Similarly, there is no significant difference in the

simulated STM image of compared to freestanding H:silicene and H:silicene on $NiSi_2$ in Figure 8d and Figure 8c respectively.

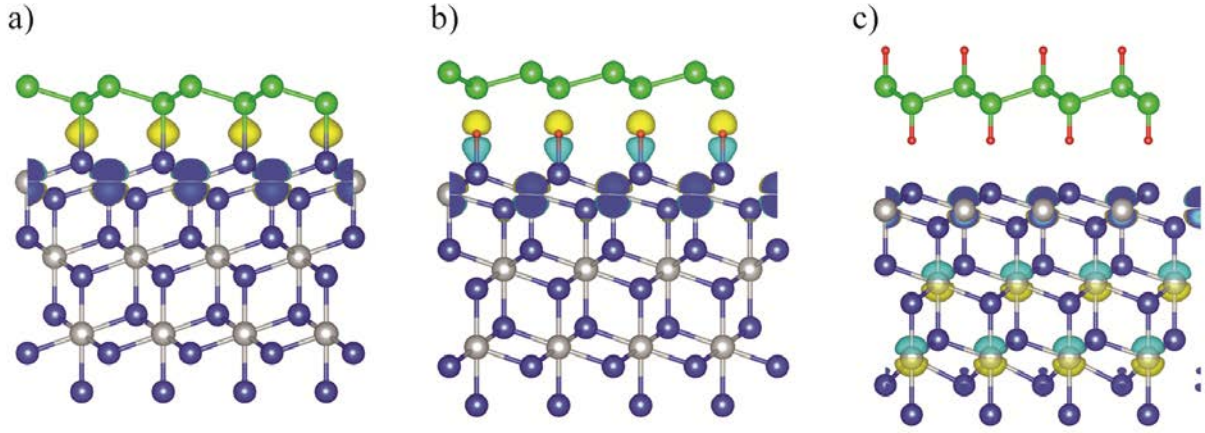

Figure 7. Side view of the charge difference density plots. (a) Silicene on a $NiSi_2$ slab, (b) silicene on a H:$NiSi_2$ slab, (c) H:silicene on a $NiSi_2$ slab. Red, green, blue, and silver atoms represent H, Si in 2D layer, Si in $NiSi_2$, and Ni, respectively. Isosurface value was set at 0.015 e/$Å^3$ where yellow and light blue isosurfaces represent negative and positive charge density difference respectively.

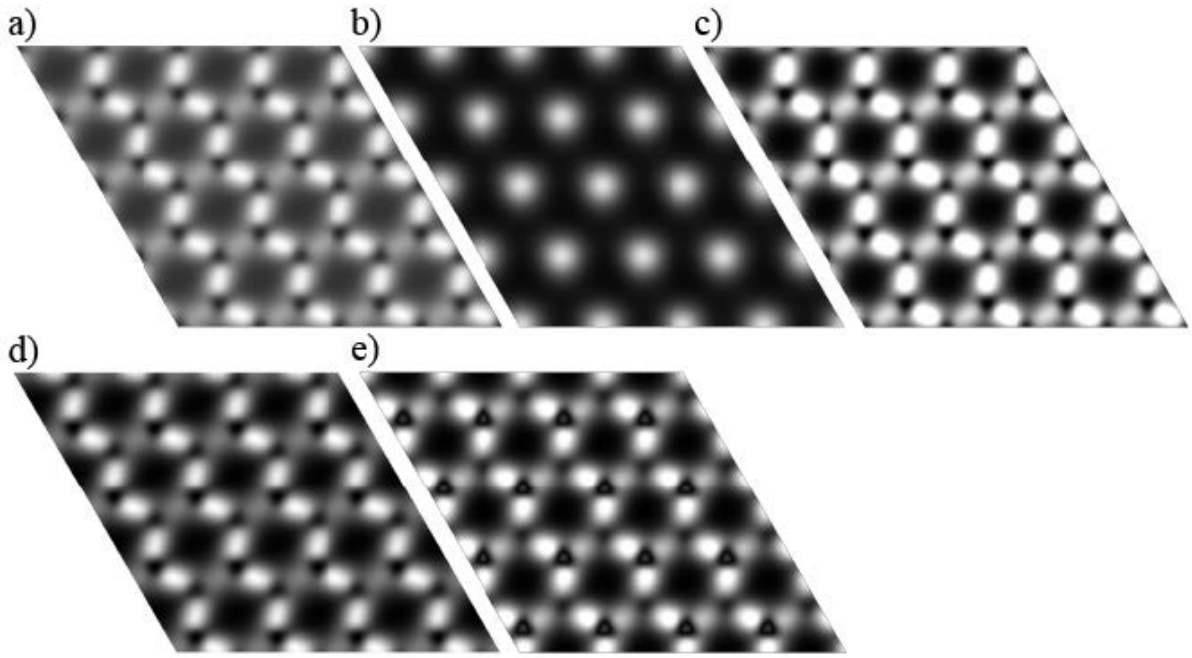

Figure 8 Simulated STM images for (a) freestanding silicene, (b) silicene on a $NiSi_2$ slab, (c) silicene on a H:$NiSi_2$ slab, (d) freestanding H:silicene, (e) H:silicene on a $NiSi_2$ slab. All images were simulated using a bias voltage of -2.0 V relative to the Fermi energy. A simulated bias voltage of -2.0 V was chosen due to the high DOS close to -2 eV for the simulated systems.

The strong bonding of silicene on $NiSi_2$ affects the band structure and DOS, shown in Figures 2b and 3b respectively. The band structure contribution from the silicene layer closely resembles that of bulk Si(111). The valence band maximum is seen above the Fermi level, around the K point in the Brillouin zone which, together with the high density of states around the Fermi energy (Fig. 2b and 3b), indicates that the 2D layer has metallic properties. The covalent bonding between the Si atoms from the 2D layer and the Si atoms along the surface of the $NiSi_2$ slab couples silicene to $NiSi_2$, rendering the silicene layer metallic.

Silicene on H:$NiSi_2$ had a slightly different band structure compared to freestanding silicene (Figure 9c-d). Hydrogenation of the $NiSi_2$ surface lowers the magnitude of the binding energy with silicene, and preserves the silicene band structure, due to van der Waals instead of

covalent bonding. The Dirac cone around the K point in the reciprocal space disappears for silicene on H:$NiSi_2$. Instead, parabolic valence and conduction bands around the K point in reciprocal space are observed, with a slight shift of 0.22 eV above the Fermi level. A zoomed-in comparison of the Dirac point and broadened bands of freestanding silicene and silicene on H:$NiSi_2$, respectively, can be seen in Figure 2f. The band gap of silicene on H:$NiSi_2$ at K is 0.14 eV. This band gap is similar to that calculated for silicene on K-intercalated $\sqrt{7}\times\sqrt{7}$ Ir, which has a band gap of 0.15 eV [126]. The disappearance of the Dirac cone and change in band gap may be due to the slight changes in the structure, including strain, buckling height, and Si-Si distances.

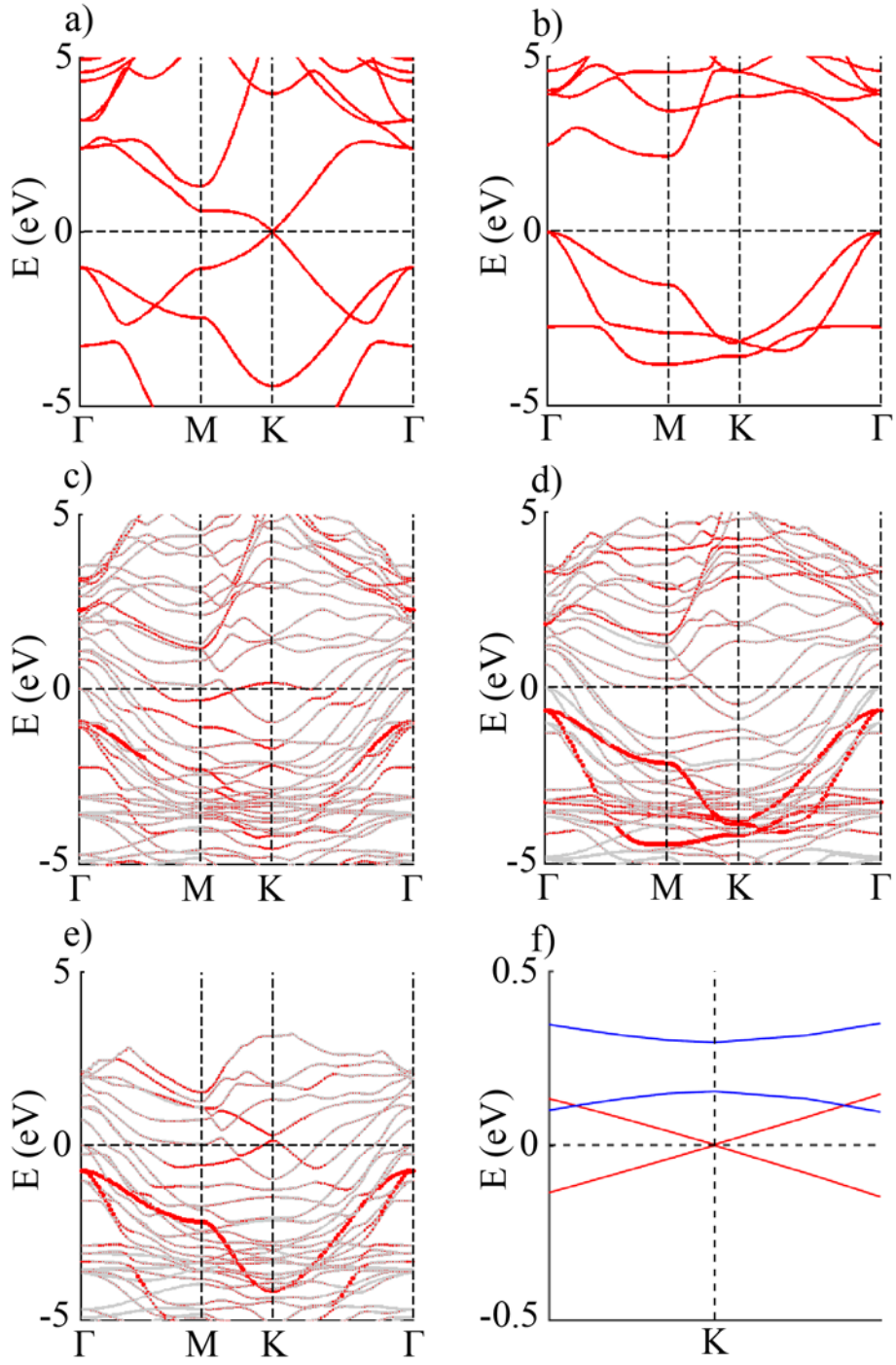

Figure 9 Band structures of (a) freestanding silicene, (b) silicene on H:$NiSi_2$, (c) silicene on a $NiSi_2$ slab, (d) freestanding H:silicene, (e) H:silicene on $NiSi_2$. Solid grey lines in (b), (c), and (e) represent the band structure of the supercell including the 2D layer and substrate. Red markings in those subplots represents the band structure contribution of the silicene or H:silicene layer. (f) Zoomed view of freestanding silicene (red) and silicene on H:$NiSi_2$ (blue) band structure around the K point in the Brillouin zone. The Fermi energy was set at 0 eV for all plots.

Although the band structure of silicene on H:$NiSi_2$ resembles that of freestanding silicene (Figure 10a,c), there is an observable change in the DOS (Figure 10a,c). In the DOS of the silicene layer, there is an increase in the DOS 0-2 eV below the Fermi energy. Broadened bands around the K point for silicene on H:$NiSi_2$ are seen in the total DOS of the silicene layer indicating some substrate contribution from the metallic $NiSi_2$ substrate despite hydrogenation.

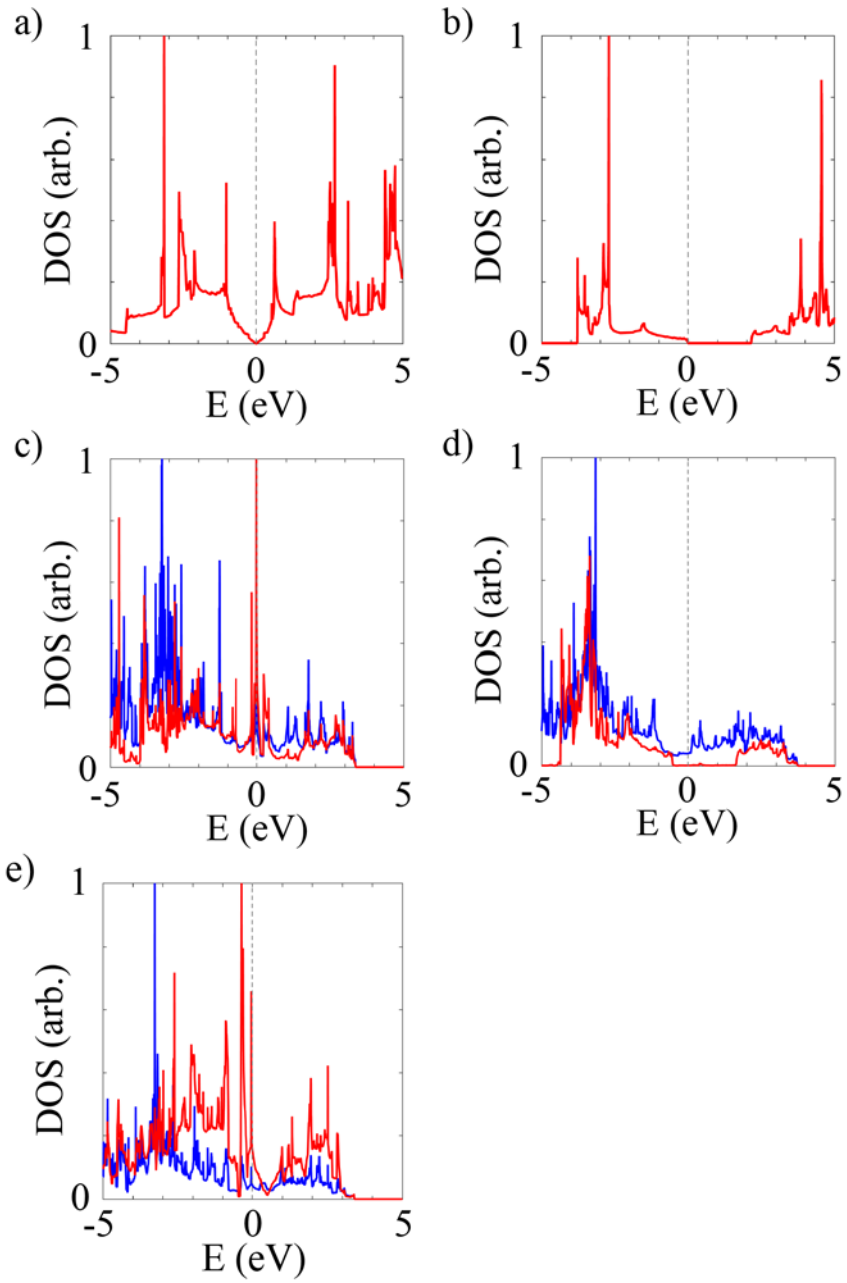

Figure 10 Density of States (DOS) of (a) freestanding silicene, (b) freestanding H:silicene, (c) silicene on $NiSi_2$, (d) silicene on a H:$NiSi_2$, (e) H:silicene on $NiSi_2$. Red and blue lines represent the 2D layer total DOS and total DOS of the supercell system (2D layer and substrate) respectively (DOS of silicene only).

A parabolic fit of the valence and conduction bands of silicene on H:$NiSi_2$ around the K point in the Brillouin zone was used to calculate the carrier effective mass using the equation $m_e^* = \frac{\hbar^2}{d^2E/dk^2}$ [68]. Silicene on H:$NiSi_2$ had a calculated electron and hole effective mass of $0.08m_0$, where m_0 is the free electron mass. This value is similar to the effective mass of $0.082m_0$ calculated for freestanding silicene under a vertically applied electric field of 1 V/Å [89]. The freestanding silicene band structure forms a linear dispersion around the K point in the Brillouin zone, where linear dispersions are characteristic of massless Dirac Fermions, and is consistent with published band structures[129-131]. The mean Fermi velocity in the M to K direction was calculated using $v_f = \frac{(dE/dk)}{\hbar}$, where v_f = 0.52×10^6 m/s and v_f = 0.39×10^6 m/s for freestanding silicene and silicene on H:$NiSi_2$ respectively, which are comparable to the published silicene Fermi velocity of 0.54×10^6 m/s which is considered to represent near-ballistic electron transport [129].

Hydrogenating the silicene layer instead of the $NiSi_2$ substrate also results in electronic decoupling, as seen in both the band structure (Figure 9e) and DOS (Figure 10e). The band structure of H:silicene on $NiSi_2$ preserves the properties of freestanding H:silicene (see Figure 9d-e). The indirect band gap of H:silicene on $NiSi_2$ is 1.97 eV compared to 1.99 eV for freestanding H:silicene and is in agreement with the calculated DFT indirect band gap of 2.0 eV for freestanding chair-like H:silicene [132] and in contrast to the Dirac point or small gap of silicene and silicene on H:$NiSi_2$. There is also little change to the DOS of H:silicene when placed on $NiSi_2$ (Figure 10d-e).

We have used DFT to show that silicene on $NiSi_2$ and H:$NiSi_2$, and H:silicene on $NiSi_2$, resulted in stable 2D Si formation with buckled hexagonal structures similar to freestanding

counterparts. Without hydrogen termination, the binding between silicene and $NiSi_2$ results in a bulk-Si-like interfacial structure and strong binding. By hydrogenating the $NiSi_2$ substrate, it was seen that the 2D electronic structure is preserved. The low binding energy and charge density plots show minimal interaction between silicene and H:$NiSi_2$, and likewise for H:silicene on $NiSi_2$. While freestanding silicene has a Dirac point with zero gap, hydrogenation of the substrate resulted in opening a gap of 0.14 eV for silicene on H:$NiSi_2$. Conversely, the 2 eV indirect band gap of H:silicene is preserved on $NiSi_2$. Additionally, electrons in silicene on H:$NiSi_2$ were calculated to have a Fermi velocity of 0.39×10^6 m/s. These calculations show that silicene and H:silicene still retain electronic properties similar to their freestanding values on H:$NiSi_2$ and $NiSi_2$, respectively. The preservation of the unique 2D properties of silicene makes $NiSi_2$ a promising substrate for silicene fabrication and integration into nanoelectronics. Future studies may look at doping or intercalation of other elements at the interface between silicene and other silicide substrates in order to tailor or decouple the electronic properties of silicene from substrates. The fabrication of silicene on $NiSi_2$, H:silicene on $NiSi_2$, and silicene on H:$NiSi_2$ is ongoing research.

4.3 Simulations of Graphene on $NiSi_2$ and Cu_3Si

Silicides, such as Pt silicide, have been used to grow high quality graphene through CVD methods[28]. Many silicides may be fabricated directly on Si substrates and are compatible with Si based fabrication processes. Growing graphene directly on these silicides would provide a method of direct integration of graphene on Si substrates without the transfer process. The silicide growth layer aids in the formation of graphene and can be used as contacts and interconnects in device designs. Ni and Cu silicides are of particular interest due to their use as contact materials in CMOS designs [25, 27]. To utilize integrated graphene on silicides in

electronic devices any possible substrate contributions between the silicide layer and graphene must be explored. This work explores how the graphene/silicide interface affects the DOS and band structure of a single graphene layer.

The DFT simulation parameters were nearly identical to those used for simulations of silicene on $NiSi_2$. The methods were outlined in Chapter 2, and additional details are presented here for clarity. DFT calculations were performed VASP© [76, 85, 86]. As with the previous silicene on silicide DFT simulations, the PBE GGA exchange-correlation function and the PAW method was used, with PAW atom potentials supplied by VASP© [77]. The DFT-D2 Grimme correction for van der Waals interactions was included in all calculations[124]. DFT calculations were performed using a 1×1 supercell which included 8-9 layers within the surface slab and a minimum of 15 Å vacuum space above the graphene layer. Initial interface orientation was determined by matching the lattice spacing of the graphene layer to the silicide surface so that the initial lattice mismatch of the two is less than 2%. Energy cutoffs of 600 eV were used for all calculations involving $NiSi_2$ or Cu_3Si surfaces. K-point mesh sizes of 8×8×1 were used for the relaxations involving $NiSi_2$ and Cu_3Si surfaces. Both surfaces utilized K-point mesh sizes of 12×12×1 for the band structure and density of states calculations. Relaxation simulations were performed with Gaussian smearing, DOS calculations were performed using tetrahedron method smearing with Blöchl corrections, and band structure calculations were performed with Methfessel-Paxton smearing. Band structure calculations included weighted band decomposition information to determine individual atom contributions to the total band structure. This band structure decomposition was used to visualize the contribution of the 2D layer to the overall band structure. Ionic relaxation of the systems were halted when forces are below 0.05 eV/Å. Energy cutoffs and k-point mesh sizes were determined such that the total energy is converged to 0.02

eV/atom. Images of atomistic structures were produced using the VESTA visualization tool [89]. Simulated STM images were generated using partial charge density plots calculated in VASP©, generated at specific energy range relative to the Fermi energy. Cells were not relaxed during ionic relaxation simulations for surface energy calculations.

A Si terminated $NiSi_2$(111) surface was used for Ni silicide simulations since the surface energy of Si-terminated $NiSi_2$(111) was determined to have a more stable surface energy than Ni-terminated surfaces [133]. For Cu_3Si(111) surfaces, the surface is terminated with both Si and Cu, but the surface energy of a Cu_3Si(111) surface has not been previously determined through DFT calculations to look at its stability. A symmetric surface slab was simulated through ionic relaxation and the total energy was compared to the bulk Cu_3Si rhombehedral structure to get calculate a surface energy of 0.31 eV/Å^2 (5.0 J/m^2). This Cu_3Si surface is thus considered to be relatively stable and was used to form the Cu silicide surface slab for these simulations.

The binding energy of graphene to $NiSi_2$ or Cu_3Si relate to how strongly the 2D layer is electronically coupled to the silicide layer. The binding energy of the graphene layer was calculated using the binding energy equation whose parameters are similar to those presented in Chapter 4.2. A binding energy of -0.05 eV/atom was calculated for graphene on $NiSi_2$ and -0.06 eV/atom for graphene on Cu_3Si. The binding energy calculations take into account van der Waals forces since the relaxation simulations were performed using the DFT-D2 van der Waals corrections. The low binding energy between graphene and both silicides shows that the interaction at the interface is assumed to be due to van der Waals interaction. DFT simulations of graphene on pure metals such as Cu and Ni had calculated binding energies of -0.037 eV/atom and -0.038 eV/atom respectively [95, 134]. The larger binding energies in this work may be due to the compositional difference and surface termination of the metal silicide layers compared to

the pure metal layers used as a surface slab. The low binding energy atop $NiSi_2$ and Cu_3Si are associated with little to no substrate and graphene layer electronic interaction leading one to believe that substrate contributions to the electronic properties to the graphene layer are minimal.

The interfacial distance between graphene on $NiSi_2$(111) and Cu_3Si(111) was calculated after relaxation simulations. Between graphene and the topmost layer in $NiSi_2$ the interfacial distance is 3.12 Å. In the graphene on Cu_3Si simulation the interfacial distance is 3.24 Å. The interfacial distance between graphene and Cu_3Si or $NiSi_2$ is similar to the interfacial distance of graphene on metallic substrates such as Cu(111) and Ni(111) of 3.58 Å and 3.50 Å respectively [95, 134]. These interfacial distances and low binding energy are thought to be due to van der Waals interaction at the interface.. The weak interaction between the graphene layer and the silicide layer may be seen in Figure 11 and Figure 12, which show the charge difference density of graphene on $NiSi_2$ and graphene on Cu_3Si respectively. The weak interaction may be observed by the concentration of charge difference density isosurfaces around the 2D layer and not between the graphene layer and silicide. Due to the charge concentration around the graphene layer atop both silicides, it is assumed that there is little to no charge transfer between the 2D layer and the silicide substrate.

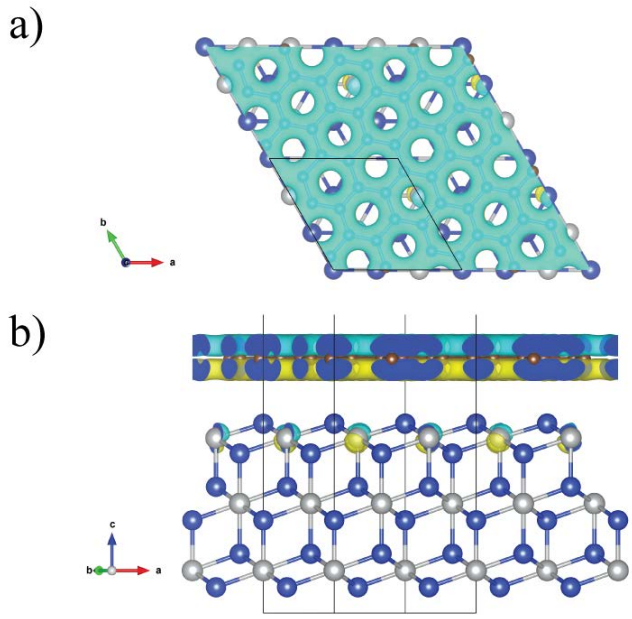

Figure 11 Charge difference density plot of graphene on $NiSi_2$. (a) Top view and (b) side view of graphene on $NiSi_2$(111). Brown, blue, and grey atoms represent C, Si, and Ni atoms respectively.

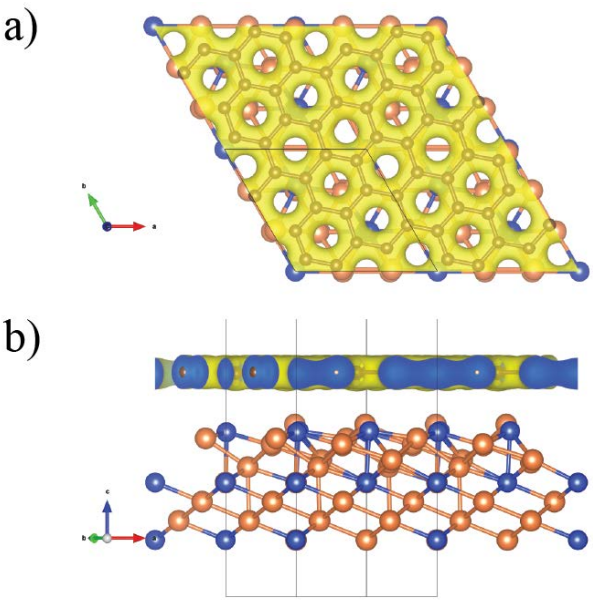

Figure 12 Charge difference density plot of graphene on Cu_3Si. (a) Top view and (b) side view of graphene on Cu_3Si(111). Brown, blue, and orange atoms represent C, Si, and Cu atoms respectively.

Based upon the low binding energy and CDD plots, it is assumed that silicide has little to no effect on the electronic properties of the graphene layer. Graphene on $NiSi_2$ retains linear bands around its Dirac point, but shows a shift of the Dirac point position to -0.46 eV below the Fermi level (where that Fermi level for the band structure and DOS was set to 0 eV) as seen in Figure 13. This shift of the Dirac point below the Fermi-level may indicate a shift of the graphene layer to n-type. This is different to the Dirac point shift of graphene atop Ni(111) which has a shift of +0.13 eV above the Fermi energy [134]. The difference in Dirac point shift may be due to the surface termination of the $NiSi_2$(111) surface. A negative Dirac point shift of -0.4 eV was calculated in graphene over Si terminated SiC(111) surface [135, 136]. The Si surface termination of $NiSi_2$(111) may cause the negative Dirac point shift differing from the Ni(111) surface. The gap at the K point in the Brillouin zone is 2.8 meV, compared to freestanding graphene's band gap of 0 eV. The non-zero DOS around the Fermi level indicate metallic characteristics due to the substrate contribution as the $NiSi_2$ layer itself is metallic. However, the DOS of the graphene layer below the Fermi energy show there is a high concentration of electrons around -0.46 eV, which coincides with the Dirac point.

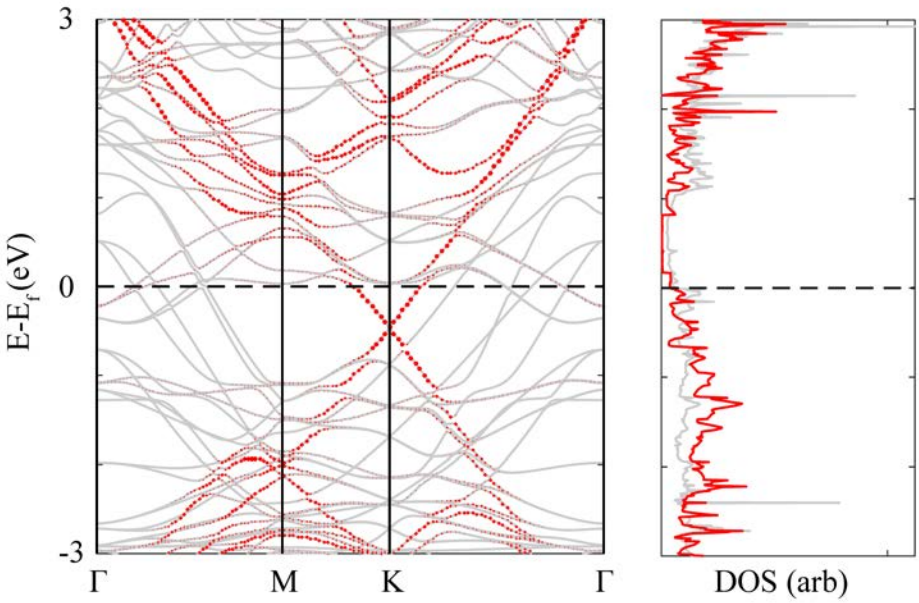

Figure 13 Band structure and DOS plot of the supercell (black) and decomposed graphene contribution (red) on $NiSi_2$. The Fermi energy of both plots was set to 0 eV.

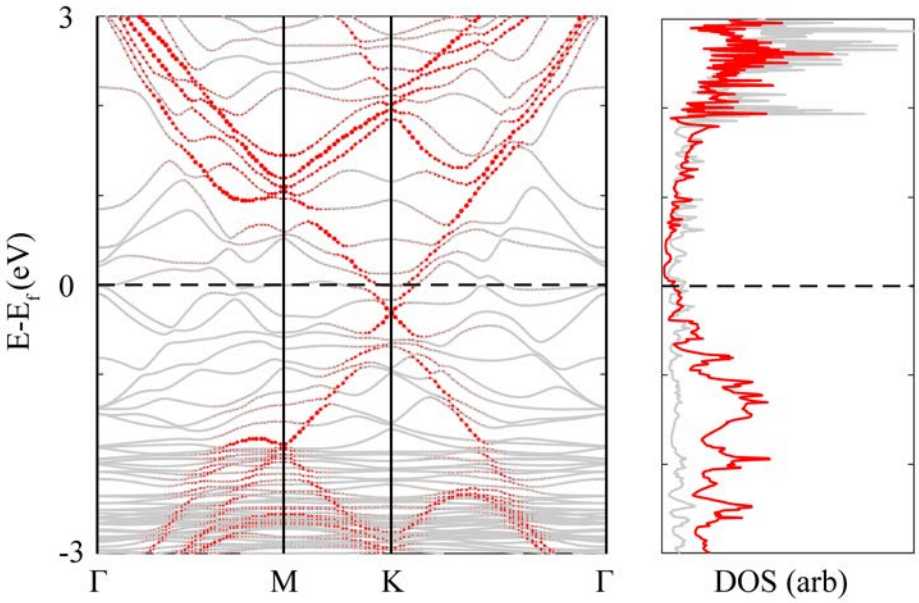

Figure 14 Band structure and DOS plot of the supercell (black) and decomposed graphene contribution (red) on Cu_3Si. The Fermi energy of both plots was set to 0 eV.

Band structure and DOS simulations of graphene on Cu_3Si yielded similar results and can be seen in Figure 14. The band structure also shows a linear dispersion around the K point in the Brillouin zone, however the range of its linear dispersion is shorter than that of graphene on $NiSi_2$. The Dirac point can still be observed in the band structure of the graphene layer contributions to the band structure shown by the red coloring of Figure 14. There is a shift of the Dirac point is -0.31 eV below the Fermi level. This shift in Dirac point is similar to the shift of the Dirac point of graphene on Cu(111) to -0.41 eV below the Fermi level [134].

Analyzing the π and π^* bands around the K point in reciprocal space reveals that the graphene layer on $NiSi_2$ or Cu_3Si retains linearity around the Dirac point. Linear dispersions are characteristic of massless Dirac Fermions. The massless Fermions of freestanding graphene from M to K in the Brillouin zone is in agreement with findings from other researchers who have simulated freestanding graphene [18, 81, 94, 137]. Due to this linearity, using the electron effective mass equation $m_e^* = \frac{\hbar^2}{d^2E/dk^2}$ yields an electron effective mass of 0 m_0·kg [68]. Similarly, the calculated hole effective mass is also 0 m_0·kg. Thus, the equation $v_f = \frac{(dE/dk)}{\hbar}$ [68] was used to calculate the Fermi velocity in the M to K Brillouin direction, resulting in values of $v_f = 1.5\times10^6$ m/s in graphene atop $NiSi_2$ and $v_f = 1.3\times10^6$ m/s in graphene atop Cu_3Si. This is of the same order as other published graphene Fermi velocity values of 2.6×10^6 m/s and can be considered to have ballistic electron transport [10].

Density Functional Theory calculations were used to show that the interface between graphene and $NiSi_2$(111) or graphene and Cu_3Si(111) slabs may result in the graphene layer retaining its unique electronic properties, specifically its ballistic electron transport around the Dirac point. The low binding energy and charge density plots show minimal interaction between

the graphene and silicide surface. The shift of the valence band maximums below the Fermi energy indicates that graphene on a $NiSi_2$ slab is now n-type. Additionally, electrons in graphene on a $NiSi_2$ slab were calculated to have a Fermi velocity of 1.5×10^6 m/s. Similarly, for graphene on a Cu_3Si slab was calculated to have a Fermi velocity of 1.3×10^6 m/s. These calculations show that graphene still retains electronic properties similar to its freestanding values atop these two silicides. The preservation of the unique 2D properties of graphene atop $NiSi_2$ and Cu_3Si shows promise for using either silicides for direct fabrication and integration into Si substrates for nanoelectronics. Future studies will look at doping or intercalation of other elements at the interface between graphene and a silicide surface in order to tailor the band gap.

4.4 Concluding Remarks

The first objective of this thesis was to use DFT simulations to study the properties of 2D films on silicides. DFT simulations on silicene on $NiSi_2$ showed that although epitaxial to each other, silicene tends to buckle towards the bulk Si positions of the $Si/NiSi_2$ interface. Additionally, the strong binding energy results in the silicene layer displaying highly metallic properties and losing 2D characteristics such as the linear bands around the Dirac point. In order to decouple a silicene layer from $NiSi_2$, hydrogenation of the $NiSi_2$ or the silicene layer itself was necessary. Hydrogenation resulted in the silicene or H:silicene layer retaining much of their 2D properties.

Simulations of graphene on $NiSi_2$ and Cu_3Si did not require hydrogenation to decouple the 2D layer and silicide. This is due to the low binding energy of graphene to either silicide indicating that the interface interaction is due to Van der Waals bonding. The weak binding energy of graphene on $NiSi_2$, in particular, can also be seen in the charge difference density plots

and the retention of linear bands around the Dirac point. Graphene was able to maintain a zero electron effective mass and essentially ballistic electron transport characteristics.

Through these DFT simulations it was shown that silicides can have a minimal effect on the band structure and DOS of a graphene layer on silicides such as $NiSi_2$ and Cu_3Si. However, strong interaction between another 2D layer, such as silicene, and a silicide layer of $NiSi_2$ can result in the 2D layer taking on metallic electrical characteristics of a silicide substrate. Depending on the 2D layer interaction with a silicide layer, low dimensional structures may retain their unique freestanding properties. Additionally, hydrogenation, using other silicide compositions, doping, or intercalation may be used to further tune the electrical properties of a 2D layer. This reinforces the importance of surface termination to interface and substrate engineering on the electronic properties of the low dimensional layers.

CHAPTER 5 GRAPHENE GROWTH ON SILICIDES

5.1 Introduction

Metal silicides, such as Cu and Ni silicides, have been used extensively as CMOS contacts and interconnects, and more recently have been studied as QD contacts However, technical challenges to utilizing silicides are their high oxidation and diffusion rates, that result in electrical and mechanical failure [138-140]. Graphene is of interest as an encapsulating layer for Ni, Fe, and Co silicides, as it has been shown to form a diffusion and oxidation barrier [29, 141, 142]. In addition, direct fabrication methods of graphene on Si and silicide platforms have been studied [143, 144]. For direct fabrication on semiconductors, Ge(001)/Si(001) and Si(111) substrates have been used to show that graphene could be fabricated using CVD methods. However, the graphene quality and carbide formation required further improvement to each of those processes respectively. An intermediate layer, such as a silicide, epitaxially grown on a Si substrate may be advantageous to direct growth on semiconductors. CVD graphene growth with silicides, using Pt_3Si, resulted in large graphene grain sizes and high quality single layer films [28, 29]. However, the CVD temperature resulted in a roughened surface that required transfer of the graphene for integration into a device. Thus, there is still a need to continue exploring the use of Si substrates and silicides for direct graphene fabrication and integration. Although, previous DFT simulations have shown that silicides such as $NiSi_2$ and Cu_3Si support a graphene layer, the experimental growth of graphene has not yet been attempted atop these silicides fabricated on Si substrates. This chapter addresses the proof of concept of using these silicides to fabricate graphene on Si.

5.2 CVD Graphene Growth on Cu_3Si Fabricated on Si Substrates

This research focused on directly growing graphene on a Si(111) crystal using Cu silicide as the catalytic surface. The goal is to demonstrate whether graphene can be grown directly on a Si substrate using a bulk CVD process while preventing silicon carbide formation. Ideally, metals that form silicides can be patterned and annealed on Si substrates to use as catalytic layers for direct graphene growth. Thus using a silicide, such as Cu silicide, for growth as well as electrical contacts would be of technological importance for future graphene on Si devices.

Si wafers were purchased from Virgina Semiconductor. They are As doped (0.001-0.0006 Ω·cm resistivity) with (111) orientation. Si(111) samples were dipped in a BOE solution for 2 minutes to remove any oxide. After the BOE solution they were rinsed in DI water and dried using N_2. 100 nm of Cu was deposited on the Si(111) samples using e-beam deposition in a UHV chamber (~10^7 mbar).

A MTI™ CVD furnace was used for the CVD growth. Ar/H_2 (4.687 mole % H_2) gas was flowed through the chamber at 200 sccm throughout the entire CVD process. Once the heated tube reached the temperature set point of 900˚C a mixture of Ar/CH_4 (500.2 ppm CH_4) was flowed into the chamber at 100 sccm for 60 minutes. A maximum temperature of 900˚C for the CVD process was chosen to stay under the SiC formation temperature. After 60 minutes the Ar/CH_4 flow was stopped and the chamber was cooled back to room temperature while the Ar/H_2 mixture was flowed through the tube. A graph of the process temperature and flow rate as function of time may be seen in Figure 15.

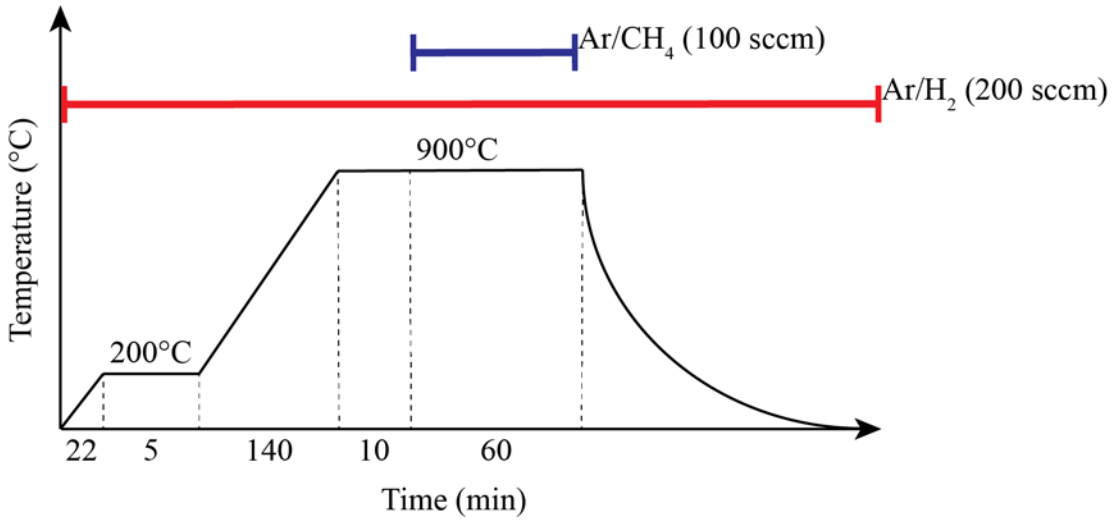

Figure 15 Representation of the standard CVD graphene growth on Cu foil process times, temperatures, and gas flows. Temperature and time axes are not to scale and are exaggerated for visual purposes.

A Renishaw inVia Raman microscope was used to perform the Raman spectroscopy. Raman spectra were taken using a 442 nm laser with a 1800 L/mm grating, the maximum laser power was 35.1 mW. Measurements were taken with a laser power between 5-10% of the maximum power to minimize heating of the sample. Measurements were taken using a magnification of 100x, where the laser spot size at 100x magnification is 0.2 μm.

A Bruker D2 Phaser XRD system was used for the XRD measurements. Samples were spun at a rate of 60 RPM during the measurements. Measurements were taken over 2θ range of 10-90° with an X-ray power of 30 kV and 10 mA using a 1 mm slit.

An optical microscopy image can be seen in Figure 16 alongside Raman intensity maps centered around the wavenumbers of 2750 cm^{-1}, 1581 cm^{-1} and 1351 cm^{-1}. These wavenumbers correspond to the 2D, G, and D carbon peaks [110, 111]. A map of the signal intensities at these three Raman wavenumbers may be seen in Figure 16b-d. The presence and sharp peak of the 2D peak is indicative of graphene. The peak intensity ratio of G to 2D may be used to estimate the

number of graphene layers present, and the D peak intensity correlates to the amount of disorder and defects present in the graphene or graphite layers [110]. G to 2D peak ratios of less than one indicate single layer graphene, ratios of around 1 indicate bilayer graphene, and ratios of around two indicate three or more graphene layers. Further increasing ratios of G to 2D peaks and broadening the 2D peak indicate the transition from graphene to graphite. In Figure 16e, one can see the approximate number of graphene layers over a scanned area based upon G to 2D ratios. Over the large triangular island roughly 1 layer of graphene is present, but individual wavenumber maps from Figure 16d show that there are a high number of defects over this particular structure due to the high D peak intensities. While scanning over the smaller islands, 1-2 layers of graphene were found to be more common with a smaller number of defects. In some cases, copper silicide islands having up to 3 layers of graphene were found and are shown by the red colored areas.

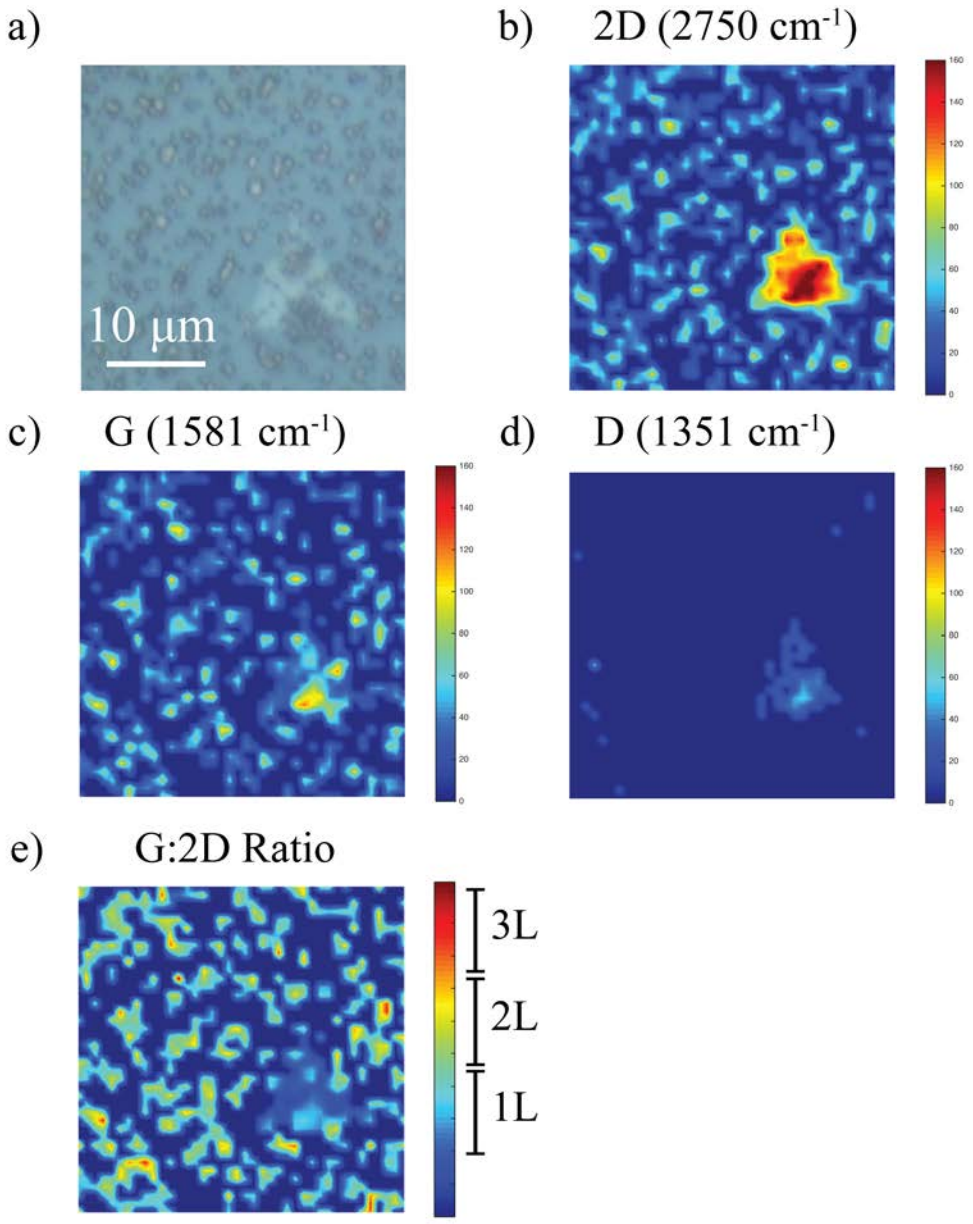

Figure 16 Raman maps of the optical microscope image shown in (a). (b-d) show Raman maps of intensities centered around wavenumbers 2750 cm^{-1} (2D), 1581 cm^{-1} (G) and 1351 cm^{-1} (D) respectively. Color bars show the relative signal intensity in arbitrary units. Derived Raman map (e) indicates the approximate number of graphene layers based upon the G:2D Raman peak intensity ratio.

An example of the Raman point spectra over graphene on Cu_3Si may be seen in Figure 17b. A comparison of Raman spectra were taken over an annealed Cu_3Si island without graphene (blue), over an annealed Cu_3Si island covered graphene (red), over a bare Si area between graphene covered Cu_3Si islands (green), and on a graphene covered Cu_3Si island left in ambient conditions for 3 months (purple) and is shown in Figure 18a. The zoomed inset focusing on the graphene related Raman shift peaks is denoted by the dashed box, which is magnified and shown in Figure 18b. In all four spectra a Si peaks may be seen at 520 cm^{-1} and 2330 cm^{-1} due to the Si substrate. The broad peak at 250 cm^{-1} in the blue spectra, without graphene growth, is due to the formation of a $CuSiO_3$ [145], most likely formed due to exposure to an ambient environment since Cu silicides and Si oxidize rapidly without an encapsulation layer [140, 146]. In the red spectra of the graphene covered Cu_3Si island, the ratio of G:2D is about 0.8, indicating 1-2 layers of graphene. There is a small D peak present showing some defects in the graphenes. No SiC peaks were observed over the samples even after CVD processing using methane, however SiO_2 was observed over the bare Si surface between the islands at broad peaks close to 643, 808, and 978 cm^{-1} [147, 148]. Annealing Cu on Si(111) without introducing the CH_4 gas during the CVD process resulted in no C formation as seen in the blue spectra. Cu_3Si, like Cu, is Raman invisible and no Cu related peaks were observed. Raman spectra were also taken after leaving a graphene coated sample out in ambient conditions for roughly three months. This measurement is shown by the green spectra. The G:2D ratio of the green spectra is roughly 0.5 indicating single layer graphene, with a D peak intensity also indicating the presence of defects. The spectra does not show the presence of any Cu oxides under the graphene coated Cu_3Si islands despite being left exposed in an ambient environment. This shows that the graphene layer is effective in preventing the oxidation of the Cu_3Si island it is covering.

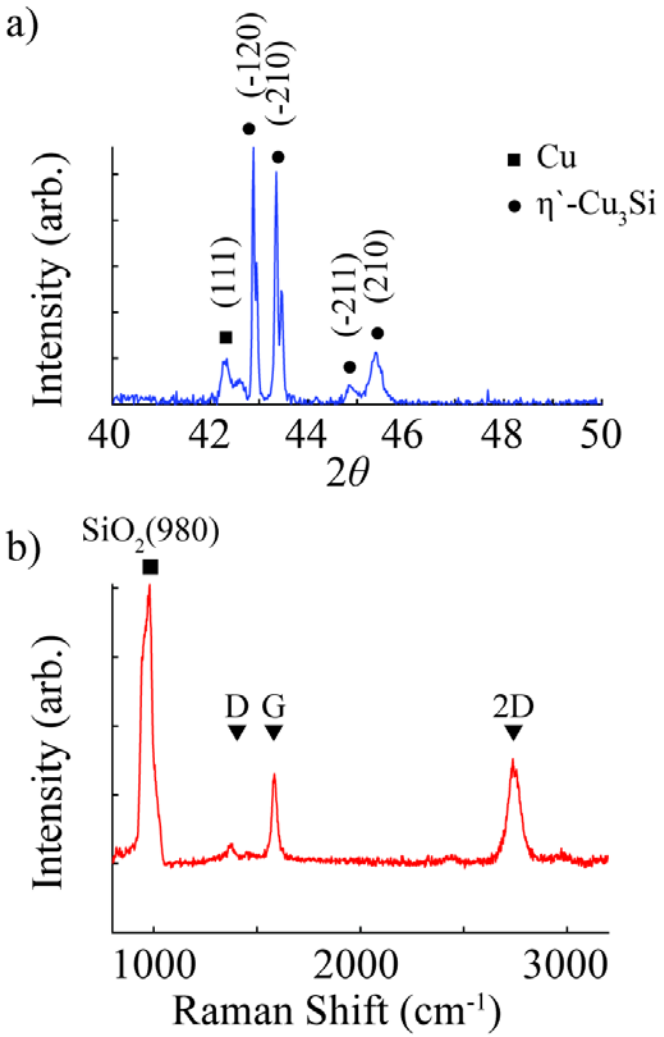

Figure 17 Normalized Raman (a) and XRD (b) spectra corrected for background slope. Spectra in (a) were taken over annealed Cu_3Si island without graphene (blue), over an annealed Cu_3Si island covered graphene (red), over a bare Si area between graphene covered Cu_3Si islands

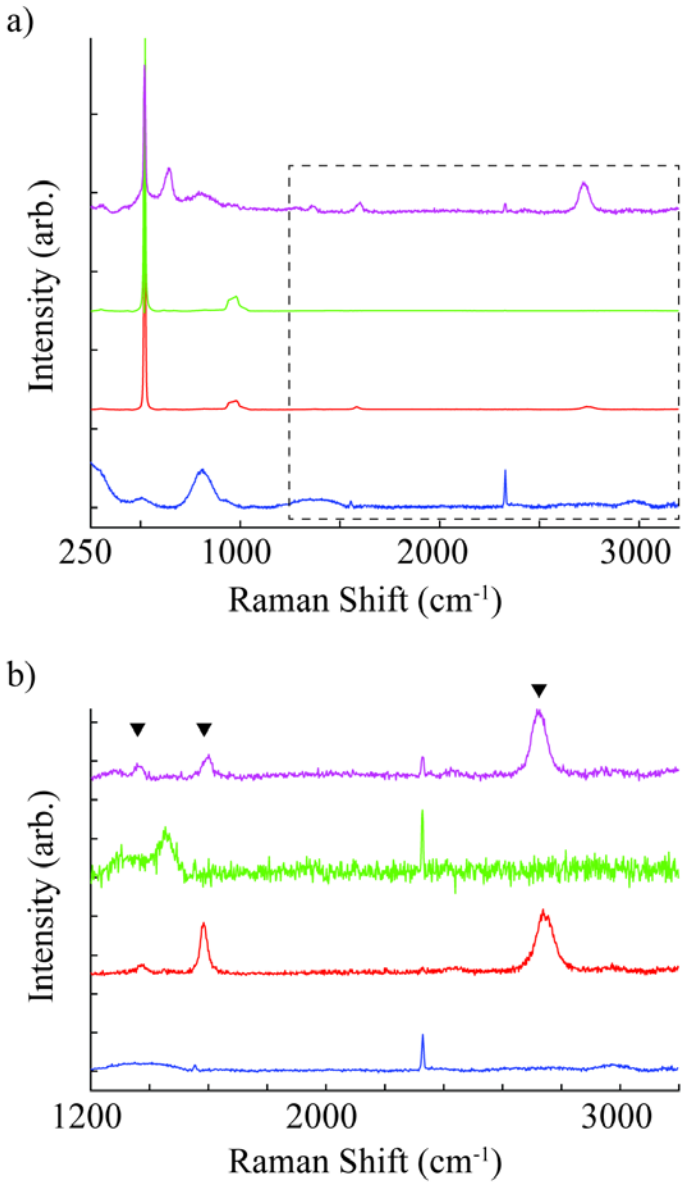

Figure 18 Normalized Raman spectra over (a) 250 to 3200 cm^{-1} Raman shift and (b) a zoomed Raman shift plot around 1200 to 3200 cm^{-1} denoted by the dashed inset in (a). Spectra were corrected for background slope. Spectra were taken over an annealed Cu_3Si island without graphene (blue), over an annealed Cu_3Si island covered graphene (red), over a bare Si area between graphene covered Cu_3Si islands (green), and over a graphene covered Cu3Si island left in ambient conditions for three months (purple).

The composition of Cu_3Si islands was confirmed using XRD. It is assumed that a majority of the Cu was turned into a silicide of η'-Cu_3Si composition due to the surface phase reaction formation method as the sample was heated to a maximum temperature of 900°C [149, 150]. Crystallographic planes that match those of η'-Cu_3Si may be seen in Figure 17a. Two definitive η'-Cu_3Si planes are (-211) and (210) found at 2θ values of 44.9° and 45.2° respectively [151, 152]. Two other possible η'-Cu_3Si planes present are (-120) and (-210) found at 42.9° and 43.4° respectively [153]. In addition a Cu (111) peak was found at 42.4° which may be due to unreacted Cu on the Si(111) surface. This Cu peak may disappear if the sample is annealed for longer periods of time or a thinner layer of Cu is deposited.

In this experiment graphene was successfully grown atop Cu_3Si islands using CVD thus directly integrating graphene on a Si(111) substrate without the transfer process. The Cu_3Si islands were formed during the CVD heating process and acted as a catalytic layer for graphene growth. Raman spectroscopy was used to confirm the presence of 1-3 layers of graphene of varying quality over the Cu_3Si islands without the formation of SiC over the exposed Si substrate despite the high temperature growth. Graphene also prevented the oxidation of the Cu silicide island after being exposed to an ambient environment for three months. XRD measurements confirmed the formation of Cu_3Si during the CVD process, specifically of the η'-Cu_3Si composition. Future work will include electrically characterizing the graphene on silicides to further study the quality of graphene, altering the CVD process parameters to adjust the surface quality of the graphene layers on different Si substrate orientations, and growing graphene on lithographically patterned silicides.

5.3 Attempted CVD of Graphene on $NiSi_2$

Attempts to directly grow graphene on $NiSi_2$ using CVD were unsuccessful. Previous experiments of graphene on Ni silicides were performed on SiC substrates [154, 155]. Si substrates were coated in Ni and then heated. The diffusion of the Ni into the SiC and silicidation of Ni with Si in the substrate formed Ni silicides, which precipitated carbon towards the surface of the sample eventually forming graphene [154, 155]. The same CVD method for graphene growth on Cu_3Si on Si(111) was used for $NiSi_2$ on Si(111) in our experiments. The growth temperature was set between 800-1000˚C and Ar/H_2 and Ar/CH_4 mixtures with the same flow rates and H_2:CH_4 ratio were used in this experiment. The formation of $NiSi_2$ was verified through Raman spectroscopy by the presence of peaks at 220 cm^{-1} and 240 cm^{-1} shown in Figure 19. The CVD maximum process temperatures were lowered below the formation temperature of Ni carbide. Raman peaks confirm the presence of $NiSi_2$ formed during the heating steps of the CVD process. Deposition of thicker initial Ni layers of 300 nm were attempted to see if a higher Ni content would aid in graphene formation. However, these thicker layers ended up delaminating from the Si substrate. Raman peaks in Figure 19 are denoted by red triangles at 229, 284, 320, 376 cm^{-1}. These peaks align closely with those associated with $NiSi_2$ at 232, 297 and 320 cm^{-1}, and a broad double peak between 350-402 cm^{-1} .

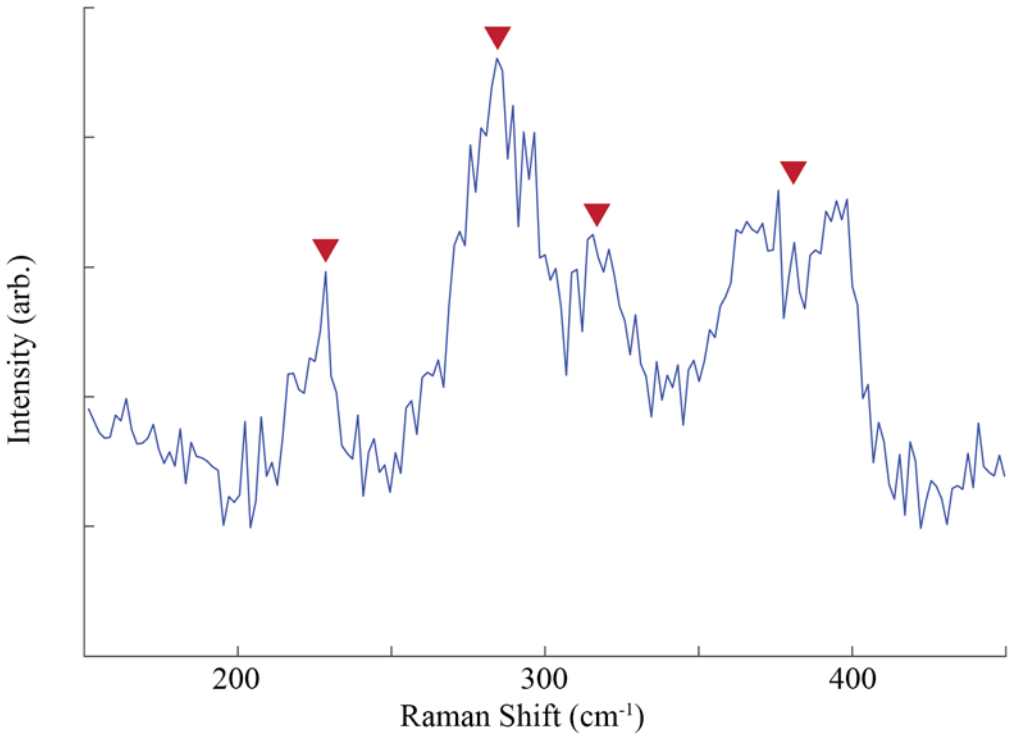

Figure 19. Raman spectroscopy (514 nm laser, 13.71 mW power, 20 sec dwell time, 5 acquisitions) of sample after CVD processing of Ni deposition on a Si(111) substrate. Peaks centered around 229, 294, and 320 cm^{-1} and a double peak centered around 376 cm^{-1} confirm the presence of $NiSi_2$ formed during the heating process. No graphene peaks were observed over the sample.

5.4 Ethylene Decomposition on Sub-Monolayer Surface Reconstructions of Ni √19x√19

Another attempt at growing graphene on Ni-silicide involved ethylene decomposition over sub-monolayer Ni √19×√19 surface reconstructions over a Si(111) substrate. Ethylene decomposition was performed within the preparation chamber of the Omicron™ STM system. Ethylene was leaked into the preparation chamber until the pressure rose to 10^{-6} mbar. This chamber pressure was maintained for 30 minutes while the Ni √19/Si(111) sample was heated using direct current to 600˚C in attempt to crack the ethylene molecules over the surface to deposit C. After the ethylene decomposition samples were analyzed using Raman spectroscopy ex situ from the Omicron™ UHV system. Raman spectroscopy again confirmed the presence of

$NiSi_2$. The presence of $NiSi_2$ versus the Ni-silicide surface reconstruction may be due to elevated temperatures and the high diffusion rate of Ni in Si causing these the formation of silicide crystals. Carbon peaks at 1363, 1594, and 2714 cm^{-1} show the presence of graphite. Graphite is confirmed due to the combined base of the D and G peak, as well as the D and G peak ratios to the 2D peak. Another marker of graphite is the presence of a D+G peak at 2972 cm^{-1} close to the 2D peak representing the disorder of graphite layers. These are close to Raman shift peak positions at 1360, 1580, 2710, 2940 cm^{-1} and represent the carbon D, G, 2D, and D+G Raman peaks respectively [110, 111]. These four peaks are highlighted by the red triangle markers shown in Figure 20. Graphite Raman signatures at known D, G, and 2D peaks differ due to the presence of a D+G peak, as well as combination of the peak bases of the D and G peak, and the relative intensity of the D and G peak to the 2D peak.

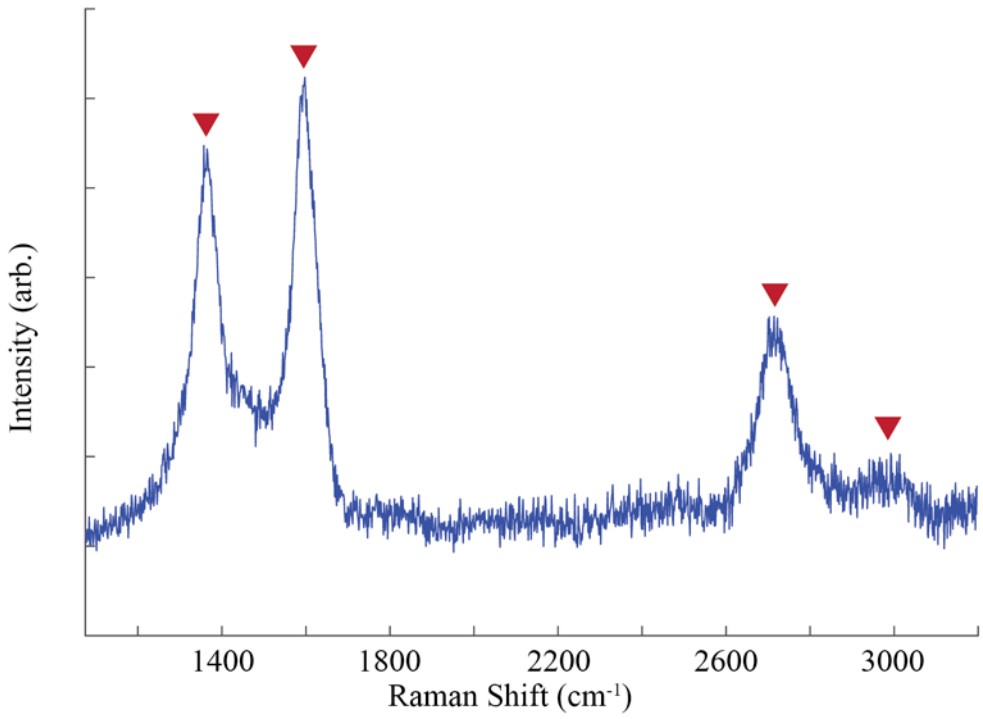

Figure 20. Raman spectroscopy of sample after ethylene decomposition showing the presence of graphite (514 nm, 13.71 mw, 10 sec dwell). Red arrow markers are placed at the peaks centered over Raman shifts of 1363, 1594, 2714, and 2972 cm^{-1} which represent the D, G, 2D, and D+G peaks respectively.

5.5 Concluding Remarks

Proof of concept experiments growing graphene directly on Si(111) using a Cu_3Si were successful. Raman spectroscopy confirmed the presence of 1-3 layers of graphene of varying quality over the surface. XRD measurements confirmed the formation of Cu_3Si. Other initial attempts of CVD grown graphene on $NiSi_2$ were unsuccessful, however ethylene decomposition over Ni silicide monolayers did result in graphite formation. Cu_3Si is the more promising material to use for graphene growth on Si. The higher ratio of metal to silicon in the Cu_3Si composition may aid in the formation in graphene and should be explored further.

CHAPTER 6 CHARACTERIZATION OF SUB-MONOLAYER NI DEPOSITION ON SI(111)

(This chapter was previously published as J.-Y. Cheng, B. L. Fisher, N. P. Guisinger, and C. M. Lilley, "Atomically manufactured nickel–silicon quantum dots displaying robust resonant tunneling and negative differential resistance," *npj Quantum Materials*, vol. 2, p. 25, 2017/05/22 2017. Linked here.)

6.1 Introduction

There has been significant progress towards the utilization of an electron's spin for the development of quantum bits (qubits) poised to revolutionize modern computers, where the orientation of the spin serves as the basis for "0" and "1" logic operations A major challenge is scaling this technology towards meaningful quantum computation requiring the entanglement of multiple qubits with coherence times long enough for calculations to occur and simultaneously be measured [156-165]. Not surprisingly, materials are at the heart of this challenge, from the fabrication of the qubits to how the electron or nuclear spin interacts with the host material [32, 166-169]. One of the most advantageous platforms has been developing solid-state qubit architectures using traditional semiconductors, where an entire industrial infrastructure exists and hybridization with conventional technology would be greatly beneficial. A predominant approach has been developing qubit systems with quantum dots using III-V semiconductor heterostructures, [31, 33, 170-172] where the lowered dimensionality is utilized for quantum confinement. Significant advances have been made towards addressing the spin in these quantum dot structures that include fast optical control and all-electrical measurements. However, the qubit interaction with the nuclear spins, inherent in the III-V materials, reduces the coherence time and presents a significant challenge. Alternatively, group IV semiconductors are

quite attractive for qubit design because they can provide a spin-free environment, where electron spin coherence times have been measured on the order of seconds [30, 173, 174].

6.2 Ni Surface Reconstruction atop Si(111)

The utilization of Si, a zero nuclear spin material, has been the focus of several proposals as an optimal material for qubit design. Kane *et al.* first described using the nuclear spins of phosphorous dopants arranged as an array within a silicon lattice for the development of a quantum computer [175]. Several experimental efforts are underway to fully develop qubit and quantum technologies based on phosphorous dopants [176-178]. A key to these efforts has been the utilization of STM to both fabricate and characterize the unique placement of single phosphorous donors on both Si and Ge surfaces. Most impressive has been the placement of isolated phosphorous dopants within electronic contacts that can be macroscopically addressed [179, 180]. Although it is not practical to utilize the STM for large-scale qubit fabrication, it has proven to be a powerful tool for the development of proof-of-principle devices and local characterization of quantum structures and phenomena at the atomic-scale.

Rather than fabricate individual quantum structures with the STM, we are interested in exploring large-scale atomic manufacturing of alternative quantum dot structures that self-assemble, consist of only a handful of atoms, and are integrated with a semiconductor substrate. The goal is to find a suitable “bottom-up” approach that is scalable for qubit design. Complimentary to STM fabrication of individual quantum structures between electrical contacts, scalability is envisioned by controlling the density of self-assembled quantum dots over an entire surface. This would allow for the patterning of contacts anywhere on the surface and with optimization result in the desired density of QDs (from one to many) to exist between the contacts. There has been significant research in the area of metal functionalization of silicon

surfaces in the context of thin film growth, metal silicides, and the modification of surface reconstructions [53, 181-183]. Guided by these efforts, this work investigated the submonolayer deposition of Ni on Si(111). At these low coverages, the surface reconstruction is modified and two distinct Ni-Si clusters emerge that consist of either a "1×1" or "√19" quantum dot structure consisting of an ordered grouping of Ni and Si atoms. Here, report the investigation of quantum dot behavior and electron confinement in these Ni-Si atomic clusters. Utilizing STS, resonant tunneling through quantized levels was observed at reproducible energies within the clusters and a larger peak spacing for the smaller clusters, as anticipated for shrinking dimensions. Furthermore, by degenerately doping (n-type) the host substrate, NDR was observed at negative sample bias. Finally, at higher surface coverage the larger clusters form a uniform metal-silicon reconstruction across the surface with a complex electronic landscape. This research presents a model system for large-scale distribution of atomic quantum dots for potential qubit design that are tunable between two distinct sizes with reproducible quantized energy levels and can be designed to exhibit NDR.

A submonolayer of Ni was evaporated onto a Si(111) substrate to observe the initial formation of the atomic Ni-Si clusters, as illustrated in the STM image of Figure 21a. In the topographic STM images, obtained at a sample temperature of 55 K, we observe regions of clean Si(111) where the 7×7 surface reconstruction is unperturbed, thus verifying that we have submonolayer coverage. The majority of the image shows Ni modification to the surface. At low coverage the smaller 7 atom clusters are most prevalent. These clusters topographically appear as small "donut" or "ring" like features in the topographic image as observed in Figure 21b and are highlighted by yellow dashed circles within the zoomed inset. We classify these as "1x1" clusters adopting the nomenclature from the literature where the Ni modification results in

a 1x1 ordering of the underlying Si atoms [184]. The structural model for our 1x1 clusters is schematically drawn in Figure 21b. Looking closely at these STM images there are larger clusters that appear darker within the topographic image. The STM is sensitive to the LDOS and the electronic difference in the larger clusters at this particular sample bias results in the clusters looking slightly depressed into the first layer of Si. These clusters are classified as "√19" clusters and are highlighted by blue circles within the zoomed inset of Figure 1b. Again we have adopted nomenclature from the literature where at higher surface coverage these larger clusters order across the surface and give rise to the reported √19×√19 Ni-Si surface reconstruction . The schematic of Figure 1b showing the spatially larger quantum dot clusters.

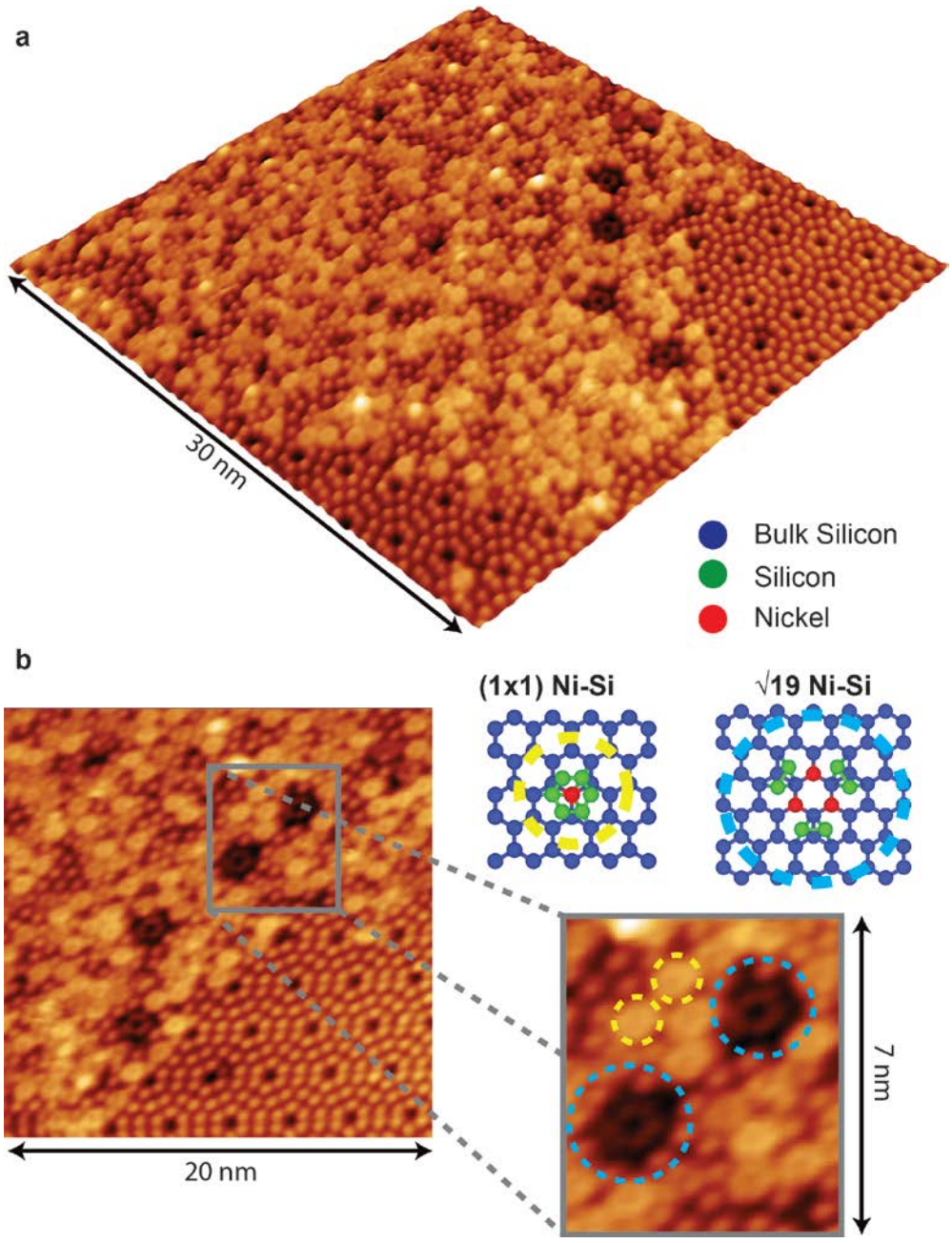

Figure 21 Atomic-scale imaging of Ni-Si clusters. (a) Topographic STM image showing submonolayer Ni coverage, where regions of pristine Si(111)-7×7 surface reconstruction are visible (Sample Bias +2.0V, Setpoint Current 100 pA). Within the Ni restructured area there are predominately "ring-cluster" structures with the underlying reconstruction going 1x1. At the right corner boundary near clean Si(111), there are four unique dark ring structures. (b) Zoom in STM image of the ring-like structures reveals our two cluster formations (1×1 and √19). The ball and stick schematics show the atomic arrangement of the Si atoms relative to the central Ni atoms. The 1×1 clusters (circled in yellow) and the √19 clusters (circled in blue) consist of self-assembled atomic clusters of Si and Ni.

At this point, we can reproducibly fabricate distributions of these atomic Ni-Si clusters on the Si(111) surface, which are consistent with previous surface science studies [53, 181-183]. The true motivation and foundationally unique aspect of this study involves evaluating these atomic Ni-Si clusters as QD structures for potential qubit design. These clusters must possess discrete energy levels resulting from quantum confinement due to the lowered dimensionality and energetically spaced to be technologically accessible. Because these clusters are comprised of only a handful of atoms, it is easy to think of these clusters as small inorganic molecules on the surface. With that analogy, our other concern is whether or not these clusters are electronically unique entities or if they are strongly coupled to the substrate. Thinking of these clusters as QDs with electron confinement we would expect the peak spacing to increase, as the size of the cluster gets smaller, which is schematically illustrated in Figure 22a.

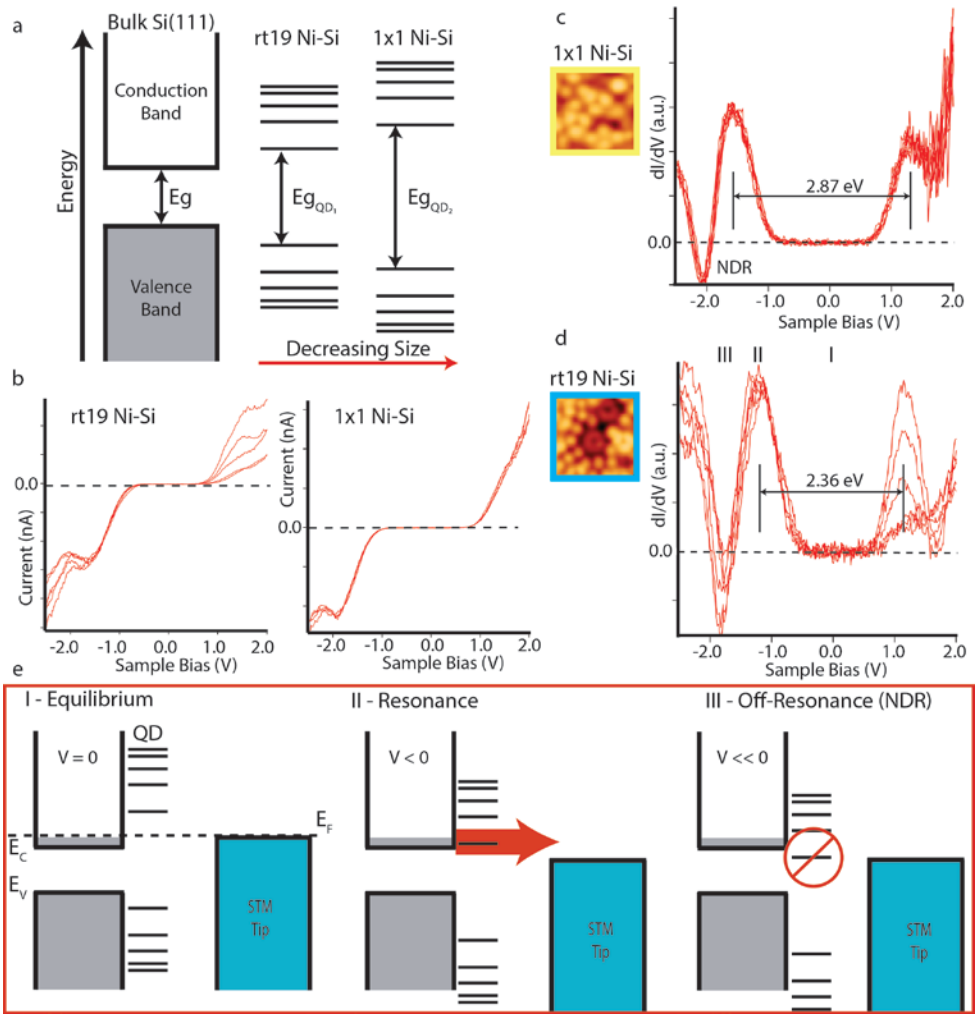

Figure 22 Resonance reveals quantum dot behavior in the atomic clusters. (a) Schematic diagram illustrating that the lowered dimensionality results in electron confinement within the clusters resulting in discrete quantized energy levels. As the size of the quantum dot decreases, the peak spacing should increase and is consistent with what we observe. (b) I-V measurements made over the Ni-Si atomic cluster quantum dots, where the turn-on energies are greater for the smaller 1×1 cluster. NDR is observed in both cluster structures at negative sample bias. (c) Averaged STS dI/dV spectra measured over the 1x1 clusters illustrated in the STM image inset. Clear resonance is observed with discrete energy levels in the cluster at positive and negative bias. Negative conductance is observed and correlated with NDR observed in I-V. (d) Averaged STS spectra of the larger √19 clusters show similar resonance but with a smaller gap between energy levels as illustrated. (e) Schematic band diagrams showing (I) Equilibrium where the Fermi level aligns and is within the conduction band due to degenerate doping of the Si, (II) Resonance where the chemical potential shifts the band of electrons in the conduction band into alignment with discrete energy level, and (III) NDR where the chemical potentials shift until the discrete level falls within the forbidden gap and cannot contribute to tunneling.

To probe the electronic structure of the 1×1 and √19 atomic quantum dots we utilized STS, where the STM probe is positioned over a cluster. With the probe parked, the feedback is turned off and I-V measurements are taken, while simultaneously measuring the dI/dV with lock-in techniques. The dI/dV is proportional to the LDOS. Figure 22b shows averaged I-V measurements taken over the two different clusters. The flat region of zero current between the turn-on at negative and positive sample bias is a reflection of the Si band gap. Qualitatively, we can see that the peak spacing is smaller over the √19 cluster in comparison to the slightly larger peak spacing observed for the smaller 1×1 cluster. Both gaps appear larger than the intrinsic energy gap of the Si(111) substrate, which is 1.1 eV. We also qualitatively observe the consistent onset of NDR at negative sample bias, which will be discussed in greater detail.

Figure 2c shows the dI/dV spectrum taken over the 1x1 clusters, illustrated in the topographic STM inset. There is a tunneling resonance with a quantized energy level at positive bias that represents tunneling through the highest occupied energy level. An almost symmetric resonance is observed at negative sample bias, where the electrons are tunneling through the lowest unoccupied quantized level. The almost symmetric position of the energy level around the Fermi energy (zero sample bias) is consistent with reported STM measurements in different quantum dot systems [38, 185]. The symmetry may be coincidental because it is dictated by how the quantized levels within the quantum dot align at equilibrium, which can be influenced by interaction with the substrate. The fact that resonance is observed at all through these levels suggests that the electronic structure of these clusters is to some extent decoupled from the host substrate. The negative bias resonance peak is clearly depicted because it immediately drops to the observed NDR negative conductance. It is resonance through this energy level that gives rise to the NDR and will be discussed further. The dI/dV spectrum verifies that we are observing

resonant tunneling through discrete energy levels and our clusters are behaving as atomic quantum dots. Measuring the distance between the two resonant peaks allows for a quantitative analysis of the energy level spacing plus twice the charging energy (E_c) of the the quantum dot structures [38, 185]. The 1×1 quantum dots have a consistent peak spacing of approximately 2.87 eV.

The √19 structures display a similar resonance within the dI/dV spectrum, with a peak more clearly observed at positive bias illustrated in Figure 22d. The positive bias peak does not drop to a negative value, which is expected. However, as with the 1x1 clusters, the √19 structures also display a drop to negative conductance after resonance with the negative bias peak. The quantum dot peak spacing is 2.36 eV when measured between the resonant peaks and is smaller for the larger cluster as expected. At negative sample bias NDR is occurring as we sweep from a state of "on-resonance" to "off-resonance" with our atomic quantum dot clusters and the degenerately doped substrate. We intentionally utilized degenerately doped n-type Si(111) to help probe these structures. The degenerate doping results in the Fermi level lying just within the conduction band, as illustrated in Figure 22e. At equilibrium, the Fermi level is aligned between the tip and substrate and should be mid-gap of the quantum dot we are probing. As we sweep the sample bias to negative values, the energy levels shift to a point in which the narrow band of electrons in the conduction band align with the lowest unoccupied level of the quantum dot structure resulting in "on-resonance". As we sweep to larger negative values the energy shift "off-resonance", the NDR only happens in this direction because the level of the quantum dot ends up in the forbidden gap of the semiconductor and can no longer participate in tunneling. At positive bias, "on-resonance" occurs and, although there is a decrease in the dI/dV signal, the

energy level can still participate in tunneling. These results are analogous to NDR observed in resonant tunneling of molecular orbitals on degenerately doped silicon [186, 187].

To further confirm our interpretation of the observed NDR behavior resulting from resonance through a discrete level of our quantum dot clusters, we explored the behavior as a function of tip spacing. The further the tip is away from the quantum dot should result in a shift in the resonant energy and observed NDR. The shifting of the relative position of the energy levels is related to the potential drop within the gap, which is modified when moving the position of the STM tip. Figure 24a shows a topographic STM image of a √19 cluster that was probed as a function of tip position. The colored dots represent the tip position to the corresponding dI/dV spectra plotted in Figure 24b. When the tip is positioned directly over the cluster we observe clear resonance through the discrete energy levels and the onset of NDR. As the tip is moved off of the cluster, the resonance shifts to higher negative values and the NDR is lost. In fact, it is transitioning to resonance through a nearby 1x1 cluster. These results help to strengthen our interpretation of the NDR phenomena.

These “off-resonance” peaks coincide with NDR events in the negative bias. A high dosage of Ni results in the prevalence of the √19x√19 reconstruction over the surface as seen in Figure 24a. The I-V and dI/dV spectra taken atop an individual √19 cluster is shown by the points in Figure 23a is shown in Figure 23b respectively. The on-off voltages for the high Ni dosage √19×√19 NDR event occurs between -1.51±0.01 V and -1.94±0.02 V. These on-off voltages are similar to the on-off voltages of the low Ni dosage. One noticeable difference between the high and low Ni dosage measurements is the Peak Voltage Ratio (PVR) which is defined by the ratio of peak voltage of the NDR event (V_p) and the minimum voltage value of the NDR event (V_m). PVR is used to quantify the performance of comparable NDR electronics and

higher values are better [188]. The PVR is 0.69±0.03 for higher Ni dosages. This PVR is higher than that of the low Ni dosage, but is lower than the NDR events observed in other quantum structures on Si substrates [188-191]. The on-off voltages of Vp and Vm are relatively similar for each measurement, however there is almost no change to the PVR as the lateral tip to sample distance is changed when the tip is moved away from the ring feature. Additionally, there is almost no change in the on-off bias voltage and the PVR remains on the same order between high and low Ni dosages. Due to the low dependence of lateral tip to sample distance and Ni dosage on both on-off voltage and PVR local orbital symmetry matching as the NDR mechanism on Ni-silicide layers may be ruled out [190].

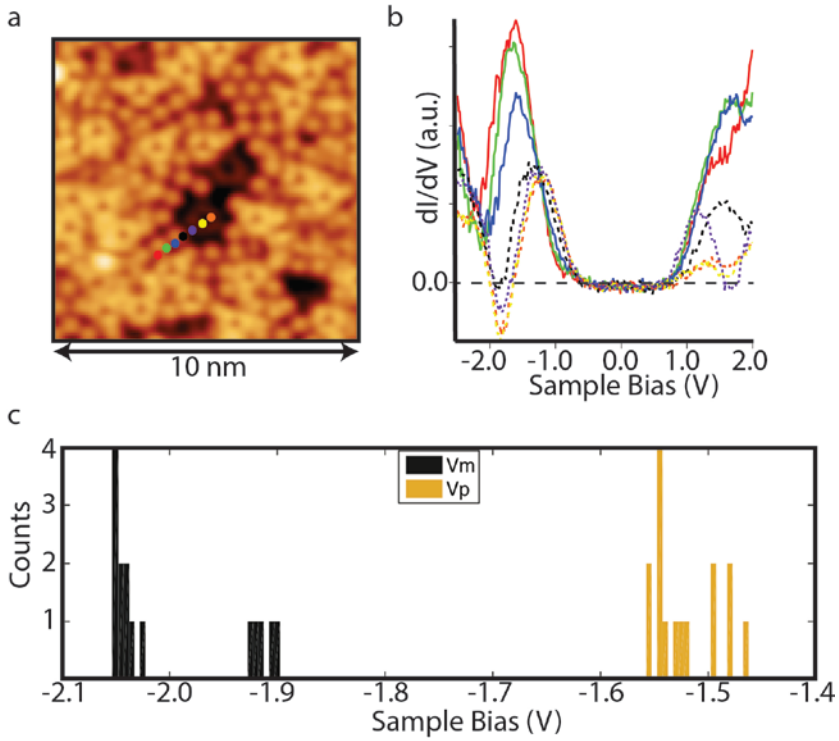

Figure 23 Spatial tip dependence on resonance through quantum dots. (a) STM image showing a line of spectra measured over a √19 cluster. (b) As the position of the STM tip moves, it shifts out of resonance and the negative conductance is lost illustrating a dependence on tip-cluster spacing. (c) The resonant energy for the clusters is extremely reproducible. This histogram shows some statistical analysis of resonant peak energies and minima for the √19 cluster. Although we could benefit from more statistical data to reveal the exact distribution, the peak values lie within 100 meV and there is thermal broadening due to a room temperature tip.

One of the most encouraging results, when considering the potential application of these atomic quantum dots for qubit design, is the consistency of the energy level alignment with the substrate. For numerous 1×1 and √19 clusters, we observe the resonance phenomena at the same energy values, mentioned as the V_p and V_m values. Figure 23c illustrates statistical distributions analyzed for several measurements made on √19 quantum dots. Although a larger statistical ensemble would be preferred, this data shows a clear trend for uniform resonant peak and valley energy positions within our STS spectra. Ultimately, we are illustrating that these clusters can be viewed as atomic-scale quantum dots, but the clusters are randomly distributed on the surface.

There are clear advantages of the self-assembly aspect in the formation of these clusters. Further work must be done to see if this route can be applied to the vision of Kane's quantum computer or provide advantages or complement current experimental efforts with phosphorous atoms.

When the Ni coverage is increased on the surface, the √19 clusters become prevalent across the surface until a saturated √19 Ni surface reconstruction is reached, as illustrated in the topographic image of Figure 4a. This Ni modified surface is stable, robust, and is essentially a tightly packed array of the individual √19 clusters (that were isolated at lower coverage). As the clusters become tightly packed, the electronic structure of the surface is modified and the well-defined resonance observed for the isolated and loosely spaced clusters becomes lost in the STS measurements. The rich electronic structure can be spatially imaged with STS conductance maps that are taken concurrently with the topographic data, as illustrated in Figure 24. The top image, Figure 24b, is the topography and the bottom image, Figure 24c, is the spatial dI/dV conductance map that is proportional to the LDOS for the given imaging sample bias. We also observe very distinct patches of variation within the electronic structure that is visualized by the color scale for high to low values of LDOS.

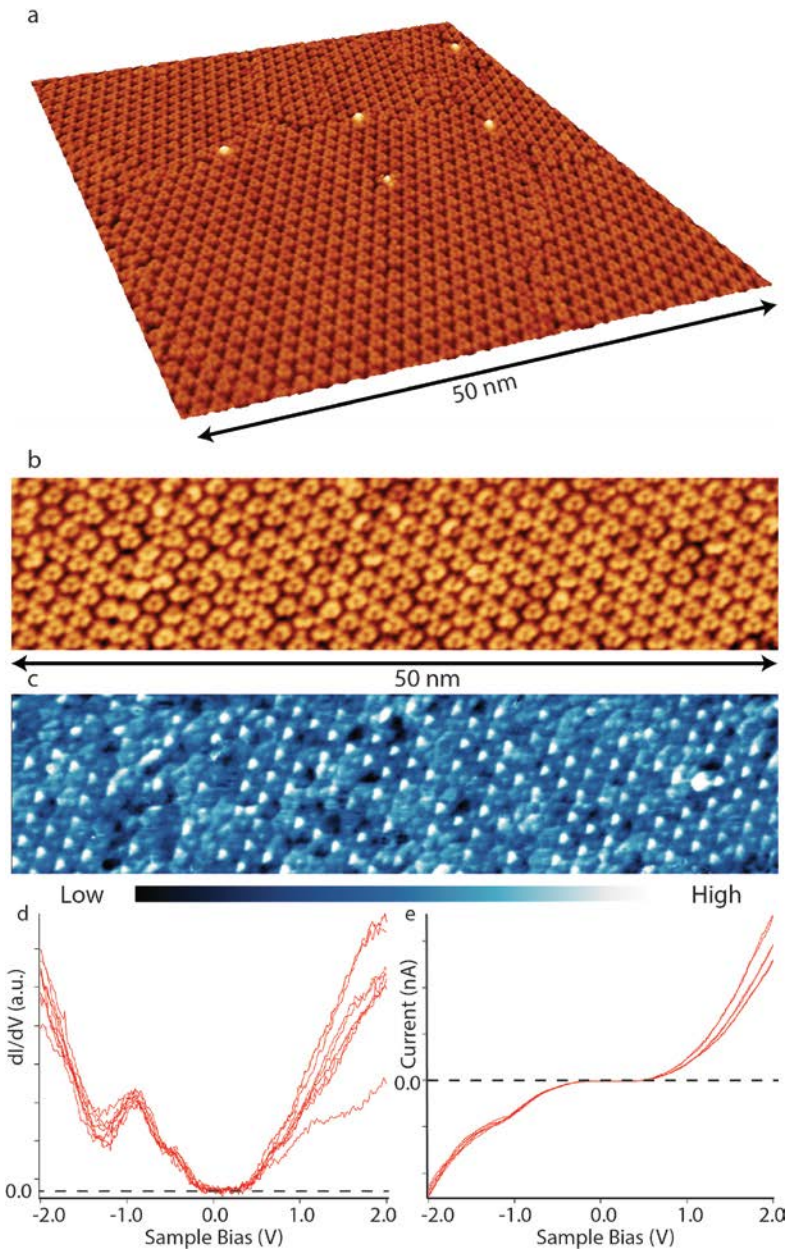

Figure 24 Saturated surface coverage of √19 cluster self-assembly. (a) STM image showing domains of saturated Ni-Si √19 cluster formation, where they hexagonally arrange with domain boundaries visible within the image (Sample Bias -2 V, Setpoint Current 200 pA). (b) A zoomed in STM image shows a uniform array of √19 clusters with some defects and vacancies. (c) A spatial dI/dV map for the same area in (b) showing a rich electronic ordering within the tightly packed atomic quantum dot array (Sample Bias -2 V, Setpoint Current 200 pA). (d) STS dI/dV spectra measured at different points over the tightly packed √19 clusters. The peak at negative bias has broadened and we do not observe the presence of NDR. (e) I-V measurements also confirm the loss of NDR and only a slight shoulder is observed. As the clusters pack together tightly, we believe that the levels of the QD structures overlap and broaden the measured spectra.

The array of bright circular features corresponds to a network of linking atoms between the clusters. By careful inspection of Figure 24c, the clusters themselves have a uniform circular LDOS with a slight brighter region directly at the center. However, there are several patches of brighter contrast and some clusters that appear dark, while some of the bright circular regions of linking atoms are missing. We feel that the LDOS variation is in part due to missing atoms in the full √19 reconstruction, defects, and some adsorbates. The intriguing aspect is how uniform the LDOS are for patches of different clusters. A key component to qubit design is achieving entanglement between qubits so information can be transferred. To further explore this possibility, we performed STS measurements of the full √19 reconstruction that are plotted in Figure 24(d, e). The STS measurements no longer display a sharp resonant peak and NDR is not observed at any position on this surface. Instead, a broadened peak is observed at negative bias and no peak is observed at positive bias. The I-V curve in Figure 24e shows a slight shoulder at negative bias but no NDR. We believe that the loss of resonance in our STS measurements is due to broadening of the levels as the clusters move closer together, which indicates that levels are overlapping and interacting. These aspects are to be explored in further studies that can be performed with instrumentation at lower temperature to increase the energy resolution and spatial stability of the spectroscopy.

6.3 Concluding Remarks

In conclusion, STM and STS were utilized to investigate atomic-scale Ni-Si clusters on the Si(111) surface. The dI/dV measurements revealed resonant tunneling through discrete energy levels within the clusters. Resonance through these levels suggests that the electronic structure of these clusters is only weakly coupled to the Si(111) substrate. The clusters behave as quantum dots on the Si surface and consist of either ("1×1") or ("√19") atomic clusters. We

intentionally explored Ni surface modification and cluster formation on degenerately doped n-type Si(111), where the Fermi level lies within the conduction band. The resonance with our highest unoccupied state with the atomic Ni-Si quantum dots resulted in NDR observed at negative sample bias in both I-V measurements and dI/dV spectra. The peak spacing of the clusters increases as the size of the quantum dot decreases. Further experiments should be run on more sophisticated low temperature instruments to increase the energy resolution. Overall, the self-assembly of Ni-Si clusters on the surface is a promising and intriguing platform for the development qubit and quantum technologies utilizing atomic-scale quantum dots self-assembled on a Si substrate.

CHAPTER 7 SN SURFACE RECONSTRUCTION ATOP SI(111)

7.1 Introduction

Early research of Sn on semiconductors was motivated by studying superconductive properties of Sn [56, 57]. More recently, there has been renewed interest in research on low dimensional Sn, e.g. as a 2-dimensional atomic layer, due to its predicted behavior as a topological insulator [192]. Researchers have studied Sn/Ge(111) and Pb/Si(111) monolayer systems and have found that they display charge ordering at lower temperatures [55, 57]. Charge ordering occurs as a material transitions to a superconducting state near its Curie temperature. Yet, there is an existing knowledge gap on the properties of Sn on Si(111). Previous research of Sn/Si(111) focused on $\sqrt{3}\times\sqrt{3}$ and $2\sqrt{3}\times2\sqrt{3}$ surface reconstructions, which readily form on the Si(111) surface, and will be referred to as $\sqrt{3}$ and $2\sqrt{3}$ respectively. Researchers found that the Sn $\sqrt{3}$ phase undergoes a metal-insulator transition at low temperature (<60K) [193-195]. However, several unanswered questions remain regarding the properties of the $2\sqrt{3}$ phase. For example, there is an existing disagreement regarding the number of atoms in the unit cell of the Sn $2\sqrt{3}$ phase [63, 196-199], although there are two commonly proposed models. In addition, the electrical properties of low dimensional Sn $2\sqrt{3}$ at low temperatures have not been fully characterized.

7.2 Electronic Characterization of Sn Surface Reconstructions

A new phase reconstruction of $4\sqrt{3}\times2\sqrt{3}$ was found to coexist with the $2\sqrt{3}$ phase at low temperature (LT), referred to henceforth as $4\sqrt{3}$. This new phase has been observed by Fangfei Ming et al. [200]. The unique structure and electronic characteristics of the $4\sqrt{3}$ phase point towards charge ordering in Sn monolayers. Charge ordering has been shown to appear in other low dimensional layers [57, 64, 66]. It can precede the appearance of CDW in superconductors

and low dimensional topological insulators indicating a low temperature superconducting transition. Charge ordering shows similar characteristics to CDW such as the appearance of checkerboard or striped patterns in STM conductance images at low temperature that differ from room temperature observations. However, charge ordering differs from CDW in that the low temperature conductance image patterns may not display long-range periodicity. STM and STS studies were performed for the √3, 2√3, and 4√3 phases of Sn/Si(111) at room temperature (295K) and LT (55K). The 2√3 to 4√3 Sn/Si(111) reconstruction was found to exhibit charge ordering due to the checkerboard-like pattern in the conductance imaging of the new 4√3 phase reconstruction at LT.

After monolayer deposition of Sn on Si(111), two surface reconstruction phases may be seen in STM images at room temperature. In Figure 1(a) the STM topography (orange shading) and conductance images (purple shading) show a 2√3 phase surrounded by the √3 phase. Zoomed in image of an isolated 2√3 phase can be seen in STM topography and conductance images in Figure 1(b). The green and yellow areas represent zoomed in views shown in Figure 1(c) alongside line profiles and FFT images. From the line profiles it is apparent that the 2√3 phase does indeed have two layers.

The structure and number of atoms of the Sn/Si(111) 2√3 unit cell is still under dispute. The widely accepted 2√3 model consisting of 13 atoms was relaxed using the VASP© DFT software. This model was recreated based upon the models by Ichikawa and Cho [198] which were modeled after the 2√3 structure proposed by Törnevik et al. [48]. The initial bilayer can be seen in the top and side view of supplementary Figure 25a where the four top layer Sn atoms are colored red and green. After DFT relaxation the bilayer flattens out into a single Sn layer shown in Figure 25b. Instead of the bilayer structure of the 2√3 seen in experiments, the relaxed

simulation shows only a single Sn layer. Previous papers have mentioned that the 2√3 model is unstable and result in differing views on how many atoms truly exist in the Sn 2√3 unit cell [201]. However, comparing the approximate atomic distances of the dimer pairs to each other the accepted 13 atom model does not have the same atomic spacing as seen in the experimental images. Based upon the FFT images the average lattice spacing of the √3 phase was measured at 1.18 ± 0.43 nm and the 2√3 phase was measured at 1.61 ± 0.20 nm. More work needs to be performed in order to generate an accurate atomic model of the unit cell.

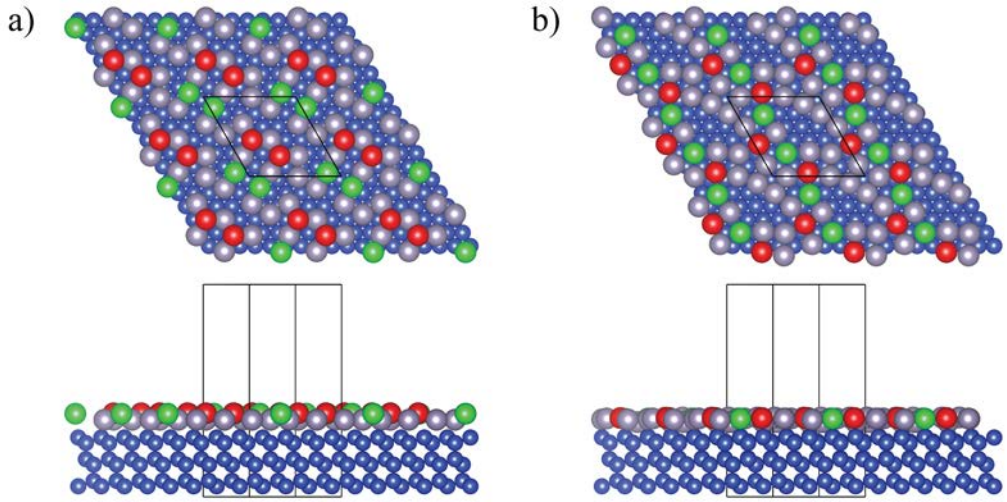

Figure 25 Top and side view of the 13 atom model proposed by Toernvik et al. (a) before DFT relaxation and (b) after DFT relaxation. Blue Atoms represent Si, whilst grey, red, and green atoms represent the 2√3x2√3 Sn layer. Red and Green atoms in (a) represent the higher height dimers in the unrelaxed model. Their positions after relaxation are shown in (b).

At low temperature (~55K) a new phase was observed in the 2√3phase. This new 4√3 phase can be seen in Figure 26b. This 4√3 phase is seen alongside the 2√3 phase at low temperature in Figure 26b and is outlined by white dashed lines to act as a guideline for the eye. The 4√3 phase appears as stripes within the 2√3 phase areas and can be seen more clearly in zoomed topography and conductance images in Figure 27b. The 4√3 phase is different than the

2√3 phase in that the top most dimer pair of the Sn bilayer structure follows alternating directions similar to a herringbone pattern. The striped areas of the 4√3 phase are even more distinct in STM conductance images. It was observed that the 2√3 to 4√3 transition is reversible upon allowing the sample to warm back up to room temperature.

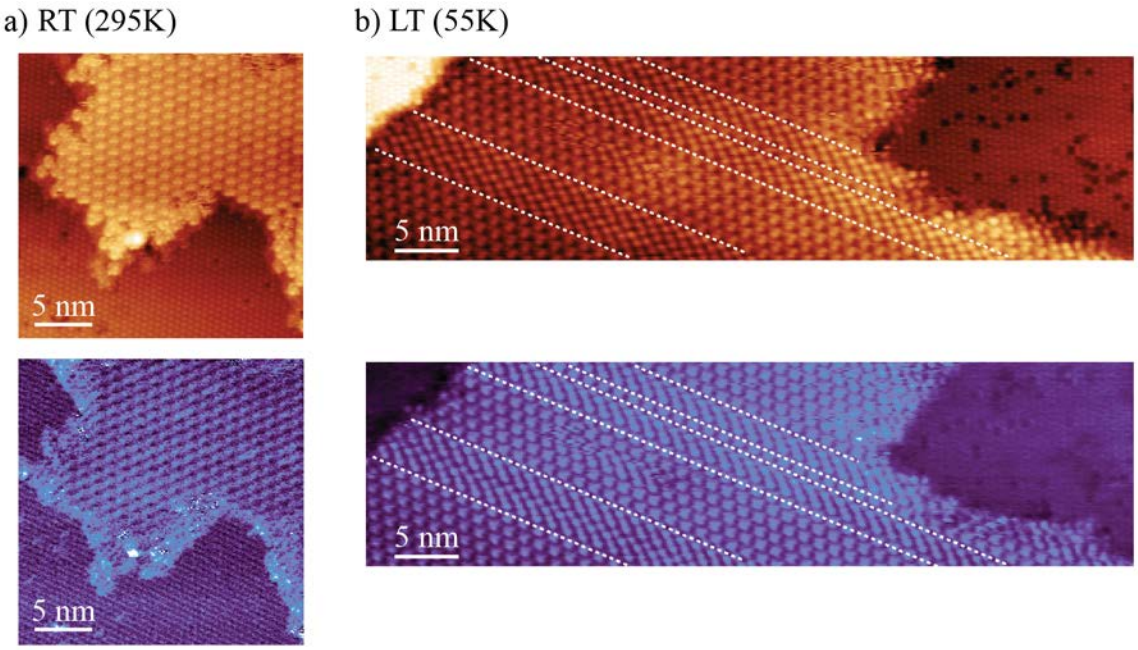

Figure 26 (a) Room temperature (295K) STM topography (orange color scale) and conductance image (purple color scale) of a 2√3 island surrounded by √3 reconstruction. (I=100pA, V_b=-1V) (b) Topography and conductance image of the 4√3 reconstruction alongside the 2√3 and √3 reconstructions at LT. White dashed lines are guidelines for the eye highlighting the 4√3 areas. (I=250pA, V_b=1V)

The room temperature phase of 2√3 has topological and conductance image FFT patterns that resemble each other closely in both size pattern and spacing of 2.7, 3.1, and 2.3 nm^{-1} shown in the Figure 27h. Although the FFT peaks match in spacing, the checkboard conductance image FFT is missing many of the other features present in the conductance image FFT pattern. The discrepancy between the two patterns indicates a change in the charge density around the atomic

structure further supporting the evidence of charge ordering. Conductance images of the 4√3 phase in Figure 27b and Figure 27d show a checkerboard like pattern indicating that the phase is atomically, and electronically different than the room temperature 2√3 phase.

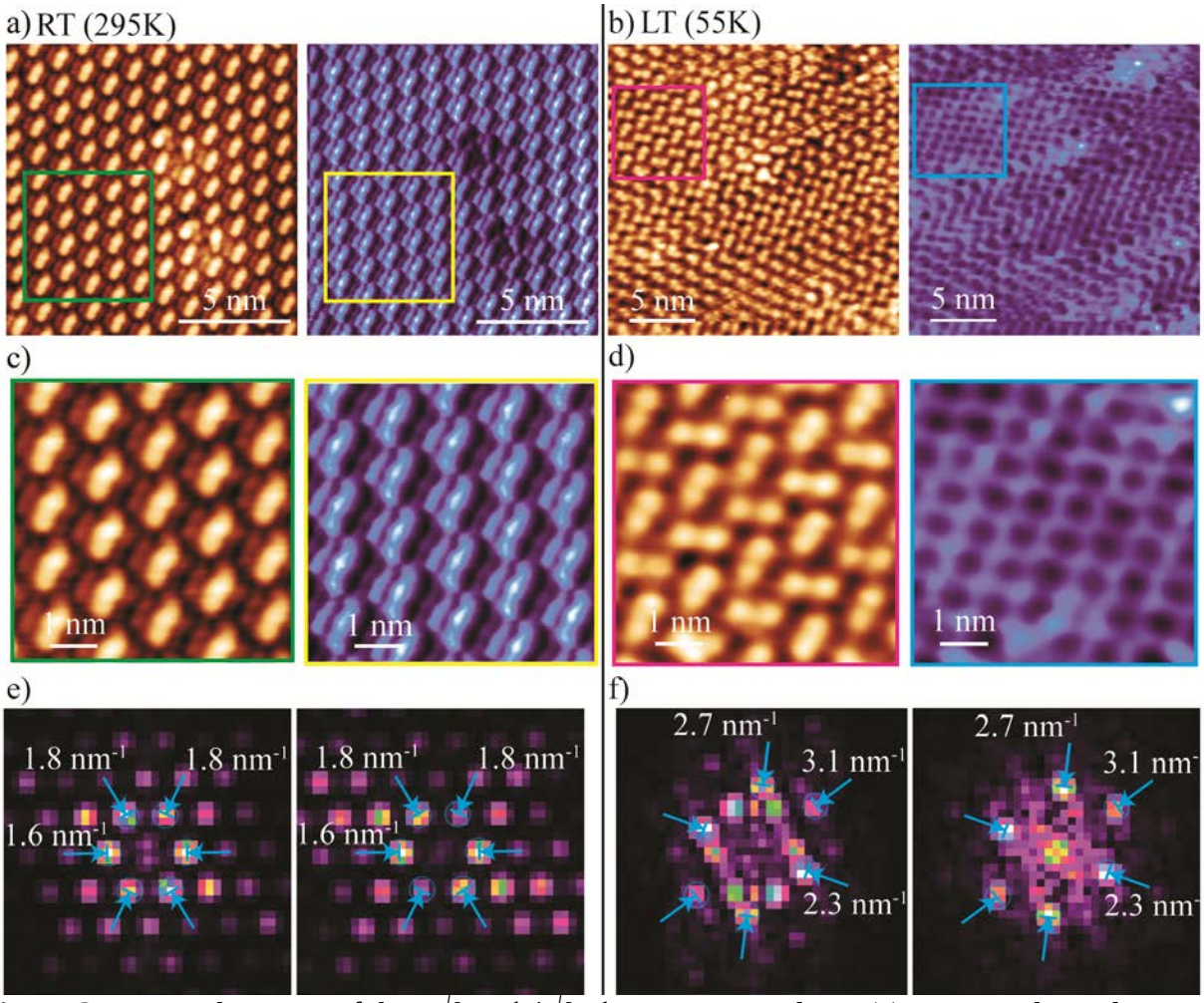

Figure 27 Zoomed in view of the 2√3 and 4√3 phases at RT and LT. (a) Topography and conductance image of RT 2√3 reconstruction. (I=600pA, V_b=0.5V). (b) Topography and conductance image of 4√3 reconstruction alongside areas of 2√3. (I=1nA, V_b=1V) (c) Zoomed areas of the RT 2√3 phase from (a). (d) Zoomed areas of the LT 4√3 phase from (b). (e) FFT patterns of the topography and conductance image from (c) showing the spacings of the RT 2√3, which roughly correlate to the lattice parameters of the 2√3 unit cell. (f) FFT patterns of the topography and conductance images from (d) showing the spacings of the LT 4√3.

The transition of the 2√3 phase to the 4√3 is proposed in Figure 28a. The 2√3 phase at RT is believed to have two dimer pairs in the top Sn layer which rest at two slightly different heights as noted by their contrast difference in STM topography images. In Figure 28a the higher height atoms are denoted by solid black circles, whereas the lower height atoms still in the top layer are denote by the white circles. In the 4√3 at phase at LT the parallel dimer pairs are no longer present and instead alternating angled dimer pairs are seen. This forms a herringbone-like pattern with the angled dimer pairs at LT. The angled dimers may form to rocking/rotation of the parallel dimer pairs about their center allowing the cross bonding to form resulting in the angled dimers seen in the 4√3 phase. The periodicity and proposed formation of the 4√3 phase is similar to that proposed by Fangfei Ming et al. [200]. This may be supported by the slight height variation and atomic distances of the angled dimers seen in the line profiles plotted in Figure 28b. It was also observed that the angled dimers are always present in pairs and occupies roughly twice the space as the room temperature 2√3 unit cell, which justify the 4√3×2√3 nomenclature used as noted by Weisong Tu et al. [201] and Fanfei Ming et al. [200]. The number of paired angled dimer columns as well as measured width of the 4√3 and spacing between 4√3 stripes may be seen in the supplementary histograms in Figure 29. However, only so much structural information of the 4√3 phase can be assumed through STM imaging. Future work will need to include low temperature LEED, XRD, and XPS in order to determine the actual atomic structure of the new phase.

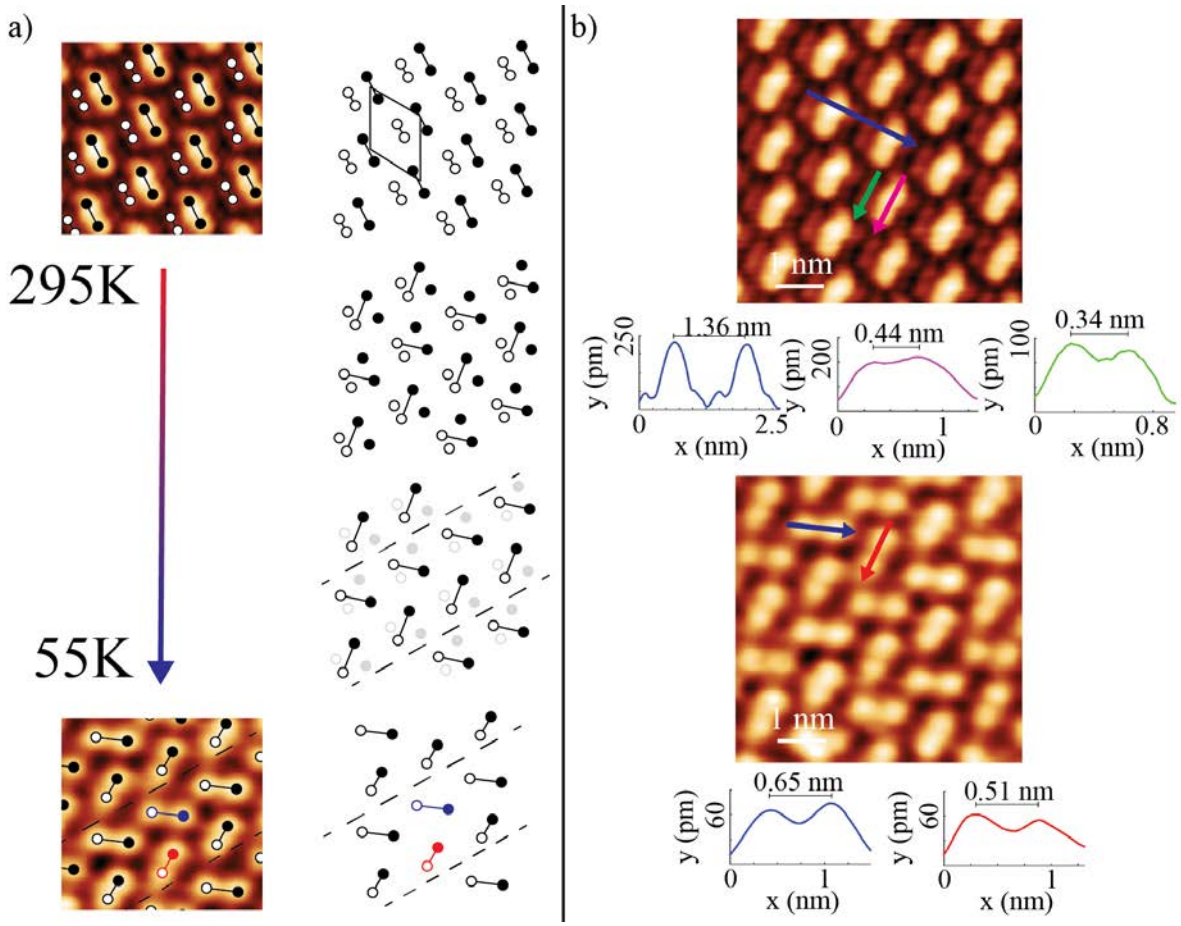

Figure 28 (a) Possible example of the dimer pair transition of Sn atoms from RT to LT. The rhombus represents a proposed unit cell of the 2√3consisting of 13 atoms at room temperature. Filled circles represent the atom in the pair with the higher height value. Dashed lines are guidelines to separate the paired 4√3dimers. (b) Line profiles over the 2√3 and 4√3 phases.

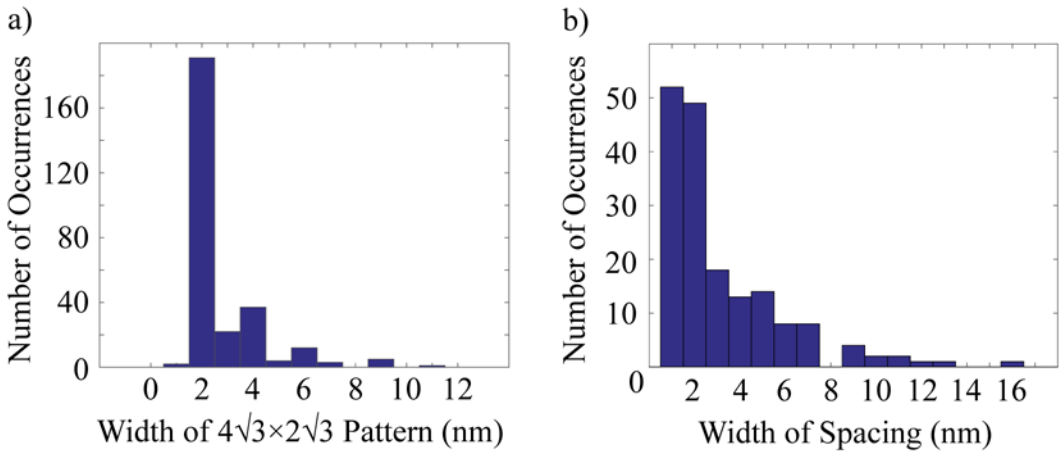

Figure 29 (a) Histogram of the average width of the 4√3 pattern and (b) the average spacing between each stripe or areas of 4√3.

A series of STS point spectra were taken over the different phases at RT(295K) and at LT (55K) to analyze the electronic change of the phases. Figure 30a and Figure 30b show magnified STM topography images of the √3 phase at RT and LT respectively as well as averaged STS dI/dV and I-V spectra around colored points indicated on the images. Similarly, Figure 30c and Figure 30d show the same information for the 2√3 phase at RT and concurrent 2√3 and 4√3 phase at LT respectively. The measured band gap of the √3 phase at RT was approximately 0.02±0.01 eV, whereas at LT the measured band gap was approximately 0.74±0.04 eV. These values do not match values found by other researchers shown in Table 2. One noticeable difference between this work and previous experiments is that the much of the dI/dV data and subsequent band gap calculations were derived from I-V data and not true dI/dV measurements.

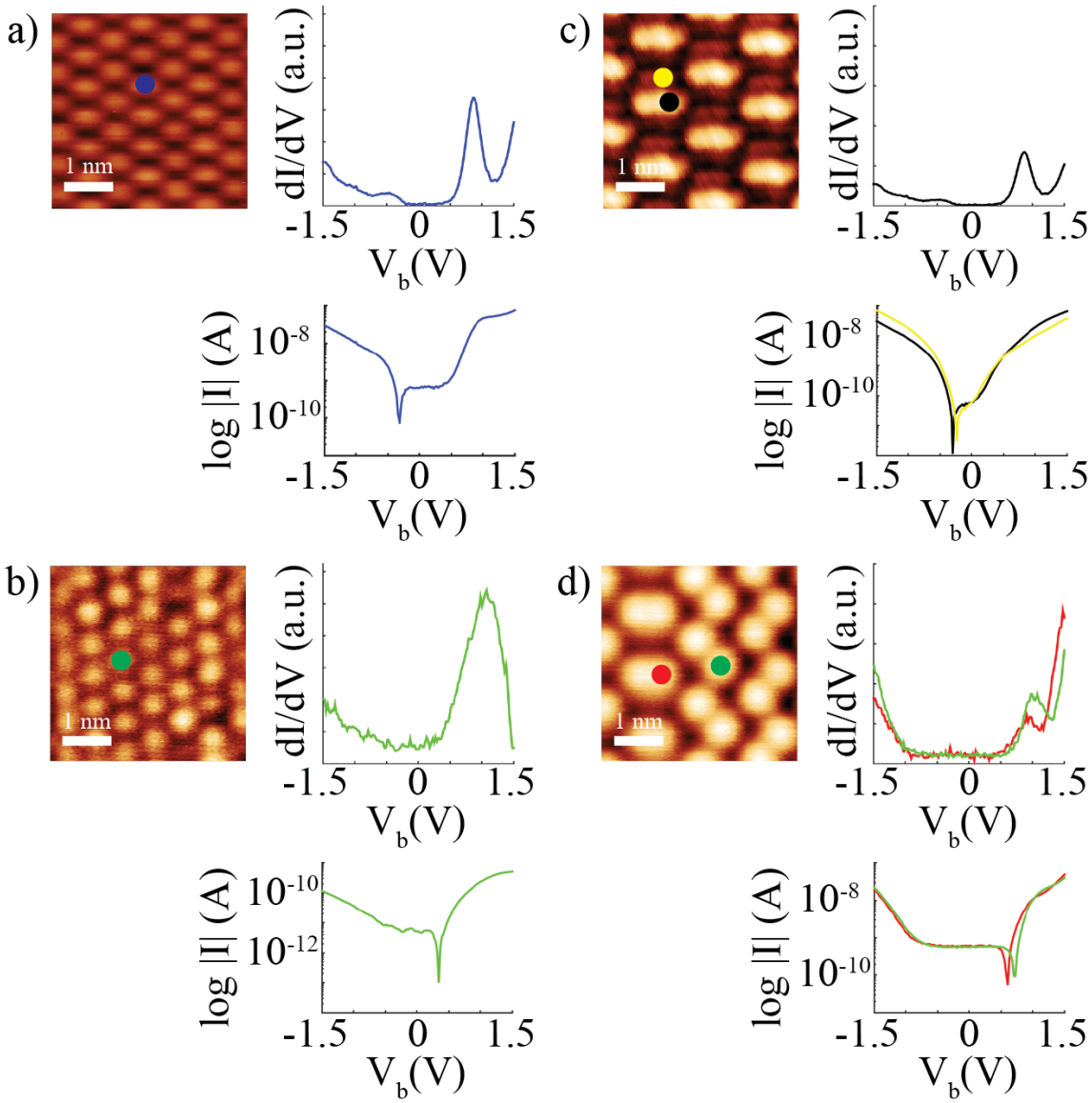

Figure 30 STM topography image, dI/dV point spectroscopy plot, and logarithmic scale I-V point spectroscopy plot of (a) room temperature √3 phase (I=300 pA, V_b=-1.5 V) (b) low temperature √3 phase (I=500 pA, V_b=1 V) (c) room temperature 2√3 phase (I=600 pA, V_b=0.5 V) (d) low temperature 2√3 and 4√3 phases (I=100 pA, V_b=1 V).

Table 2 Band gaps of the Sn √3 and 2√3 reconstructions on Si(111)

Structure	Band Gap (RT)	Band Gap (LT 55K)	Band gap Literature
√3×√3	0.02 eV	0.37 eV	0.4-0.5 RT [59, 193], 0.2 eV LT (5K) [44]
2√3×2√3	0.74 eV	1.03 eV	0.8 eV RT [63]
4√3×4√3	---	1.03 eV	---

At RT the measured band gap for the 2√3 was approximately 0.37±0.04 eV. At LT the measured band gap of the unreconstructed 2√3 areas was 1.03±0.2 eV. Over the 4√3 phase the band gap was measured to be nearly identical. There is no current work to compare the LT 4√3 phase band gap to and no mention of the 4√3 outside of the work by W. Tu [201]. Decreasing the sample temperature to 55K resulted in an increase of the band gaps of the √3 phase and 2√3 phase.

Based upon STM and STS observations, it is thought that the LT phase change of 2√3 to 4√3 is due to charge ordering. Other papers have suggested that the Sn √3 phase reconstruction under LT (5K and 60K) also undergoes charge ordering on Ge(111) substrates [64, 66]. The conductance images for the 4√3 phase seen in this work has the same characteristics as charge ordering seen over Sn/Ge(111) and Sn/Si(111). The periodicity of the 4√3 phase in the STS images indicates charge ordering due to the low periodicity and long range order of the conductance image patterns. Checkerboard-like patterns of the dI/dV conductance images of the 4√3 phase are similar to observed charge ordering in metal-semiconductor interfaces. In Figure 27d, the checkerboard pattern of the 4√3 phase in the conductance image can be seen alongside the more parallel pattern of the 2√3 phase even at LT. The conductance images of the 2√3 phase are nearly identical analyzed at RT or LT. FFT of the 4√3 checkerboard-like conductance image show a rhombus shaped pattern and can be seen in Figure 28a. Although the images have been processed to minimize or eliminate any image curvature and drift, the possibility remains that

some remain and affect the FFT, manifesting in the pattern as a rhombus instead of a possible diamond or rectangular shape. Regardless, the overall pattern of the conductance image is still similar to checkerboard-like images from two-dimensional materials that have displayed charge ordering [202, 203] and very similar to conductance imaging of the Pb/Ge(111) interface [65], and Sn/Ge(111) √3 phases [64, 66]. One may believe, that due to the similarity of these systems consisting entirely of group IV elements, charge ordering may also be present in the Sn/Si(111) system. No papers, thus far, have looked at charge ordering atop the Sn/Si(111) 4√3 reconstruction. It is believed that this is a reconstruction of the 2√3 phase at LT. This physical reconstruction is thought to be the cause of the charge ordering in the 4√3 phase. Both 2√3 and 4√3 phases coexist at LT as seen in multiple images. However, between these two phases, two distinct conductance image patterns can also be seen. An alternative cause to the appearance of a 4√3 surface may be surface modulation from hole doping [201]. However, modulation hole doping does not address the apparent periodicity of the 4√3 phase nor effects on the conductance imaging. Further studies are needed in order to understand the exact structure of the 4√3 phase to elucidate the nature of the charge ordering.

7.3 Concluding Remarks

As found in our DFT modeling, the currently accepted 13 atom 2√3 phase model is unstable after DFT relaxation. Thus, a new model for the room temperature 2√3 phase is needed. A newly observed LT phase transition of 2√3 to 4√3 was discovered and has been observed to exist simultaneously alongside 2√3 phases. This new reconstruction matches that observed by Fangfei Ming et al. [200]. The broken periodicity and short range order of the 4√3 phase indicates that the transition observed is not due to a CDW. However, this transition may be due to charge ordering since conductance images have shown the 4√3 phase to have a checkerboard

like pattern and charge ordering can indicate CDW at even lower temperatures. Thus, studies in the ~4K range will need to be performed on the 2√3 and 4√3 phases of Sn/Si(111) to see if a CDW may occur in these Sn reconstructions. Experimental temperatures below 55K may also affect the periodicity and long-range order of the 4√3 phase. Additional work using low temperature LEED and XPS will need to be performed to determine the true structure of the new 4√3 phase in future work. If a CDW can be confirmed in Sn it will aid in the understanding of superconducting characteristics of single element monolayers.

CHAPTER 8 CONCLUSIONS AND RECOMMENDATIONS FOR FUTURE WORK

8.1 Conclusions

The research goal was to fabricate low dimensional nanomaterials with tunable electronic properties directly on Si. The first objective was to use DFT simulations to study the properties of 2D films on silicides, where silicides would be epitaxial to a Si substrate. The second objective was to see if graphene could be fabricated on Si using a silicide layer for 2D layer growth. The third objective was to use the self-assembly to directly fabricate metal silicide quantum structures on Si to study their lowest possible dimensional properties. And the fourth objective was to fabricate low dimensional Sn layers on Si using self-assembly methods and to study their electrical behavior.

In this research the following tasks were performed: DFT simulations of silicene on $NiSi_2$ and grapheme on $NiSi_2$ and Cu_3Si. DFT simulations showed that silicene on $NiSi_2$ is strongly coupled and the hydrogenation of the interface or silicene layer is necessary to decouple the 2D layer and silicide. By decoupling the silicene or H:silicene layer, the freestanding properties were mostly retained. The Dirac point of silicene on H:$NiSi_2$ was no longer linear around the K point in the Brillouin zone and was shifted 0.22 eV above the Fermi energy possibly showing a shift to n-type, but parabolic fits used to calculate the electron effective mass and Fermi velocity of v_f = 0.39×10^6 m/s for freestanding silicene on H:$NiSi_2$ which is on the same order of its predicted freestanding values. For graphene, DFT simulations show that a graphene layer is weakly coupled to either $NiSi_2$ or Cu_3Si, most likely through Van der Waals interaction. Since the graphene layer is decoupled it retained linear bands around the K point in the Brillouin zone. Although graphene retained linear bands around the Dirac point, there was a shift in the Dirac point below the Fermi energy of -0.46 eV atop $NiSi_2$, showing a shift to p-type. Graphene atop

$NiSi_2$ retained its freestanding Fermi velocity of v_f =1.5x10^6 m/s. Graphene atop Cu_3Si showed a low binding energy, but no Dirac point in the Band structure around the K point in reciprocal space. The DOS and band structure of graphene on Cu3Si is thought to show that the graphene layer is metallic like the silicide substrate, however this contradicts the low binding energy calculated at the interface. It was expected that graphene would retain its 2D characteristics above Cu_3Si and future research will need to be performed to confirm if alternative pseudopotentials will need to be used in order to accurately simulate the system. These DFT simulations were used to address objective one to study the 2D layer properties atop a silicide surface. Using these simulations one may be able to further understand how silicides may affect the properties of a 2D layer if used to integrate a low dimensional structure, such as graphene or silicene, in nanoelectronics.

Further studies attempted the direct growth of graphene on a Si substrate using a silicide for 2D layer growth. CVD was used to attempt graphene growth on $NiSi_2$ and Cu_3Si, although direct growth of graphene on $NiSi_2$ was unsuccessful. However, graphene was successfully grown directly on Cu_3Si structures using CVD. The formation of self-assembled Cu_3Si structures on Si(111) was verified using XRD, and the presence of graphene was verified using Raman spectroscopy. Raman spectroscopy showed that the graphene layers were successfully grown on the Cu_3Si structures. 1-3 layers of graphene were present over the Cu_3Si structures or varying quality. And like graphene covered Ni, Fe, and Co silicides prevented oxidation of the Cu_3Si layer after exposure to an ambient environment. Objective two was successfully met through this experiment by growing graphene directly on Si(111) substrate using a Cu_3Si layer for graphene growth using CVD. Using this method graphene was directly integrated on a Si substrate without using the transfer method. Although the graphene's electrical properties have yet to be

characterized, it is assumed that the as-grown properties are preserved. Thus, this method allowed one to use silicides to grow the low dimensional material graphene and hopefully preserve its electrical properties atop Si.

Objective three was achieved by studying self-assembled atomic Ni-silicide ring like QD structures were studied using STM. These ring like structures are the result of sub-monolayer Ni reconstructions on Si(111). This ring structures have been observed in Ni surface reconstructions known as the √19×√19 and 1×1 [53, 183, 204]. STS spectra of these structures showed that the both displayed an NDR event in the negative bias voltage. The confinement of the NDR events over both structures to the negative bias voltage is most likely due to the n-type doping of the Si substrate [186]. The individual ring structures of √19×√19 and 1×1 were studied, but at higher Ni coverage, the √19 structure is prominent resulting in large areas of arrayed ring structures on the surface. Due to the self-assembly of these √19 ring structures on the surface large arrays of the Ni-Si QDs may be formed on Si(111). Even at higher coverage these √19 Ni-Si ring structure arrays still display NDR. Utilizing these self-assembled arrays of the Ni silicide QD rings may be a method of fabricating large scale arrays of QDs on Si platforms in the future.

Objective four was to study low dimensional Sn layers self-assembled on a Si substrate. Sn monolayers were deposited on Si(111) and the two known surface reconstructions of √3 and 2√3 were observed. However, upon lowering the sample temperature to 55K the 2√3 phase underwent a transition to a new 4√3 phase. This 4√3 phase has an altered 2√3 structure with short range periodicity and order and takes on a herringbone pattern. This 4√3 phase has a checkerboard like conductance pattern whose FFT pattern does not match that of the topological FFT pattern. The presence of the ordered conductance pattern and mismatching FFT over this low temperature 4√3 phase indicates some charge ordering. Additionally, the 4√3 phase has an

increase in band gap compared to the remaining $2\sqrt{3}$ phase at low temperature. Studying the low temperature $4\sqrt{3}$ phase opens up the debate again whether a CDW, observed in superconducting materials, would be present at Sn at even lower temperatures in the sub 4K range. The presence of charge ordering itself shows that Sn monolayers may display other superconducting characteristics.

The research presented in the thesis has covered the DFT simulations of 2D layers on silicides, the growth of graphene directly on a Si substrate using a Cu_3Si layer, the characterization of self-assembled Ni-Si QD ring structures on Si, and the characterization of low temperature charge ordering in a newly observed Sn $4\sqrt{3}\times2\sqrt{3}$ phase on Si(111). These tasks have addressed the four objectives outlined at the beginning of this work. This research showed that silicide layers themselves may support the direct growth and integration of a low dimensional structures, such as graphene, on Si substrates. The self-assembly of low dimensional Ni-Si QD structures and Sn 2D layers on Si(111) have further shown that at the these low dimensions materials have unique electronic properties which may be applied to future electronic applications. All of this research supports the goal of fabricating low dimensional nanomaterials with tunable electronic properties, such as metal-Si and metal silicide 2D layers and QDs, atop Si platforms.

8.2 Future Work

In this thesis, DFT simulations were used to study how the interface of a 2D layer and silicide would affect the electronic properties, such as the band structure. In order to utilize graphene in transistor based technology a band gap needs to be opened. Graphene on silicides seem to remain decoupled and retains its freestanding characteristic of no band gap. Alternative or modified pseudopotentials should be tested to see if they provide a more realistic electron

interaction between carbon and metal silicides. Future DFT studies simulating the intercalation of elements such as Ca, F, H, and O between graphene and a silicide layer may be used to see if a graphene layer's electronic properties can be tuned.

Silicides have been shown to have a high energy density in Li ion energy storage [205, 206]. However, due to the high reactivity of silicides with oxygen and other chemical elements [138, 149, 207, 208], many silicide applications would require an encapsulation layer, such as graphene. Graphene has already proven to be an oxidation barrier for Ni, Co, and Fe silicides [29]. Due to graphene's chemical stability it stands to reason to that a graphene encapsulation may protect a silicide layer from other harsh chemicals in applications such as energy storage. Graphene encapsulation of Si nanoparticles for energy storage has already been demonstrated, where graphene prevented Si oxidation and mechanically restrained lithiation expansion further increasing the maximum number of lithiation cycles [209-211]. Graphene coated silicides may also perform well for Li energy storage. DFT simulations on the lithiation and de-lithiation of graphene capped silicide surfaces may provide future insight into whether such a structure would be a viable anode for Li ion cells.

Much work remains in the characterization of low dimensional metal-Si nanostructures. Although this work concentrated on Cu and Ni silicides, other silicide forming metals may display unique properties. Co, Fe and Ti are three examples of silicides, which present unique properties that have applications in QDs, photovoltaics, and energy storage [25, 206, 212]. Some of these metal silicides form similar ring like structures on Si observed here in Ni-Si. The characterization work of the Ni-Si ring structures in this thesis were carried out at room temperature. Further studies of this structure need to be carried out at lower temperatures to see how these QD structures will behave.

STM analysis of the 2√3 phase at low temperature provided new insight into possible charge ordering in the 4√3 phase on Si(111). This low temperature study was only performed at 55K. Whereas other CDWs observed in the same temperature range are commonly found in complex cuprates [213]. The long range periodicity of the 4√3 phase may increase at temperatures less than 4K, which is the temperature when Sn supposedly becomes superconducting. There is no current work that analyzes whether a full CDW may occur in the 4√3 phase at <4K. Additionally, if a CDW and superconducting characteristics present themselves, a superconducting gap may be measured using STS further confirming that these Sn monolayers on Si may undergo a superconducting transition and exhibit behavior as a topological insulator at LT. This work should also be coupled with DFT simulations to determine a more accurate model for the 2√3 unit cell as well as propose a model for the 4√3 unit cell.

The exploration for a 2D layer of Sn, i.e. stanene, can also be expanded to utilizing other substrates. 2D group IV layers such as silicene, germanene, and graphene are commonly grown on metals such as Ag and Cu [131]. This is usually due to the low solubility of those group IV elements with the metal substrates/foils that they are grown on [131]. Sn is known to have little to no solubility with Si, whose properties were explored in this thesis, and Al. An Al(111) surface may provide a commensurate surface structure to support a stanene layer. Preliminary DFT calculations have shown that a stanene layer on Al(111) may be stable. Difficulties of using an Al(111) substrate would be the preparation of an Al crystal for use in a UHV system.

The graphene growth on Cu-silicide presented in this thesis was performed using a scalable CVD method. Although this work proved that graphene could be successfully grown, the electrical properties of the as-grown graphene crystals on Cu_3Si have yet to be studied. Future work should include the STM imaging and STS study of these as-grown graphene crystals

to see if the graphene to silicide interface matches that of the DFT simulations presented in this thesis. Since the Cu_3Si structures were self-assembled into random island sizes and geometries, other future work should include growing graphene on patterned silicide areas. This would still provide direct integration of graphene on Si substrates, and provide a method for directing the graphene growth by using the patterned silicide area. Additionally, future research should explore whether graphene may be grown using CVD on other silicide surface.

Much of the future work recommended here would go towards a further understanding of low dimensional material integration on Si. These can advance technological developments into their integration and use for future technology.

APPENDIX A

Background Correction

Optical spectroscopy techniques such as Raman and XRD often have a curvature to the raw spectra due to the movement or rotation of optics or a detector during scanning. This results in data that has a linear or curvilinear skew. In this research, Matlab® software was used to perform background correction on both the Raman and XRD data before plotting. To perform a background correction, a polynomial function is fitted to the general shape of the spectra using a least squares method. Corrected data is then replotted after subtracting the fitted polynomial function from the raw data. An example of a Raman signal before and after background correction is shown in Figure 31.

For example, if the data in Figure 31a is in a two column matrix. Area under the plotted intensity column is fitted to a set of squares using the Matlab® function “linspace” to create a least squares set of points. Those points are then used by the function “polyfit” to generate a matching polynomial function following background curve of the raw data. This polynomial function is then subtracted from the data to level the data, which maintains peak positions and intensity.

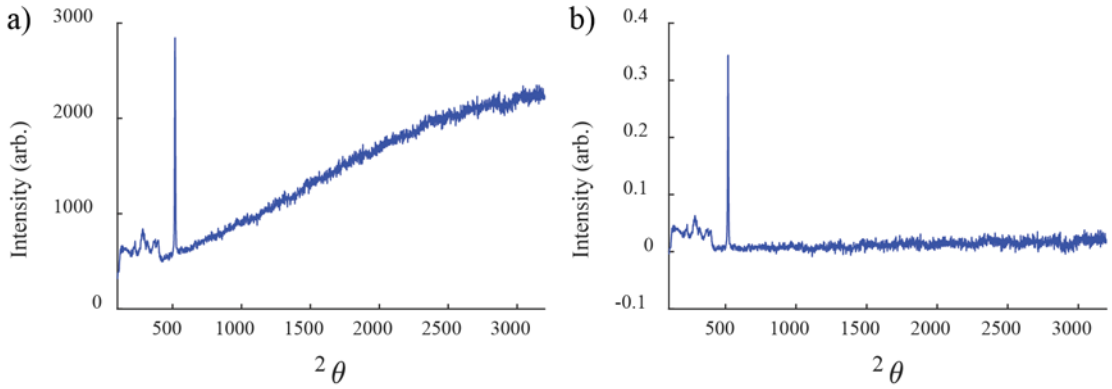

Figure 31 Example of raw Raman spectra before (a) and after (b) background correction and normalization.

APPENDIX B

Journal Policies Regarding the Reprint of Published Work

- AIP Publishing which oversees Applied Physics Letters states in their "License to publish agreement" under author rights and permitted uses that the authors may re-use their own work as long as it is properly cited.

Author Rights and Permitted Uses

Subject to the rights herein granted to AIP Publishing, each Copyright Owner retains ownership of copyright and all other proprietary rights such as patent rights in the Work.

Each Copyright Owner retains the following nonexclusive rights to use the Work, without obtaining permission from AIP Publishing, in keeping with professional publication ethics, and provided clear credit is given to its first publication in an AIP Publishing journal. Any reuse must include a full credit line acknowledging AIP Publishing's publication and a link to the VOR on AIP Publishing's site.

5. Reprint the Version of Record (VOR) in print collections written by the Author, or in the Author's thesis or dissertation. It is understood and agreed that the thesis or dissertation may be made available electronically on the university's site or in its repository and that copies may be offered for sale on demand.

- Nature Research grants authors permission to re-use their work within a thesis document as long as it is properly citied. Screenshot of Nature Research's Author request is shown below.

Permission requests from authors

The authors of articles published by Nature Research, or the authors' designated agents, do not usually need to seek permission for re-use of their material as long as the journal is credited with initial publication. For further information about the terms of re-use for authors please see below.

Author Requests

If you are the author of this content (or his/her designated agent) please read the following. Since 2003, ownership of copyright in in original research articles remains with the Authors*, and provided that, when reproducing the Contribution or extracts from it, the Authors acknowledge first and reference publication in the Journal, the Authors retain the following non-exclusive rights:

a. To reproduce the Contribution in whole or in part in any printed volume (book or thesis) of which they are the author(s).
b. They and any academic institution where they work at the time may reproduce the Contribution for the purpose of course teaching.
c. To reuse figures or tables created by them and contained in the Contribution in other works created by them.
d. To post a copy of the Contribution as accepted for publication after peer review (in Word or Tex format) on the Author's own web site, or the Author's institutional repository, or the Author's funding body's archive, six months after publication of the printed or online edition of the Journal, provided that they also link to the Journal article on Nature Research's web site (eg through the DOI).

REFERENCES

[1] D. S. L. Abergel, V. Apalkov, J. Berashevich, K. Ziegler, and T. Chakraborty, "Properties of graphene: a theoretical perspective," *Advances in Physics,* vol. 59, pp. 261-482, 2010/07/01 2010.

[2] A. H. Castro Neto, F. Guinea, N. M. R. Peres, K. S. Novoselov, and A. K. Geim, "The electronic properties of graphene," *Reviews of Modern Physics,* vol. 81, pp. 109-162, 01/14/ 2009.

[3] M. F. L. De Volder, S. H. Tawfick, R. H. Baughman, and A. J. Hart, "Carbon Nanotubes: Present and Future Commercial Applications," *Science,* vol. 339, pp. 535-539, 2013.

[4] J. Tersoff, C. Teichert, and M. G. Lagally, "Self-Organization in Growth of Quantum Dot Superlattices," *Physical Review Letters,* vol. 76, pp. 1675-1678, 03/04/ 1996.

[5] K. S. Novoselov, A. K. Geim, S. V. Morozov, D. Jiang, Y. Zhang, S. V. Dubonos, *et al.*, "Electric Field Effect in Atomically Thin Carbon Films," *Science,* vol. 306, pp. 666-669, October 22, 2004 2004.

[6] K. S. Novoselov, A. K. Geim, S. V. Morozov, D. Jiang, M. I. Katsnelson, I. V. Grigorieva, *et al.*, "Two-dimensional gas of massless Dirac fermions in graphene," *Nature,* vol. 438, pp. 197-200, 11/10/print 2005.

[7] S. V. Morozov, K. S. Novoselov, M. I. Katsnelson, F. Schedin, D. C. Elias, J. A. Jaszczak, *et al.*, "Giant Intrinsic Carrier Mobilities in Graphene and Its Bilayer," *Physical Review Letters,* vol. 100, p. 016602, 01/07/ 2008.

[8] A. K. Geim and K. S. Novoselov, "The rise of graphene," *Nature Materials,* vol. 6, pp. 183-191, Mar 2007.

[9] D. C. Elias, R. V. Gorbachev, A. S. Mayorov, S. V. Morozov, A. A. Zhukov, P. Blake, *et al.*, "Dirac cones reshaped by interaction effects in suspended graphene," *Nat Phys,* vol. 7, pp. 701-704, 2011.

[10] C. Berger, Z. Song, X. Li, X. Wu, N. Brown, C. Naud, *et al.*, "Electronic confinement and coherence in patterned epitaxial graphene," *Science,* vol. 312, pp. 1191-1196, May 26 2006.

[11] G. Le Lay, B. Aufray, C. Leandri, H. Oughaddou, J. P. Biberian, P. De Padova, *et al.*, "Physics and chemistry of silicene nano-ribbons," *Applied Surface Science,* vol. 256, pp. 524-529, Oct 2009.

[12] C. Hwang, D. A. Siegel, S.-K. Mo, W. Regan, A. Ismach, Y. Zhang, *et al.*, "Fermi velocity engineering in graphene by substrate modification," *Sci. Rep.,* vol. 2, 2012.

[13] S. Kim, I. Jo, D. C. Dillen, D. A. Ferrer, B. Fallahazad, Z. Yao, *et al.*, "Direct Measurement of the Fermi Energy in Graphene Using a Double-Layer Heterostructure," *Physical Review Letters,* vol. 108, p. 116404, 2012.

[14] S. Das Sarma, S. Adam, E. H. Hwang, and E. Rossi, "Electronic transport in two-dimensional graphene," *Reviews of Modern Physics,* vol. 83, pp. 407-470, 2011.

[15] C. R. Woods, L. Britnell, A. Eckmann, R. S. Ma, J. C. Lu, H. M. Guo, *et al.*, "Commensurate-incommensurate transition in graphene on hexagonal boron nitride," *Nat Phys,* vol. 10, pp. 451-456, 06//print 2014.

[16] Y. Zhang, T.-T. Tang, C. Girit, Z. Hao, M. C. Martin, A. Zettl, *et al.*, "Direct observation of a widely tunable bandgap in bilayer graphene," *Nature,* vol. 459, pp. 820-823, 06/11/print 2009.

[17] G. Giovannetti, P. A. Khomyakov, G. Brocks, P. J. Kelly, and J. van den Brink, "Substrate-induced band gap in graphene on hexagonal boron nitride: *Ab initio* density functional calculations," *Physical Review B*, vol. 76, p. 073103, 08/16/ 2007.

[18] S. Tang, J. Yu, and L. Liu, "Tunable doping and band gap of graphene on functionalized hexagonal boron nitride with hydrogen and fluorine," *Physical Chemistry Chemical Physics*, vol. 15, pp. 5067-5077, 2013.

[19] H. Vita, S. Bottcher, K. Horn, E. N. Voloshina, R. E. Ovcharenko, T. Kampen, *et al.*, "Understanding the origin of band gap formation in graphene on metals: graphene on Cu/Ir(111)," *Sci. Rep.*, vol. 4, 07/16/online 2014.

[20] Y. Lee, S. Bae, H. Jang, S. Jang, S.-E. Zhu, S. H. Sim, *et al.*, "Wafer-Scale Synthesis and Transfer of Graphene Films," *Nano Letters*, vol. 10, pp. 490-493, 2010/02/10 2010.

[21] S. Gorantla, A. Bachmatiuk, J. Hwang, H. A. Alsalman, J. Y. Kwak, T. Seyller, *et al.*, "A universal transfer route for graphene," *Nanoscale*, vol. 6, pp. 889-896, 2014.

[22] W.-H. Lin, T.-H. Chen, J.-K. Chang, J.-I. Taur, Y.-Y. Lo, W.-L. Lee, *et al.*, "A Direct and Polymer-Free Method for Transferring Graphene Grown by Chemical Vapor Deposition to Any Substrate," *ACS Nano*, vol. 8, pp. 1784-1791, 2014/02/25 2014.

[23] W. Regan, N. Alem, B. Alemán, B. Geng, Ç. Girit, L. Maserati, *et al.*, "A direct transfer of layer-area graphene," *Applied Physics Letters*, vol. 96, p. 113102, 2010.

[24] J. W. Suk, A. Kitt, C. W. Magnuson, Y. Hao, S. Ahmed, J. An, *et al.*, "Transfer of CVD-Grown Monolayer Graphene onto Arbitrary Substrates," *ACS Nano*, vol. 5, pp. 6916-6924, 2011/09/27 2011.

[25] A. L. Schmitt, J. M. Higgins, J. R. Szczech, and S. Jin, "Synthesis and applications of metal silicide nanowires," *Journal of Materials Chemistry*, vol. 20, pp. 223-235, 2010.

[26] J. R. Tucker, C. Wang, and T. C. Shen, "Metal silicide patterning: a new approach to silicon nanoelectronics," *Nanotechnology*, vol. 7, p. 275, 1996.

[27] W. Tang, S. A. Dayeh, S. T. Picraux, J. Y. Huang, and K. N. Tu, "Ultrashort Channel Silicon Nanowire Transistors with Nickel Silicide Source/Drain Contacts," *Nano Letters*, vol. 12, pp. 3979-3985, Aug 2012.

[28] V. Babenko, A. T. Murdock, A. A. Koos, J. Britton, A. Crossley, P. Holdway, *et al.*, "Rapid epitaxy-free graphene synthesis on silicidated polycrystalline platinum," *Nat Commun*, vol. 6, p. 7536, 2015.

[29] O. Vilkov, A. Fedorov, D. Usachov, L. V. Yashina, A. V. Generalov, K. Borygina, *et al.*, "Controlled assembly of graphene-capped nickel, cobalt and iron silicides," *Sci. Rep.*, vol. 3, p. 2168, 2013.

[30] J. J. L. Morton, D. R. McCamey, M. A. Eriksson, and S. A. Lyon, "Embracing the quantum limit in silicon computing," *Nature*, vol. 479, pp. 345-353, 11/17/print 2011.

[31] H. Bluhm, S. Foletti, I. Neder, M. Rudner, D. Mahalu, V. Umansky, *et al.*, "Dephasing time of GaAs electron-spin qubits coupled to a nuclear bath exceeding 200 μs," *Nat Phys*, vol. 7, pp. 109-113, 02//print 2011.

[32] W. F. Koehl, B. B. Buckley, F. J. Heremans, G. Calusine, and D. D. Awschalom, "Room temperature coherent control of defect spin qubits in silicon carbide," *Nature*, vol. 479, pp. 84-87, 11/03/print 2011.

[33] Veldhorst M, J. C. C. Hwang, C. H. Yang, A. W. Leenstra, B. de Ronde, J. P. Dehollain, *et al.*, "An addressable quantum dot qubit with fault-tolerant control-fidelity," *Nat Nano*, vol. 9, pp. 981-985, 12//print 2014.

[34] L. Dózsa, G. Molnár, Z. J. Horváth, A. L. Tóth, J. Gyulai, V. Raineri, *et al.*, "Investigation of the morphology and electrical characteristics of FeSi2 quantum dots on silicon," *Applied Surface Science,* vol. 234, pp. 60-66, 2004.

[35] L. Fernández, M. Löffler, J. Cordón, and E. Ortega, "Tuning reactive epitaxy of silicides with surface steps: Silicide quantum dot arrays on Si(111)," *Superlattices and Microstructures,* vol. 44, pp. 378-384, 2008.

[36] L. Fernandez, M. Loffler, J. Cordon, and J. E. Ortega, "Self-assembly of silicide quantum dot arrays on stepped silicon surfaces by reactive epitaxy," *Applied Physics Letters,* vol. 91, pp. 263106-263106-3, 2007.

[37] M. Cegiel, M. Bazarnik, and R. Czajka, "STM investigation of cobalt silicide nanostructures growth on Si(111)-(√19×√19) substrate," *Central European Journal of Physics,* vol. 7, pp. 291-294, 2009/06/01 2009.

[38] U. Banin, Y. Cao, D. Katz, and O. Millo, "Identification of atomic-like electronic states in indium arsenide nanocrystal quantum dots," *Nature,* vol. 400, pp. 542-544, 08/05/print 1999.

[39] P. E. D. S. Rodriguez, P. Aseev, V. J. Gómez, P. Kumar, N. U. H. Alvi, E. Calleja, *et al.*, "Stranski-Krastanov InN/InGaN quantum dots grown directly on Si(111)," *Applied Physics Letters,* vol. 106, p. 023105, 2015.

[40] F. M. Ross, J. Tersoff, and R. M. Tromp, "Coarsening of Self-Assembled Ge Quantum Dots on Si(001)," *Physical Review Letters,* vol. 80, pp. 984-987, 02/02/ 1998.

[41] S. Küfner, M. Fitzner, and F. Bechstedt, "Topological α-Sn surface states versus film thickness and strain," *Physical Review B,* vol. 90, p. 125312, 09/22/ 2014.

[42] A. Barfuss, L. Dudy, M. R. Scholz, H. Roth, P. Höpfner, C. Blumenstein, *et al.*, "Elemental Topological Insulator with Tunable Fermi Level: Strained $\ensuremath{\alpha}$-Sn on InSb(001)," *Physical Review Letters,* vol. 111, p. 157205, 10/11/ 2013.

[43] R. W. Olesinski and G. J. Abbaschian, "The Si−Sn (Silicon−Tin) system," *Bulletin of Alloy Phase Diagrams,* vol. 5, pp. 273-276, 1984.

[44] S. Modesti, L. Petaccia, G. Ceballos, I. Vobornik, G. Panaccione, G. Rossi, *et al.*, "Insulating Ground State of Sn/Si(111) (√3×√3)R30°," *Physical Review Letters,* vol. 98, p. 126401, 03/19/ 2007.

[45] G. Profeta and E. Tosatti, "Triangular Mott-Hubbard Insulator Phases of Sn/Si(111) and Sn/Ge(111) Surfaces," *Physical Review Letters,* vol. 98, p. 086401, 02/21/ 2007.

[46] L. Ottaviano, M. Crivellari, L. Lozzi, and S. Santucci, "STM investigation of the α-Sn/Si(111) phase at 120 K," *Surface Science,* vol. 445, pp. L41-L46, 1/10/ 2000.

[47] Y. Sugimoto, M. Abe, S. Hirayama, and S. Morita, "Highly resolved non-contact atomic force microscopy images of the Sn/Si(111)-(2√3×2√3)R30° surface," *Nanotechnology,* vol. 17, pp. 4235-4239, 2006 2006.

[48] C. Törnevik, M. Hammar, N. G. Nilsson, and S. A. Flodström, "Epitaxial growth of Sn on Si(111): A direct atomic-structure determination of the (2√3×2√3)R30° reconstructed surface," *Physical Review B,* vol. 44, pp. 13144-13147, 12/15/ 1991.

[49] D. Cherns, G. R. Anstis, J. L. Hutchison, and J. C. H. Spence, "Atomic structure of the NiSi2/(111)Si interface," *Philosophical Magazine A,* vol. 46, pp. 849-862, 1982/11/01 1982.

[50] T. Nishimura, J. Takeda, Y. Asami, Y. Hoshino, and Y. Kido, "Initial growth processes of ultra-thin Ni-layers on Si(1 1 1) and electronic structure of epitaxially grown NiSi2," *Surface Science,* vol. 588, pp. 71-82, 8/20/ 2005.

[51] R. T. Tung, "EPITAXIAL COSI2 AND NISI2 THIN-FILMS," *Materials Chemistry and Physics,* vol. 32, pp. 107-133, Aug 1992.

[52] H. von Känel, "Growth and characterization of epitaxial Ni and Co silicides," *Materials Science Reports,* vol. 8, pp. 193-269, 5// 1992.

[53] T. Ichinokawa, T. Tani, and A. Sayama, "Formation of the Si(111)√19 ×√19 structure induced by Ni impurity at low coverage," *Surface Science,* vol. 219, pp. 395-406, 1989/09/02 1989.

[54] D. T. Wang, N. Esser, M. Cardona, and J. Zegenhagen, "Epitaxy of Sn on Si(111)," *Surface Science,* vol. 343, pp. 31-36, 12/1/ 1995.

[55] S. Qin, J. Kim, Q. Niu, and C.-K. Shih, "Superconductivity at the Two-Dimensional Limit," *Science,* vol. 324, pp. 1314-1317, 2009.

[56] Z. Wei, Z. Ye, K. D. D. Rathnayaka, I. F. Lyuksyutov, W. Wu, and D. G. Naugle, "Superconductivity of a Sn film controlled by an array of Co nanowires," *Physica C: Superconductivity,* vol. 479, pp. 41-44, 9// 2012.

[57] T. Zhang, P. Cheng, W.-J. Li, Y.-J. Sun, G. Wang, X.-G. Zhu, *et al.*, "Superconductivity in one-atomic-layer metal films grown on Si(111)," *Nat Phys,* vol. 6, pp. 104-108, 02//print 2010.

[58] M. Göthelid, M. Björkqvist, T. M. Grehk, G. Le Lay, and U. O. Karlsson, "Metal-semiconductor fluctuation in the Sn adatoms in the Si(111)-Sn and Ge(111)-Sn (√3√3)R30° reconstructions," *Physical Review B,* vol. 52, pp. R14352-R14355, 11/15/ 1995.

[59] B. Ressel, C. Di Teodoro, G. Profeta, L. Ottaviano, V. Cháb, and K. C. Prince, "Scanning tunneling spectroscopy investigation of the (√3×√3)R30° Sn/Si(1 1 1) α and γ surfaces," *Surface Science,* vol. 562, pp. 128-136, 8/1/ 2004.

[60] I. Yi, Y. Sugimoto, R. Nishi, and S. Morita, "Study on topographic images of Sn/Si(1 1 1)-(√3 × √3)R30° surface by non-contact AFM," *Surface Science,* vol. 600, pp. 3382-3387, 9/1/ 2006.

[61] P. E. J. Eriksson, J. R. Osiecki, K. Sakamoto, and R. I. G. Uhrberg, "Atomic and electronic structures of the ordered (2√3×2√3)R30° phase on the Si(111):Sn surface," *Physical Review B,* vol. 81, p. 235410, 06/07/ 2010.

[62] T. Ichikawa and K. Cho, "Structural Study of Si(111)(2√3×2√3)R30°–Sn Surfaces," *Japanese Journal of Applied Physics,* vol. 42, p. 5239, 2003.

[63] L. Ottaviano, G. Profeta, L. Petaccia, C. B. Nacci, and S. Santucci, "Structural and electronic properties of the Sn/Si(1 1 1)-(2√3×2√3)R30° surface revised," *Surface Science,* vol. 554, pp. 109-118, 2004.

[64] J. M. Carpinelli, H. H. Weitering, M. Bartkowiak, R. Stumpf, and E. W. Plummer, "Surface Charge Ordering Transition: α Phase of Sn/Ge(111)," *Physical Review Letters,* vol. 79, pp. 2859-2862, 10/13/ 1997.

[65] J. M. Carpinelli, H. H. Weitering, E. W. Plummer, and R. Stumpf, "Direct observation of a surface charge density wave," *Nature,* vol. 381, pp. 398-400, 05/30/print 1996.

[66] R. Cortés, A. Tejeda, J. Lobo-Checa, C. Didiot, B. Kierren, D. Malterre, *et al.*, "Competing charge ordering and Mott phases in a correlated Sn/Ge(111) two-dimensional triangular lattice," *Physical Review B,* vol. 88, p. 125113, 09/06/ 2013.

[67] D. Sholl and J. A. Steckel, *Density Functional Theory: A Practical Introduction*. US: John Wiley & Sons, Inc. , 2009.
[68] N. W. Ashcroft and N. D. Mermin, *Solid state physics*. New York: Holt, Rinehart and Winston, 1976.
[69] P. Hohenberg and W. Kohn, "Inhomogeneous Electron Gas," *Physical Review,* vol. 136, pp. B864-B871, 11/09/ 1964.
[70] W. Kohn and L. J. Sham, "Self-Consistent Equations Including Exchange and Correlation Effects," *Physical Review,* vol. 140, pp. A1133-A1138, 1965.
[71] A. D. Becke, "A new mixing of Hartree–Fock and local density-functional theories," *The Journal of Chemical Physics,* vol. 98, pp. 1372-1377, 1993/01/15 1993.
[72] J. P. Perdew, K. Burke, and M. Ernzerhof, "Generalized Gradient Approximation Made Simple," *Physical Review Letters,* vol. 77, pp. 3865-3868, 1996.
[73] J. P. Perdew, K. Burke, and M. Ernzerhof, "Generalized Gradient Approximation Made Simple [Phys. Rev. Lett. 77, 3865 (1996)]," *Physical Review Letters,* vol. 78, pp. 1396-1396, 02/17/ 1997.
[74] P. Schwerdtfeger, "The Pseudopotential Approximation in Electronic Structure Theory," *ChemPhysChem,* vol. 12, pp. 3143-3155, 2011.
[75] P. E. Blöchl, "Projector augmented-wave method," *Physical Review B,* vol. 50, pp. 17953-17979, 12/15/ 1994.
[76] G. Kresse and J. Furthmüller, "Efficient iterative schemes for ab initio total-energy calculations using a plane-wave basis set," *Physical Review B,* vol. 54, pp. 11169-11186, 10/15/ 1996.
[77] G. Kresse and D. Joubert, "From ultrasoft pseudopotentials to the projector augmented-wave method," *Physical Review B,* vol. 59, pp. 1758-1775, 01/15/ 1999.
[78] R. Núñez-González, A. Reyes-Serrato, D. H. Galván, and A. Posada-Amarillas, "DFT calculation of the electronic properties and EEL spectrum of NiSi2," *Computational Materials Science,* vol. 49, pp. 15-20, 2010.
[79] L. B. Drissi, E. H. Saidi, M. Bousmina, and O. Fassi-Fehri, "DFT investigations of the hydrogenation effect on silicene/graphene hybrids," *Journal of Physics-Condensed Matter,* vol. 24, p. 485502, Dec 2012.
[80] B. van den Broek, M. Houssa, E. Scalise, G. Pourtois, V. V. Afanas‘ev, and A. Stesmans, "First-principles electronic functionalization of silicene and germanene by adatom chemisorption," *Applied Surface Science,* vol. 291, pp. 104-108, 2014.
[81] M. Houssa, B. van den Broek, E. Scalise, B. Ealet, G. Pourtois, D. Chiappe, *et al.*, "Theoretical aspects of graphene-like group IV semiconductors," *Applied Surface Science,* vol. 291, pp. 98-103, 2014.
[82] S. Lebegue and O. Eriksson, "Electronic structure of two-dimensional crystals from ab initio theory," *Physical Review B,* vol. 79, p. 115409, Mar 2009.
[83] L. Liu and Z. Shen, "Bandgap engineering of graphene: A density functional theory study," *Applied Physics Letters,* vol. 95, pp. -, 2009.
[84] H. Yildirim, A. Kinaci, Z.-J. Zhao, M. K. Y. Chan, and J. P. Greeley, "First-Principles Analysis of Defect-Mediated Li Adsorption on Graphene," *ACS Applied Materials & Interfaces,* vol. 6, pp. 21141-21150, 2014/12/10 2014.
[85] G. Kresse and J. Furthmüller, "Efficiency of ab-initio total energy calculations for metals and semiconductors using a plane-wave basis set," *Computational Materials Science,* vol. 6, pp. 15-50, 7// 1996.

[86] G. Kresse and J. Hafner, "Ab initio molecular-dynamics simulation of the liquid-metal-amorphous-semiconductor transition in germanium," *Physical Review B*, vol. 49, pp. 14251-14269, 05/15/ 1994.
[87] M. Brandbyge, J.-L. Mozos, P. Ordejón, J. Taylor, and K. Stokbro, "Density-functional method for nonequilibrium electron transport," *Physical Review B*, vol. 65, p. 165401, 2002.
[88] M. S. José, A. Emilio, D. G. Julian, G. Alberto, J. Javier, O. Pablo, *et al.*, "The SIESTA method for ab initio order- N materials simulation," *Journal of Physics: Condensed Matter*, vol. 14, p. 2745, 2002.
[89] K. Momma and F. Izumi, "VESTA 3 for three-dimensional visualization of crystal, volumetric and morphology data," *Journal of Applied Crystallography*, vol. 44, pp. 1272-1276, 2011.
[90] (2014). *p4vasp*. Available: http://www.p4vasp.at/
[91] A. Dahal, J. Gunasekera, L. Harringer, D. K. Singh, and D. J. Singh, "Metallic nickel silicides: Experiments and theory for NiSi and first principles calculations for other phases," *Journal of Alloys and Compounds*, vol. 672, pp. 110-116, 7/5/ 2016.
[92] A. J. Morris, C. P. Grey, and C. J. Pickard, "Thermodynamically stable lithium silicides and germanides from density functional theory calculations," *Physical Review B*, vol. 90, p. 054111, 08/21/ 2014.
[93] C. Zhang, X. Kuang, Y. Jin, C. Lu, D. Zhou, P. Li, *et al.*, "Prediction of Stable Ruthenium Silicides from First-Principles Calculations: Stoichiometries, Crystal Structures, and Physical Properties," *ACS Applied Materials & Interfaces*, vol. 7, pp. 26776-26782, 2015/12/09 2015.
[94] P. A. Khomyakov, G. Giovannetti, P. C. Rusu, G. Brocks, J. van den Brink, and P. J. Kelly, "First-principles study of the interaction and charge transfer between graphene and metals," *Physical Review B*, vol. 79, p. 195425, 05/20/ 2009.
[95] M. Vanin, J. J. Mortensen, A. K. Kelkkanen, J. M. Garcia-Lastra, K. S. Thygesen, and K. W. Jacobsen, "Graphene on metals: A van der Waals density functional study," *Physical Review B*, vol. 81, p. 081408, 02/23/ 2010.
[96] P. A. Bennett, S. A. Parikh, and D. G. Cahill, "Scanning-Tunneling-Microscopy Studies of Nucleation and Growth in a Reactive, Epitaxial System - Co/Si(111)," *Journal of Vacuum Science & Technology a-Vacuum Surfaces and Films*, vol. 11, pp. 1680-1685, Jul-Aug 1993.
[97] S. Y. Chen and L. J. Chen, "Self-assembled epitaxial $NiSi_2$ nanowires on Si(001) by reactive deposition epitaxy," *Thin Solid Films*, vol. 508, pp. 222-225, Jun 2006.
[98] A. Vantomme, M.-A. Nicolet, R. G. Long, J. E. Mahan, and F. S. Pool, "Reactive deposition epitaxy of CrSi2," *Applied Surface Science*, vol. 73, pp. 146-152, 1993/11/02 1993.
[99] A. G. Italyantsev, "Basic processes accompanying solid-phase reactions on the silicon surface," *Journal of Applied Physics*, vol. 79, pp. 2369-2375, Mar 1996.
[100] M. J. Madou, *Fundamentals of Microfabrication and Nanotechnology*, 1st ed. vol. II: Taylor & Francis Group, LLC, 2011.
[101] X. Li, W. Cai, J. An, S. Kim, J. Nah, D. Yang, *et al.*, "Large-Area Synthesis of High-Quality and Uniform Graphene Films on Copper Foils," *Science*, vol. 324, pp. 1312-1314, June 5, 2009 2009.

[102] R. Lv, J. A. Robinson, R. E. Schaak, D. Sun, Y. Sun, T. E. Mallouk, *et al.*, "Transition Metal Dichalcogenides and Beyond: Synthesis, Properties, and Applications of Single- and Few-Layer Nanosheets," *Accounts of Chemical Research,* vol. 48, pp. 56-64, 2015/01/20 2015.

[103] K. L. Choy, "Chemical vapour deposition of coatings," *Progress in Materials Science,* vol. 48, pp. 57-170, // 2003.

[104] L. Huang, Q. H. Chang, G. L. Guo, Y. Liu, Y. Q. Xie, T. Wang, *et al.*, "Synthesis of high-quality graphene films on nickel foils by rapid thermal chemical vapor deposition," *Carbon,* vol. 50, pp. 551-556, 2// 2012.

[105] G. Binning, H. Rohrer, C. Gerber, and E. Weibel, "SURFACE STUDIES BY SCANNING TUNNELING MICROSCOPY," *Physical Review Letters,* vol. 49, pp. 57-61, 1982.

[106] R. Wiesendanger, *Scanning Probe Microscopy and Spectroscopy: Methods and Applications*. Cambridge: Cambridge University Press, 1994.

[107] P. Klapetek, "Front Matter A2 - Klapetek, Petr," in *Quantitative Data Processing in Scanning Probe Microscopy*, ed: William Andrew Publishing, 2013, pp. i-ii.

[108] D. Nečas and P. Klapetek, "Gwyddion: an open-source software for SPM data analysis," *Central European Journal of Physics,* vol. 10, pp. 181-188, 2012.

[109] D. J. Gardiner and P. R. Graves, *Practial Raman Spectroscopy*. Berlin Heidelberg: Springer-Verlag, 1989.

[110] A. C. Ferrari, "Raman spectroscopy of graphene and graphite: Disorder, electron–phonon coupling, doping and nonadiabatic effects," *Solid State Communications,* vol. 143, pp. 47-57, 7// 2007.

[111] L. M. Malard, M. A. Pimenta, G. Dresselhaus, and M. S. Dresselhaus, "Raman spectroscopy in graphene," *Physics Reports,* vol. 473, pp. 51-87, 4// 2009.

[112] B. D. Cullity, *Elements of X-Ray Diffraction*. Reading, MA: Addison-Wesley Publishing Company, Inc. , 1956.

[113] H. P. Klug and L. E. Alexander, *X-Ray Diffraction Procedures: For Polycrystalline and Amorphous Materials*. US: John Wiley & Sons, Inc. , 1974.

[114] B. Lalmi, H. Oughaddou, H. Enriquez, A. Kara, S. Vizzini, B. Ealet, *et al.*, "Epitaxial growth of a silicene sheet," *Applied Physics Letters,* vol. 97, pp. -, 2010.

[115] S. Cahangirov, M. Audiffred, P. Z. Tang, A. Iacomino, W. H. Duan, G. Merino, *et al.*, "Electronic structure of silicene on Ag(111): Strong hybridization effects," *Physical Review B,* vol. 88, Jul 2013.

[116] A. Kara, H. Enriquez, A. P. Seitsonen, L. Voon, S. Vizzini, B. Aufray, *et al.*, "A review on silicene - New candidate for electronics," *Surface Science Reports,* vol. 67, pp. 1-18, Jan 2012.

[117] N. Gao, J. C. Li, and Q. Jiang, "Bandgap opening in silicene: Effect of substrates," *Chemical Physics Letters,* vol. 592, pp. 222-226, 2014.

[118] H. Liu, J. Gao, and J. Zhao, "Silicene on substrates: interaction mechanism and growth behavior," *Journal of Physics: Conference Series,* vol. 491, p. 012007, 2014.

[119] A. J. Mannix, B. Kiraly, B. L. Fisher, M. C. Hersam, and N. P. Guisinger, "Silicon Growth at the Two-Dimensional Limit on Ag(111)," *ACS Nano,* vol. 8, pp. 7538-7547, 2014.

[120] Z. Jin, G. A. Bhat, M. Yeung, H. S. Kwok, and M. Wong, "Nickel induced crystallization of amorphous silicon thin films," *Journal of Applied Physics,* vol. 84, pp. 194-200, 1998.

[121] J. A. Schmidt, N. Budini, P. Rinaldi, R. D. Arce, and R. H. Buitrago, "Nickel-induced crystallization of amorphous silicon," *Journal of Physics: Conference Series,* vol. 167, p. 012046, 2009.
[122] N. Budini, P. A. Rinaldi, R. D. Arce, J. A. Schmidt, R. R. Koropecki, and R. H. Buitrago, "Vacuum-enhanced nickel-induced crystallization of hydrogenated amorphous silicon," *Journal of Applied Physics,* vol. 112, p. 073506, 2012.
[123] R. T. Tung and F. Schrey, "Growth of epitaxial NiSi2 on Si(111) at room temperature," *Applied Physics Letters,* vol. 55, pp. 256-258, 1989.
[124] S. Grimme, "Semiempirical GGA-type density functional constructed with a long-range dispersion correction," *Journal of Computational Chemistry,* vol. 27, pp. 1787-1799, 2006.
[125] J. Vrijmoeth, P. M. Zagwijn, J. W. M. Frenken, and J. F. van der Veen, "Monolayer resolution in medium-energy ion-scattering experiments on the NiSi2(111) surface," *Physical Review Letters,* vol. 67, pp. 1134-1137, 1991.
[126] R. Quhe, Y. Yuan, J. Zheng, Y. Wang, Z. Ni, J. Shi, *et al.*, "Does the Dirac Cone Exist in Silicene on Metal Substrates?," *Scientific Reports,* vol. 4, p. 5476, 2014.
[127] E. Vlieg, A. E. M. J. Fischer, J. F. van Der Veen, B. N. Dev, and G. Materlik, "Geometric structure of the NiSi2-Si(111) interface: An X-ray standing-wave analysis," *Surface Science,* vol. 178, pp. 36-46, 1986/12/03 1986.
[128] E. J. van Loenen, J. W. M. Frenken, J. F. van der Veen, and S. Valeri, "Real-space determination of atomic structure and bond relaxation at the NiSi2-Si(111) interface," *Physical Review Letters,* vol. 54, pp. 827-830, 02/25/ 1985.
[129] J. A. Yan, R. Stein, D. M. Schaefer, X. Q. Wang, and M. Y. Chou, "Electron-phonon coupling in two-dimensional silicene and germanene," *Physical Review B,* vol. 88, p. 121403, 2013.
[130] Z. Ni, Q. Liu, K. Tang, J. Zheng, J. Zhou, R. Qin, *et al.*, "Tunable Bandgap in Silicene and Germanene," *Nano Letters,* vol. 12, pp. 113-118, 2012/01/11 2011.
[131] N. J. Roome and J. D. Carey, "Beyond Graphene: Stable Elemental Monolayers of Silicene and Germanene," *ACS Applied Materials & Interfaces,* vol. 6, pp. 7743-7750, 2014/05/28 2014.
[132] M. Houssa, E. Scalise, K. Sankaran, G. Pourtois, V. V. Afanas'ev, and A. Stesmans, "Electronic properties of hydrogenated silicene and germanene," *Applied Physics Letters,* vol. 98, p. 223107, 2011.
[133] J.-Y. Cheng, M. K. Y. Chan, and C. M. Lilley, "Enabling direct silicene integration in electronics: First principles study of silicene on NiSi2(111)," *Applied Physics Letters,* vol. 109, p. 133111, 2016.
[134] K. Toyoda, K. Nozawa, N. Matsukawa, and S. Yoshii, "Density Functional Theoretical Study of Graphene on Transition-Metal Surfaces: The Role of Metal d-Band in the Potential-Energy Surface," *The Journal of Physical Chemistry C,* vol. 117, pp. 8156-8160, 2013/04/25 2013.
[135] F. Hiebel, P. Mallet, J. Y. Veuillen, and L. Magaud, "Graphene on the carbon face of SiC: Electronic structure modification by hydrogen intercalation," *Physical Review B,* vol. 83, p. 075438, 02/28/ 2011.
[136] F. Varchon, R. Feng, J. Hass, X. Li, B. N. Nguyen, C. Naud, *et al.*, "Electronic Structure of Epitaxial Graphene Layers on SiC: Effect of the Substrate," *Physical Review Letters,* vol. 99, p. 126805, 09/20/ 2007.

[137] M. Wu, C. Cao, and J. Z. Jiang, "Light non-metallic atom (B, N, O and F)-doped graphene: a first-principles study," *Nanotechnology,* vol. 21, Dec 2010.
[138] F. M. d'Heurle, "The Oxidation of Silicides on Silicon," in *The Physics and Chemistry of SiO2 and the Si-SiO2 Interface*, C. R. Helms and B. E. Deal, Eds., ed Boston, MA: Springer US, 1988, pp. 85-94.
[139] Y.-L. Cheng, M.-K. Shiau, W.-Y. Chung, and Y.-L. Wang, "Competition of Electromigration Reliability in Copper and Nickel-Silicide," *Journal of The Electrochemical Society,* vol. 158, pp. H174-H177, February 1, 2011 2011.
[140] L. Stolt, A. Charai, F. M. D'Heurle, P. M. Fryer, and J. M. E. Harper, "Formation of Cu3Si and its catalytic effect on silicon oxidation at room temperature," *Journal of Vacuum Science & Technology A,* vol. 9, pp. 1501-1505, 1991.
[141] J. S. Bunch, S. S. Verbridge, J. S. Alden, A. M. van der Zande, J. M. Parpia, H. G. Craighead, *et al.*, "Impermeable Atomic Membranes from Graphene Sheets," *Nano Letters,* vol. 8, pp. 2458-2462, 2008/08/01 2008.
[142] S. S. Roy and M. S. Arnold, "Improving Graphene Diffusion Barriers via Stacking Multiple Layers and Grain Size Engineering," *Advanced Functional Materials,* vol. 23, pp. 3638-3644, 2013.
[143] I. Pasternak, M. Wesolowski, I. Jozwik, M. Lukosius, G. Lupina, P. Dabrowski, *et al.*, "Graphene growth on Ge(100)/Si(100) substrates by CVD method," *Scientific Reports,* vol. 6, p. 21773, 02/22/online 2016.
[144] P. T. Trung, J. Campos-Delgado, F. Joucken, J.-F. Colomer, B. Hackens, J.-P. Raskin, *et al.*, "Direct growth of graphene on Si(111)," *Journal of Applied Physics,* vol. 115, p. 223704, 2014.
[145] M. Meibohm, H. H. Otto, and W. Brockner, "Vibrational spectra of copper polysilicate, CuSiO3," *arXiv preprint arXiv:0903.3901,* 2009.
[146] C. S. Liu and L. J. Chen, "Catalytic oxidation of (001)Si in the presence of Cu3Si at room temperature," *Journal of Applied Physics,* vol. 74, pp. 3611-3613, 1993.
[147] D. Manara, A. Grandjean, and D. R. Neuville, "Advances in understanding the structure of borosilicate glasses: A Raman spectroscopy study," *American Mineralogist,* vol. 94, pp. 777-784, 2009.
[148] K. J. Kingma and R. J. Hemley, "Raman spectroscopic study of microcrystalline silica," *American Mineralogist,* vol. 79, pp. 269-273, 1994.
[149] A. Cros, M. O. Aboelfotoh, and K. N. Tu, "Formation, oxidation, electronic, and electrical properties of copper silicides," *Journal of Applied Physics,* vol. 67, pp. 3328-3336, 1990.
[150] L. Stolt, F. M. D'Heurle, and J. M. E. Harper, "On the formation of copper-rich copper silicides," *Thin Solid Films,* vol. 200, pp. 147-156, 1991/05/01 1991.
[151] S. Zhang, J. Wu, Z. He, R. Tu, J. Shi, and L. Zhang, "Effects of annealing processes on Cu x Si1-x thin films," *Journal of Wuhan University of Technology-Mater. Sci. Ed.,* vol. 31, pp. 31-34, 2016.
[152] S. Zhang, J. Wu, Z. He, J. Xie, J. Lu, R. Tu, *et al.*, "Fabrication and characterization of CuxSi1−x films on Si (111) and Si (100) by pulsed laser deposition," *AIP Advances,* vol. 6, p. 055106, 2016.
[153] Z. Zhang, L. M. Wong, H. G. Ong, X. J. Wang, J. L. Wang, S. J. Wang, *et al.*, "Self-Assembled Shape- and Orientation-Controlled Synthesis of Nanoscale Cu_3Si Triangles, Squares, and Wires," *Nano Letters,* vol. 8, pp. 3205-3210, 2008/10/08 2008.

[154] E. Escobedo-Cousin, K. Vassilevski, T. Hopf, N. Wright, apos, A. Neill, *et al.*, "Local solid phase growth of few-layer graphene on silicon carbide from nickel silicide supersaturated with carbon," *Journal of Applied Physics*, vol. 113, pp. -, 2013.

[155] M. Ruan, Y. Hu, Z. Guo, R. Dong, J. Palmer, J. Hankinson, *et al.*, "Epitaxial graphene on silicon carbide: Introduction to structured graphene," *Mrs Bulletin*, vol. 37, pp. 1138-1147, Dec 2012.

[156] S. Bose, "Quantum communication through spin chain dynamics: an introductory overview," *Contemporary Physics*, vol. 48, pp. 13-30, 2007/01/01 2007.

[157] B. B. Buckley, G. D. Fuchs, L. C. Bassett, and D. D. Awschalom, "Spin-Light Coherence for Single-Spin Measurement and Control in Diamond," *Science*, vol. 330, pp. 1212-1215, 2010.

[158] G. de Lange, Z. H. Wang, D. Ristè, V. V. Dobrovitski, and R. Hanson, "Universal Dynamical Decoupling of a Single Solid-State Spin from a Spin Bath," *Science*, vol. 330, pp. 60-63, 2010.

[159] H. J. Kimble, "The quantum internet," *Nature*, vol. 453, pp. 1023-1030, 06/19/print 2008.

[160] R. P. G. McNeil, M. Kataoka, C. J. B. Ford, C. H. W. Barnes, D. Anderson, G. A. C. Jones, *et al.*, "On-demand single-electron transfer between distant quantum dots," *Nature*, vol. 477, pp. 439-442, 09/22/print 2011.

[161] W. Pfaff, B. J. Hensen, H. Bernien, S. B. van Dam, M. S. Blok, T. H. Taminiau, *et al.*, "Unconditional quantum teleportation between distant solid-state quantum bits," *Science*, vol. 345, pp. 532-535, 2014.

[162] D. Press, T. D. Ladd, B. Zhang, and Y. Yamamoto, "Complete quantum control of a single quantum dot spin using ultrafast optical pulses," *Nature*, vol. 456, pp. 218-221, 11/13/print 2008.

[163] M. D. Shulman, O. E. Dial, S. P. Harvey, H. Bluhm, V. Umansky, and A. Yacoby, "Demonstration of Entanglement of Electrostatically Coupled Singlet-Triplet Qubits," *Science*, vol. 336, pp. 202-205, 2012.

[164] E. Togan, Y. Chu, A. S. Trifonov, L. Jiang, J. Maze, L. Childress, *et al.*, "Quantum entanglement between an optical photon and a solid-state spin qubit," *Nature*, vol. 466, pp. 730-734, 08/05/print 2010.

[165] L. Trifunovic, O. Dial, M. Trif, J. R. Wootton, R. Abebe, A. Yacoby, *et al.*, "Long-Distance Spin-Spin Coupling via Floating Gates," *Physical Review X*, vol. 2, p. 011006, 01/26/ 2012.

[166] G. D. Fuchs, G. Burkard, P. V. Klimov, and D. D. Awschalom, "A quantum memory intrinsic to single nitrogen-vacancy centres in diamond," *Nat Phys*, vol. 7, pp. 789-793, 10//print 2011.

[167] R. Kolesov, K. Xia, R. Reuter, M. Jamali, R. Stöhr, T. Inal, *et al.*, "Mapping Spin Coherence of a Single Rare-Earth Ion in a Crystal onto a Single Photon Polarization State," *Physical Review Letters*, vol. 111, p. 120502, 09/20/ 2013.

[168] T. D. Ladd, K. Sanaka, Y. Yamamoto, A. Pawlis, and K. Lischka, "Fluorine-doped ZnSe for applications in quantum information processing," *physica status solidi (b)*, vol. 247, pp. 1543-1546, 2010.

[169] L. Robledo, L. Childress, H. Bernien, B. Hensen, P. F. A. Alkemade, and R. Hanson, "High-fidelity projective read-out of a solid-state spin quantum register," *Nature*, vol. 477, pp. 574-578, 09/29/print 2011.

[170] R. Hanson, L. P. Kouwenhoven, J. R. Petta, S. Tarucha, and L. M. K. Vandersypen, "Spins in few-electron quantum dots," *Reviews of Modern Physics,* vol. 79, pp. 1217-1265, 10/01/ 2007.

[171] D. Loss and D. P. DiVincenzo, "Quantum computation with quantum dots," *Physical Review A,* vol. 57, pp. 120-126, 01/01/ 1998.

[172] J. R. Petta, A. C. Johnson, J. M. Taylor, E. A. Laird, A. Yacoby, M. D. Lukin, *et al.*, "Coherent Manipulation of Coupled Electron Spins in Semiconductor Quantum Dots," *Science,* vol. 309, pp. 2180-2184, 2005.

[173] M. Steger, K. Saeedi, M. L. W. Thewalt, J. J. L. Morton, H. Riemann, N. V. Abrosimov, *et al.*, "Quantum Information Storage for over 180 s Using Donor Spins in a ^{28}Si "Semiconductor Vacuum"," *Science,* vol. 336, pp. 1280-1283, 2012.

[174] A. M. Tyryshkin, S. Tojo, J. J. L. Morton, H. Riemann, N. V. Abrosimov, P. Becker, *et al.*, "Electron spin coherence exceeding seconds in high-purity silicon," *Nat Mater,* vol. 11, pp. 143-147, 02//print 2012.

[175] B. E. Kane, "A silicon-based nuclear spin quantum computer," *Nature,* vol. 393, pp. 133-137, 05/14/print 1998.

[176] H. Büch, Mahapatra, S., Rahman, R., Morello, A. & Simmons, M. Y. , "Spin readout and addressability of phosphorus-donor clusters in silicon," *Nature Communications,* vol. 4, p. 2017, 2013.

[177] L. Oberbeck, N. J. Curson, M. Y. Simmons, R. Brenner, A. R. Hamilton, S. R. Schofield, *et al.*, "Encapsulation of phosphorus dopants in silicon for the fabrication of a quantum computer," *Applied Physics Letters,* vol. 81, pp. 3197-3199, 2002.

[178] F. A. Zwanenburg, A. S. Dzurak, A. Morello, M. Y. Simmons, L. C. L. Hollenberg, G. Klimeck, *et al.*, "Silicon quantum electronics," *Reviews of Modern Physics,* vol. 85, pp. 961-1019, 07/10/ 2013.

[179] M. Fuechsle, J. A. Miwa, S. Mahapatra, H. Ryu, S. Lee, O. Warschkow, *et al.*, "A single-atom transistor," *Nat Nano,* vol. 7, pp. 242-246, 04//print 2012.

[180] G. Scappucci, G. Capellini, B. Johnston, W. M. Klesse, J. A. Miwa, and M. Y. Simmons, "A Complete Fabrication Route for Atomic-Scale, Donor-Based Devices in Single-Crystal Germanium," *Nano Letters,* vol. 11, pp. 2272-2279, 2011/06/08 2011.

[181] P. A. Bennett, M. Copel, D. Cahill, J. Falta, and R. M. Tromp, "Ring clusters in transition-metal-silicon surface structures," *Physical Review Letters,* vol. 69, pp. 1224-1227, 08/24/ 1992.

[182] M.-H. Tsai, J. D. Dow, P. A. Bennett, and D. G. Cahill, "Electronic structure and stability of ring clusters in the Si(111)-(√7x√7)Co surface," *Physical Review B,* vol. 48, pp. 2486-2492, 07/15/ 1993.

[183] R. J. Wilson and S. Chiang, "Surface modifications induced by adsorbates at low coverage: A scanning tunneling microscopy study of the Ni/Si(111)√19 surface," *Physical Review Letters,* vol. 58, pp. 2575-2578, 06/15/ 1987.

[184] T. Yao, S. Shinabe, and M. Yoshimura, "Atomistic study of the formation process of Ni silicide on the Si(111)-7×7 surface with scanning tunneling microscopy," *Applied Surface Science,* vol. 104, pp. 213-217, 1996/09/02 1996.

[185] O. Millo, D. Katz, Y. Cao, and U. Banin, "Scanning tunneling spectroscopy of InAs nanocrystal quantum dots," *Physical Review B,* vol. 61, pp. 16773-16777, 06/15/ 2000.

[186] N. P. Guisinger, M. E. Greene, R. Basu, A. S. Baluch, and M. C. Hersam, "Room Temperature Negative Differential Resistance through Individual Organic Molecules on Silicon Surfaces," *Nano Letters,* vol. 4, pp. 55-59, 2004/01/01 2004.
[187] T. Rakshit, G.-C. Liang, A. W. Ghosh, and S. Datta, "Silicon-based Molecular Electronics," *Nano Letters,* vol. 4, pp. 1803-1807, 2004/10/01 2004.
[188] J. Chen, M. A. Reed, A. M. Rawlett, and J. M. Tour, "Large On-Off Ratios and Negative Differential Resistance in a Molecular Electronic Device," *Science,* vol. 286, pp. 1550-1552, 1999.
[189] G. Buchs, P. Ruffieux, P. Gröning, and O. Gröning, "Defect-induced negative differential resistance in single-walled carbon nanotubes," *Applied Physics Letters,* vol. 93, p. 073115, 2008.
[190] I.-H. Hong, T.-M. Chen, and Y.-F. Tsai, "Observation of room-temperature negative differential resistance in Gd-doped Si nanowires on Si(110) surface," *Applied Physics Letters,* vol. 101, p. 053113, 2012.
[191] I.-W. Lyo and P. Avouris, "Negative Differential Resistance on the Atomic Scale: Implications for Atomic Scale Devices," *Science,* vol. 245, pp. 1369-1371, 1989.
[192] Y. Fang, Z.-Q. Huang, C.-H. Hsu, X. Li, Y. Xu, Y. Zhou, *et al.*, "Quantum Spin Hall States in Stanene/Ge(111)," *Scientific Reports,* vol. 5, p. 14196, 09/16/online 2015.
[193] A. Charrier, J. M. Themlin, F. Thibaudau, I. Forbeaux, and J. M. Debever, "Electronic structure of α and γ phases of Si(111)–3×3–Sn," *Applied Surface Science,* vol. 162–163, pp. 375-379, 8/1/ 2000.
[194] T. Hirahara, T. Komorida, Y. Gu, F. Nakamura, H. Idzuchi, H. Morikawa, *et al.*, "Insulating conduction in Sn/Si(111): Possibility of a Mott insulating ground state and metallization/localization induced by carrier doping," *Physical Review B,* vol. 80, p. 235419, 12/11/ 2009.
[195] T. Kinoshita, H. Ohta, Y. Enta, Y. Yaegashi, S. Suzuki, and S. Kono, "Empty- and Filled-Electronic States of the Si(111) (√3×√3)-Sn, (√3×√3)-In and (2√3×2√3)-Sn Surfaces," *Journal of the Physical Society of Japan,* vol. 56, pp. 4015-4021, 1987/11/15 1987.
[196] A. H. Levermann, P. B. Howes, K. A. Edwards, H. T. Anyele, C. C. Matthai, J. E. Macdonald, *et al.*, "Proceedings of the Fifth International Conference on the Formation of Semiconductor InterfacesThe atomic structure of the Si(111) (2√3×2√3)R30°-Sn reconstruction," *Applied Surface Science,* vol. 104, pp. 124-129, 1996/09/02 1996.
[197] W. Srour, D. G. Trabada, J. I. Martínez, F. Flores, J. Ortega, M. Abuín, *et al.*, "Ultrafast Atomic Diffusion Inducing a Reversible 2√3x2√3 R30 to √3x√3 R30 Transition on Sn/Si(111):B," *Physical Review Letters,* vol. 114, p. 196101, 05/13/ 2015.
[198] I. Toshihiro and C. Kohei, "Structural Study of Si(111)(2√3×2√3)R30°–Sn Surfaces," *Japanese Journal of Applied Physics,* vol. 42, p. 5239, 2003.
[199] H. M. Zhang and L. S. O. Johansson, "STM study of PTCDA on Sn/Si(111)-2√3×2√3," *The Journal of Chemical Physics,* vol. 144, p. 124701, 2016.
[200] F. Ming, D. Mulugeta, W. Tu, T. S. Smith, P. Vilmercati, G. Lee, *et al.*, "Hidden phase in a two-dimensional Sn layer stabilized by modulation hole doping," *Nature Communications,* vol. 8, p. 14721, 03/07/online 2017.
[201] W. Tu, "Structure Analysis fo Sn Bilayer Films on Si(111)," Master of Science, Physics, University of Tennessee Knoxville, 2014.

[202] P. Cai, W. Ruan, Y. Peng, C. Ye, X. Li, Z. Hao, *et al.*, "Visualizing the evolution from the Mott insulator to a charge-ordered insulator in lightly doped cuprates," *Nat Phys,* vol. 12, pp. 1047-1051, 11//print 2016.

[203] C. Renner, G. Aeppli, B. G. Kim, Y.-A. Soh, and S. W. Cheong, "Atomic-scale images of charge ordering in a mixed-valence manganite," *Nature,* vol. 416, pp. 518-521, 04/04/print 2002.

[204] S. A. Parikh, M. Y. Lee, and P. A. Bennett, "Formation conditions and atomic structure of the Si(111)-√19 Ni surface," *Surface Science,* vol. 356, pp. 53-58, 6/10/ 1996.

[205] Z. Hong-Li, L. Feng, L. Chang, and C. Hui-Ming, "The facile synthesis of nickel silicide nanobelts and nanosheets and their application in electrochemical energy storage," *Nanotechnology,* vol. 19, p. 165606, 2008.

[206] H. Zhang, X. Zhong, J. C. Shaw, L. Liu, Y. Huang, and X. Duan, "Very high energy density silicide-air primary batteries," *Energy & Environmental Science,* vol. 6, pp. 2621-2625, 2013.

[207] M. Bartur and M. A. Nicolet, "Thermal Oxidation of Transition Metal Silicides on Si: Summary," *Journal of The Electrochemical Society,* vol. 131, pp. 371-375, February 1, 1984 1984.

[208] L. N. Lie, W. A. Tiller, and K. C. Saraswat, "Thermal oxidation of silicides," *Journal of Applied Physics,* vol. 56, pp. 2127-2132, 1984.

[209] X. Zhou, Y.-X. Yin, L.-J. Wan, and Y.-G. Guo, "Self-Assembled Nanocomposite of Silicon Nanoparticles Encapsulated in Graphene through Electrostatic Attraction for Lithium-Ion Batteries," *Advanced Energy Materials,* vol. 2, pp. 1086-1090, 2012.

[210] J. K. Lee, K. B. Smith, C. M. Hayner, and H. H. Kung, "Silicon nanoparticles-graphene paper composites for Li ion battery anodes," *Chemical Communications,* vol. 46, pp. 2025-2027, 2010.

[211] J. Luo, X. Zhao, J. Wu, H. D. Jang, H. H. Kung, and J. Huang, "Crumpled Graphene-Encapsulated Si Nanoparticles for Lithium Ion Battery Anodes," *The Journal of Physical Chemistry Letters,* vol. 3, pp. 1824-1829, 2012/07/05 2012.

[212] J. Derrien, J. Chevrier, V. Le Thanh, and J. E. Mahan, "Semiconducting silicide-silicon heterostructures: growth, properties and applications," *Applied Surface Science,* vol. 56–58, Part 1, pp. 382-393, 1992.

[213] J. Chang, E. Blackburn, A. T. Holmes, N. B. Christensen, J. Larsen, J. Mesot, *et al.*, "Direct observation of competition between superconductivity and charge density wave order in YBa2Cu3O6.67," *Nat Phys,* vol. 8, pp. 871-876, 12//print 2012.

VITA

NAME: Jian-Yih Cheng

EDUCATION: Ph.D. Candidate, Mechanical Engineering, University of Illinois at Chicago (UIC), 2017

M.S., Mechanical Engineering, UIC, 2011

B.S., Mechanical Engineering, UIC, 2009

EXPERIENCE: Teaching and Research Assistant at UIC 2013-2016

NASA 2013

Energy Resources Center 2009-2013

UIC Industrial Assessment Center 2008-2009

Andersen Corporation 2007

Omron Automotive Corporation 2006

Packer Engineering 2005

AWARDS Argonne Center for Nanoscale Materials Best Poster Award 2014

PROFESSIONAL MEMBERSHIP: American Society of Mechanical Engineers

Institute of Electrical and Electronics Engineers

Materials Research Society

CONFERENCE PAPERS: **J.Y. Cheng**, P.K. Ng, B. Fisher, and C.M. Lilley, "Surface Step Assisted Cu_3Si Nanowire Growth" *IEEE Nano*, Toronto, CA August 18-21, 2014.

P.K. Ng, **J.Y. Cheng**, B Fisher, and C.M. Lilley, "*In situ* Electrical Resistivity Measurement of Self Assembled Cu_3Si Nanowires on Si(111)" *IEEE Nanotechnology Materials and Devices Conference (IEEE-NMDC)*, Waikiki Beach, Hawaii, USA October 16-19, 2012.

Zker, E.; Farid, S.; Selvaraj, S.K.; Bhavanarayana, C.; Sorto, D.; Kaur, R.; Svean, B.; Slusser, S.; Habibimehr, P.; **Cheng, J-Y.**; Sliwa, K.;

Habeebuddin, F.; Kirkpatrick, M.; Dankovic, T.; Punchihewa, K.A.G.; Feinerman, A.; Busta, H.;, "Thermal-based MEMS vacuum gauges for measuring pressures from 10^{-2} Torr to 10^{-6} Torr," *Vacuum Nanoelectronics Conference (IVNC), 2012 25th International*, vol., no., pp.1-2, 9-13 July 2012.

JOURNAL PUBLICATIONS:

J.Y. Cheng, M.K.Y. Chan, and C.M. Lilley, "Enabling direct silicene integration in electronics: First principles study of silicene on $NiSi_2$(111)," *Applied Physics Letters*, vol. 109, p. 133111, 2016.

J.Y. Cheng, B. Fisher, N.P. Guisinger, C.M. Lilley, "Atomically manufactured Nickel-Silicon quantum dots displaying robust resonant tunneling and negative differential resistance," *Nature Quantum Materials*, Accepted.

J.Y. Cheng, G. Ortega, B. Fisher, M.K.Y. Chan, N.P. Guisinger, C.M. Lilley, "Possible charge ordering in two-dimensional layers of Sn on Si(111) at low temperature," In preparation.

J.Y. Cheng, B. Fisher, N.P. Guisinger, C.M. Lilley, "Integration of CVD grown graphene on Si(111) using a Cu_3Si layer," In preparation.

J.Y. Cheng, M.K.Y. Chan, C. M. Lilley, "Enabling direct graphene integration on Si: First principles study of graphene on $NiSi_2$(111) and Cu_3Si(111)," In preparation.